

REPORT DOCUMENTATION PAGE					Form Approved OMB No. 0704-0188	
The public reporting burden for this collection of information is estimated to average 1 hour per response, including the time for reviewing instructions, searching existing data sources, gathering and maintaining the data needed, and completing and reviewing the collection of information. Send comments regarding this burden estimate or any other aspect of this collection of information, including suggestions for reducing the burden, to the Department of Defense, Executive Service Directorate (0704-0188). Respondents should be aware that notwithstanding any other provision of law, no person shall be subject to any penalty for failing to comply with a collection of information if it does not display a currently valid OMB control number.						
PLEASE DO NOT RETURN YOUR FORM TO THE ABOVE ORGANIZATION.						
1. REPORT DATE (DD-MM-YYYY) 28-02-2012		2. REPORT TYPE Final			3. DATES COVERED (From - To) Aug 2008 - Nov 2011	
4. TITLE AND SUBTITLE Development of a 30 kW Inductively Coupled Plasma Torch Facility for Advanced Aerospace Material Investigations				5a. CONTRACT NUMBER		
				5b. GRANT NUMBER FA9550-08-1-0414		
				5c. PROGRAM ELEMENT NUMBER		
6. AUTHOR(S) Fletcher, Douglas, G Meyers, Jason, M Owens, Walten, P				5d. PROJECT NUMBER		
				5e. TASK NUMBER		
				5f. WORK UNIT NUMBER		
7. PERFORMING ORGANIZATION NAME(S) AND ADDRESS(ES) University of Vermont & State Agricultural College University of Vermont 85 S. Prospect St Burlington, VT 05405-1704					8. PERFORMING ORGANIZATION REPORT NUMBER	
9. SPONSORING/MONITORING AGENCY NAME(S) AND ADDRESS(ES) Air Force Office of Scientific Research 875 N. Randolph St. Room 3112 Arlington, VA 22203					10. SPONSOR/MONITOR'S ACRONYM(S)	
					11. SPONSOR/MONITOR'S REPORT NUMBER(S) AFRL-OSR-VA-TR-2012-0281	
12. DISTRIBUTION/AVAILABILITY STATEMENT Distribution A - Approved for Public Release						
13. SUPPLEMENTARY NOTES						
14. ABSTRACT A 30 kW Inductively Coupled Plasma (ICP) Torch for testing high-temperature materials for aerospace applications has been designed, constructed, and made operational at the University of Vermont. A key advantage of the inductive heating approach to creating the plasma is the electrodeless operation, which avoids the copper contamination from electrode attachment of traditional arc heaters. Heat flux probes have been fabricated and used to characterize the heating rates. In addition, sample holders for both shape-stable and ablative material samples have been developed for use in the facility. Surface temperature measurements using a two-color optical pyrometer have been demonstrated. Tests have been conducted on graphite, SiC, and ZrB <sub>2</sub> -SiC samples. Current test capabilities for continuous operation include heat flux levels up to 120 W/cm <sup>2</sup> for air and nitrogen plasmas at pressures between 100 and 200 torr, and surface temperatures to 1800 K for graphite. A unique feature of the ICP Torch Facility is the inclusion of optical access to allow emission and laser-spectroscopic measurements in the plasma/surface reaction zone. Emission measurements have been used to track the evolution of boron depletion and silicon-oxide layer formation over a UHTC test sample.						
15. SUBJECT TERMS High temperature materials, plasma testing, UHTC, laser diagnostics						
16. SECURITY CLASSIFICATION OF:			17. LIMITATION OF ABSTRACT	18. NUMBER OF PAGES 87	19a. NAME OF RESPONSIBLE PERSON Douglas G. Fletcher	
a. REPORT UU	b. ABSTRACT UU	c. THIS PAGE UU			19b. TELEPHONE NUMBER (Include area code) 802 656 9863	


Reset

**University of Vermont  
Mechanical Engineering**

201 Votey Bldg  
33 Colchester Ave  
Burlington, VT 05405

**Development of a 30 kW Inductively  
Coupled Plasma Torch Facility for  
Advanced Aerospace Material  
Investigations**



 <b>The UNIVERSITY of VERMONT</b>  University of Vermont Mechanical Engineering		<b>CLASSIFICATION</b>			<b>CATEGORY</b>		
		1. Unclassified <input checked="" type="checkbox"/> 2. Industry <input type="checkbox"/> 3. Restricted <input type="checkbox"/> 4. Confidential			1. For approval <input type="checkbox"/> 2. For review <input type="checkbox"/> 3. Other <input type="checkbox"/>		
		<b>CONFIGURATION</b>					
		Controlled		<input type="checkbox"/>	Not Controlled		<input type="checkbox"/>
Agency	Program	Contract number:			Period:		
AFOSR	High Temperature Materials	FA9550-08-1-0414			08/01/08 to 11/30/11		
<b>TITLE:</b>  <p style="text-align: center;"><b>Development of a 30 kW Inductively Coupled Plasma Torch for Advanced Aerospace Material Investigations</b></p>							
<b>AUTHOR(S):</b>  <p style="text-align: center;"><b>D. G. Fletcher, J. M. Meyers, and W. P. Owens</b></p>							
<b>ISSUE.</b>		Internal Reference Number			Number of pages: 22		
Date: February 21, 2012		12/UVM/AFOSR/ICP-02			Number of included annexes: 0		
Issue 1 Rev. 0.							
<b>SUMMARY:</b> This final report summarizes the work performed to develop and exploit a 30 kW Inductively Coupled Plasma (ICP) Torch Facility for high-temperature testing of aerospace materials at the University of Vermont during the period from August 1, 2008 to November 30, 2011. The objectives of this work are briefly revisited and the progress toward meeting the objectives is summarized by archival conference papers describing some of the material investigations that have been carried out. The conference papers are included as appendices.							
<b>HOST SYSTEM</b>	<b>HARDWARE EQUIPMENT.</b>	<b>MEDIA.</b>			<b>SOFTWARE.</b>		
	Nature: Mac	Nature & Type: Identification:			Name: Microsoft Word 2010		
<b>KEY WORDS</b>		<b>LANGUAGE CODE</b>			<b>APPROVAL.</b>		
		ENG					
Plasma torch, ground test, high temperature, thermal protection material, laser diagnostics, heat flux					Laboratory:		
					D. G. Fletcher		

I. Investigation Objectives..... 4

Appendices:

A. W. P. Owens et al, “Development of a 30 kW Inductively Coupled Plasma Torch Facility for Aerospace Material Testing”, AIAA 2010-4322, June 2010. ....6

B. J. Marschall and D. G. Fletcher, “High enthalpy test environments, flow modelling, and *in situ* diagnostics for characterizing ultra-high temperature ceramics”, *JECS*, **30**, (2010), pp. 2323-2336 .....21

C. D. G. Fletcher et al, “Realization of a Gas-Surface Interaction Test Case for CFD Validation”, AIAA 2010-1249, 48<sup>th</sup> AIAA Aerospace Sciences Meeting, January 2010.....34

D. M. Dougherty, W. Owens, J. Meyers, and D. Fletcher, “Investigation of Surface-Catalyzed Recombination Reactions in the Mars Atmosphere”, AIAA 2011-1326, 49<sup>th</sup> AIAA Aerospace Sciences Meeting, January 2011 .....53

E. A. Lutz, W. Owens, J. Meyers, D. G. Fletcher, and J. Marschall, “Investigation of CN Production from Carbon Materials in Nitrogen Plasmas”, AIAA 2011-0901, 49<sup>th</sup> AIAA Aerospace Sciences Meeting, January, 2011.....64

F. D. G. Fletcher, A. J. Lutz, J. M. Meyers, W. P. Owens, and J. Uhl, “Species and Temperature Gradient Measurements in the Reacting Boundary Layer over ICP Test Samples”, Proceedings of the 7<sup>th</sup> European Symposium on the Aerothermodynamics of Space Vehicles, ESA Special Publication SP-692, May, 2011.....80

## I. Investigation Objectives

The overall goal of the 4-year research program was to develop a 30 kW ICP Torch Facility for testing advanced candidate thermal protection materials in a harsh plasma environment. The operating capabilities of such a facility were expected to include variable species plasmas and high surface temperatures for the materials.

The investigation had five specific objectives:

1. Design and develop a 30 kW ICP Torch Facility for material testing with advanced gas-phase and material diagnostic capabilities.
2. Evaluate operation of the 30 kW ICP Torch Facility by systematically varying its operational parameters and quantifying its performance.
3. Develop the instrumental and analytical tools needed to characterize the plasma conditions and to determine material catalytic efficiency values (including sample holder, heat flux and pitot probe(s) and optical pyrometry).
4. Demonstrate the capability of the 30 kW ICP Torch Facility by performing tests of material samples in concert with duplicate tests at VKI.
5. Implement advanced material and gas-phase diagnostics, including emission spectrometry for the material and the material boundary layer, and laser-spectroscopic techniques for measuring key species flux rates toward and away from the material surface during testing.

Progress in achieving these objectives is described in a series of peer-reviewed papers that are attached to this document as appendices. The first paper was presented at the AIAA Thermophysics Conference in June, 2010, and it details the key design features of the 30 kW ICP Torch Facility, the test conditions achieved, and the means by which the facility was finally made operational. Thus, it also addresses the third specific objective listed above. Efforts continue to improve test condition stability, and to provide higher heating rates and higher surface temperatures. This paper also addresses part of the second objective, although this is not complete owing to current component limitations. It should be noted that the facility was built, and then rebuilt a second time to obtain the current level of performance.

The remaining papers present examples of material and gas-surface interaction investigations that highlight the unique features of the 30 kW ICP Torch Facility. The first of these is a survey of the state-of-the-art for laser diagnostics applied to gas-surface interactions. This paper was written for the 2009 UHTC Workshop and was subsequently published in the Journal of the European Ceramic Society. The subsequent paper presents a detailed numerical investigation of the effect of surface-catalyzed recombination reaction efficiency on atomic species diffusion gradients in the reacting, non-equilibrium boundary layer above the material surface. This paper was presented at the 48<sup>th</sup> AIAA

Aerospace Sciences Meeting in January, 2010, and the study was linked to the state-of-the-art survey.

The two following papers were presented at the January, 2011 49<sup>th</sup> AIAA Aerospace Sciences Meeting. The first describes a laser spectroscopic investigation of the species gradients over a copper surface for a carbon dioxide plasma. The second paper describes laser spectroscopic measurements used to evaluate carbon nitridation of graphite samples. In each case, the gradient in species distribution within the thermal boundary layer over the surface is used to assess the relative surface reaction rate.

For the latter case, carbon nitridation, additional measurements were performed to obtain absolute species concentrations, and a rate for this reaction was elucidated from the measured values. This paper was presented at the 7<sup>th</sup> European Symposium on Aerothermodynamics of Space Vehicles in June, 2011.

# Development of a 30 kW Inductively Coupled Plasma Torch Facility for Aerospace Material Testing

*W. P. Owens\*, J. Uhl\*, M. Dougherty\*, A. Lutz\*, Jason Meyers† and D. G. Fletcher‡  
Mechanical Engineering, University of Vermont, Burlington, VT, 05405*

## Abstract

The development of a new 30 kW Inductively Coupled Plasma (ICP) Torch Facility for testing advanced aerospace materials is presented. The design of the facility and the fabrication of the major system components are described. Operating capabilities and results of the preliminary tests are discussed. A major objective of the facility design was to enable spectroscopic diagnostic access to the reacting boundary layer over the material surface.

## Nomenclature

$b$	=	load coil radius, $m$	$P$	=	stagnation pitot pressure, $atm$
$c$	=	specific heat of slug, $J Kg^{-1} K^{-1}$	$q$	=	heat flux, $W cm^{-2}$
$\delta$	=	plasma skin thickness, $m$	$\rho$	=	density of slug, $Kg m^{-3}$
$f$	=	frequency, $Hz$	$R$	=	plasma radius, $m$
$l$	=	overall load coil length, $m$	$\sigma$	=	electrical conductivity, $S m^{-1}$
$L$	=	length of slug, $m$	$t$	=	time, $s$
$\mu$	=	magnetic permeability, $H m^{-1}$	$T$	=	temperature, $K$
$N$	=	number of load coil turns			

## I. Introduction

A 30 kW inductively coupled plasma (ICP) torch facility has been designed and assembled at the University of Vermont. An ICP torch is a device designed to heat gases to very high temperatures through electron excitation and heavy particle collisions. The inductively coupled approach is attractive to applications where a clean and stable source of plasma is essential. The facility will test advanced aerospace materials for thermal protection of hypervelocity vehicles.

Although inductive discharges have been studied for over a century, ICP torch facilities have not been extensively developed in the U.S. to simulate the aero-thermal environments needed for the development of thermal protection materials. Typical applications of ICP technology include synthesis of fine powders, spectrochemical elemental analysis as well as other large scale industrial applications. Current US facilities designed for aerospace applications use arc heaters, which rely on a direct arc discharge to produce a plasma. Owing to the attachment of the arc to electrodes, arc-heated facilities tend to have electrode material in the stream as a contaminant. Arc-heated facilities tend to be expensive to operate. For either type of plasma facility, stagnation point test conditions for materials are based on duplicating total enthalpy, post shock total pressure and the velocity gradient from the hypersonic flight environment.

In the following sections the design and fabrication of each different subsystem is described in detail. This is followed by a discussion of the standard instruments that have been developed to characterize facility operation. Data from these measurements are presented and are used to assess whether or not the facility design criteria are met.

---

\*Graduate student, Mechanical Engineering, 33 Colchester Ave, Burlington, VT 05405 USA

†Post-doctoral researcher, Mechanical Engineering, 33 Colchester Ave, Burlington, VT 05405 USA, Member AIAA

‡Professor, Mechanical Engineering, 33 Colchester Ave, Burlington, VT 05405 USA, Associate Fellow AIAA

## II. Facility Description

The primary components of the facility are the RF power supply, coil/injector-block assembly, and the test chamber. Sub-systems that are required for operation of the torch include the gas feed, cooling and exhaust systems. The configuration of the major components can be seen in Fig 1. The effective design of the ICP torch depends on the integration of the power supply, gas supply and the pressure control systems.

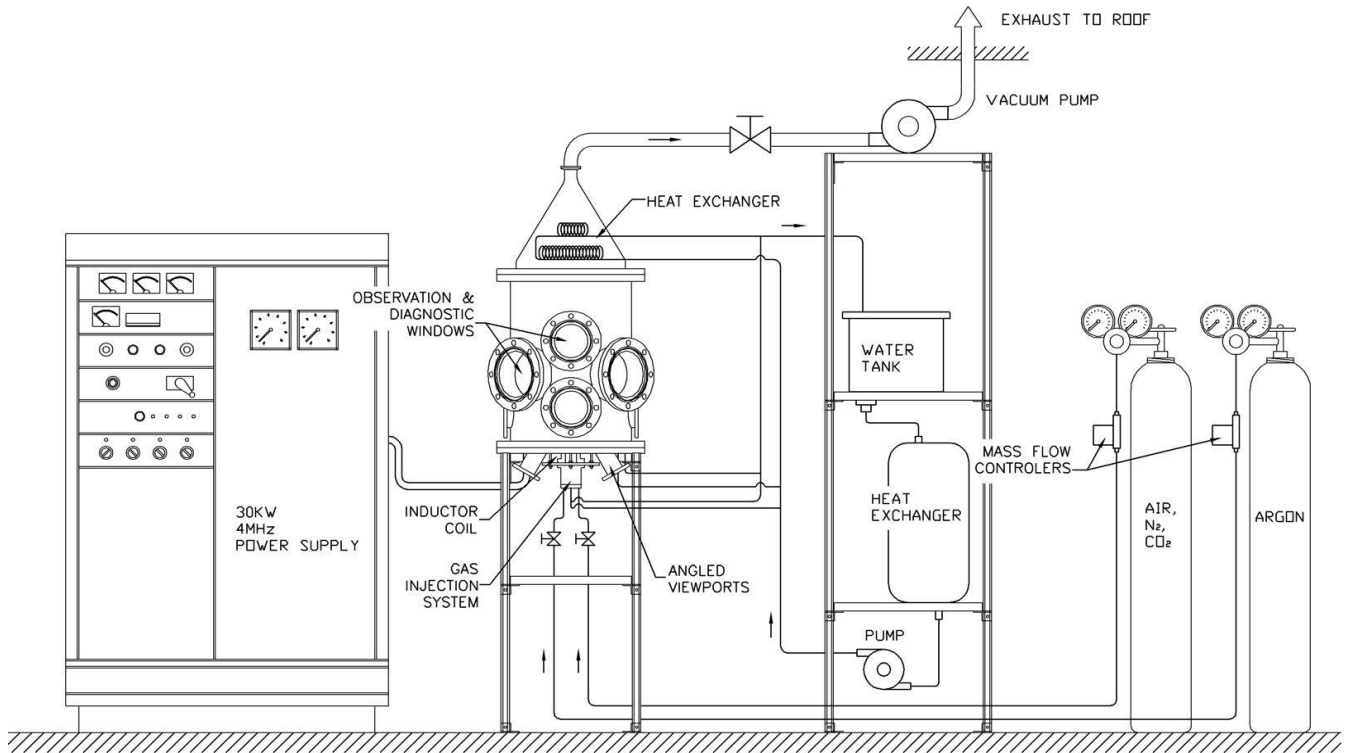


**Figure 1. Schematic of the ICP Torch including major components.**

### II. A. Power Supply

The power supply is a Lepel Model T-30-3-MC5-J-TL1 induction heating generator that delivers up to 30kW of radio frequency (RF) energy at a frequency between 2.5-5Mhz. It is rated for continuous duty and was re-engineered from its original application as a fiber optic furnace to work for plasma generation. The power supply contains a primary saturable reactor control with silicon diode rectifier stacks. All components are conservatively rated and a network of safety devices and warning lights are employed to protect both the operator and the equipment. The power supply converts line voltage through a three phase plate transformer and rectifiers to DC voltage. Plate power is controlled by varying this DC voltage level. A grid-tuned plate oscillator converts the high voltage DC power to RF output power supplied to the tank circuit. A proper tank circuit and the variable grid coil provide the flexibility required for matching a wide variety of plasma conditions to the generator output.

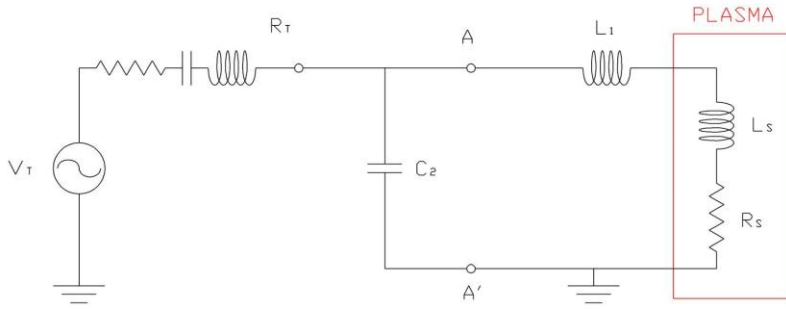


**Figure 2. Tank circuit configuration**

is a function of the capacitance, inductance, and resistance. Impedance of the plasma ball can be determined from the coil geometry and gas characteristics, such as the electrical conductivity. The equivalent plasma resistance and inductance can be calculated using Eq (1) and Eq (2) respectively<sup>1</sup>.

$$\text{Plasma Resistance} \approx N^2 \frac{2\pi R}{\sigma_{eff} l \delta_p} \quad (1)$$

$$\text{Plasma Inductance} \approx \frac{\mu_0 \pi R^2 N^2}{l} \left( \frac{b^2}{R^2} - 1 \right) \quad (2)$$

Where the skin thickness  $\delta$  is calculated using Eq (3).

$$\delta_p \approx \sqrt{\frac{1}{\pi \mu_0 \sigma_{eff} f}} \quad (3)$$

A functional parallel tank circuit was developed experimentally with a combination of removable vacuum capacitors and fixed air inductors. The current tank circuit wiring diagram can be seen in Fig 2. Because electrical conductivity of the plasma is changing with conversion of gases, the impedance is also changing. This requires the ability to vary the impedance of the tank circuit. Variable grid control is combined with adjustable capacitance to accommodate the different plasma conditions with different gases.

## II. B. Plasma Generation Components

The creation of the plasma occurs inside the induction region of the torch. There are three major components of the plasma creation, the coil, confinement tube and the gas injection system. Creation of a plasma can be seen in Fig 3. The fundamental phenomena governing the operation of inductively coupled plasmas are essentially analogous to those of the induction heating of metals with the “load” now being the conducting plasma gas. Unlike most metals, plasmas have a substantially lower electrical conductivity, which has a direct influence on the optimal frequency, size, and power combination, necessary to sustain a stable plasma

The plasma is generated through an induced RF magnetic field created by a helical load coil. Coils with 5 or 6 turns have proven to work best with our power supply. The coil geometry is designed to maximize the power into the plasma and enhance coupling efficiency. The coil is made of 6mm outer diameter copper and cooled with internal circulation of water flow from the power supply.

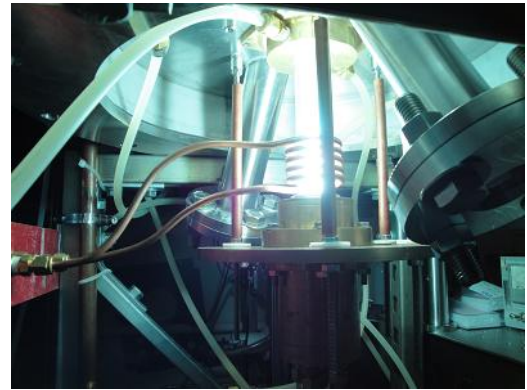


**Figure 3. Photograph of the induction region of the plasma torch with a 5 turn load coil and modified base plate**

The ideal coil diameter is equivalent to that of the plasma diameter, however physical constraints determine the minimum offset of the load coil. A close proximity to the confinement tube contributes to more efficient coupling. Conversely, if the coil is too close to the quartz tube it will arc with increasing power.

The spacing between each turn of the coil was designed to maximize the concentration of the induced magnetic field by making them as close as possible without making the gap so small that it will arc to the next coil. Coil height is set as close as possible to the injector block without arcing and without overheating the bottom o-ring that seals the injector block to the quartz tube. This takes advantage of the recirculation zone produced by the annular region of the injector block. It also maximizes the impact of a sheath gas, which actively cools the quartz tube from the plasma ball. Leads to the coil are kept short to limit transmission loss as well as to dampen vibration. The coil, quartz tube, and o-rings are currently viewed as consumables with a limited operating life but great measures have been taken to increase the time between replacements.

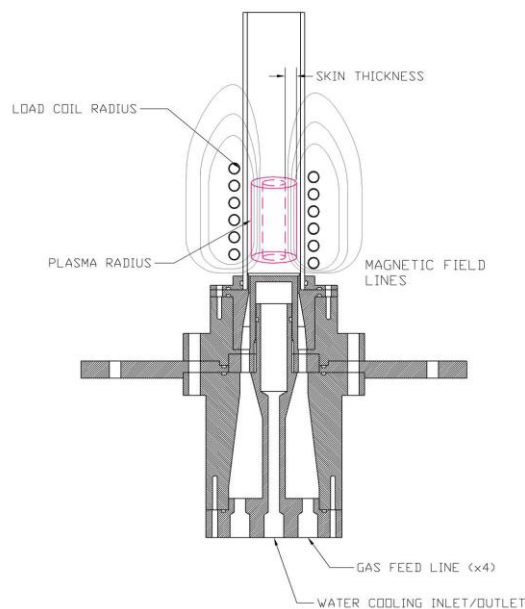


**Figure 4. Initial gas injection system**

The injector block is the gas distributor which inserts room temperature gas into the confinement tube. The gases enter through four inlets and exit through a .75mm annulus. This is designed to produce a recirculation zone in the confinement tube as well as a sheath gas layer to prevent the plasma ball from touching the confinement tube. The injector block assembly is made completely of brass to maximize heat transfer and thereby avoid overheating. The individual stages are sealed with viton o-rings which have a temperature rating to 400C. The assembly is water cooled in the center and is suspended on threaded rod attached to the base plate of the vacuum chamber. The flange that supports the injector block acts as a large heat transfer surface to assist the cooling of the exterior through convection. The injector block is insulated from ground to prevent arcing with nylon bushings between the support flange and the threaded rod. The threaded rod is also insulated with a phenolic tube to prevent arcing from the coil. All sharp edges and protruding bolts have also been rounded. The injector block is moved along the axis of the threaded rod for the installation of the quartz tube. Our current configuration is based on the design presented in Ref. 2.

The confinement tube currently has a 30mm inner diameter and made of quartz. It is rated for a melting temperature of 2000K. A 200mm length has been found to offer the best performance. Shorter tubes are less costly but the plasma ball sits too close to the upper seal which causes the o-ring to melt. Under improper operating conditions the quartz tube is susceptible to melting. A high gas feed flow is necessary to promote cooling along the quartz tube. A depiction of all the major plasma generating components can be seen in Fig 4.

## II.C. Vacuum Chamber

The vacuum chamber is comprised of three major sections, the test chamber, base plate, and upper cap. The complete assembly is seen in Fig 5.

The stainless steel test chamber was designed to provide optical access from four directions with auxiliary ports for instrumentation and sample access. Stainless steel was chosen to avoid contamination of the plasma flow by oxidized metals. Three viewports are located at the same axial position with direct view of the plasma jet and sample. These ports allow optical access for laser-induced fluorescence and emission detection.

The plasma flow enters the test chamber through the base plate from below. The base plate houses the quartz tube adapter and also contains angled viewports. The angled ports on the bottom of the chamber provide a direct view of the test article surface for optical pyrometry and/or observation. It is also constructed of stainless steel with a water cooled double jacket construction to prevent warping from high heat loads.

The upper cap is a stainless steel conical shape designed to funnel the exhaust gases into a 5cm stainless flex hose which leads into the vacuum pump. This conical cap defines the exit of the test chamber and constricts the flow in a manner which promotes cooling through a heat exchanger. This is needed to protect the vacuum pump and to promote efficient pumping. The vacuum chamber sits atop a channelled frame bolted together with brackets. Stabilizing members are in place to add structural support and to limit vibration. The frame is permanently bolted to the floor to keep the system aligned with the power supply, and optical tables.

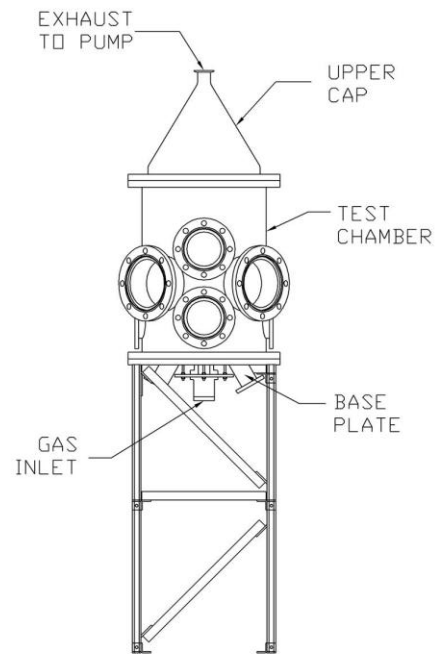


**Figure 5. Schematic of the vacuum chamber and stand**

## II.D. Cooling System

The torch locations with the highest heat loads are actively cooled with a closed loop water system. Separate cooling loops are provided for the injector block, quartz tube adapter, base plate, calorimeters, and both heat exchangers. Two pumps are used to circulate water. A model 30RT magnetic drive pump serves the injector block and base plate. A model 40RT pump provides circulation for all the other water cooled components.

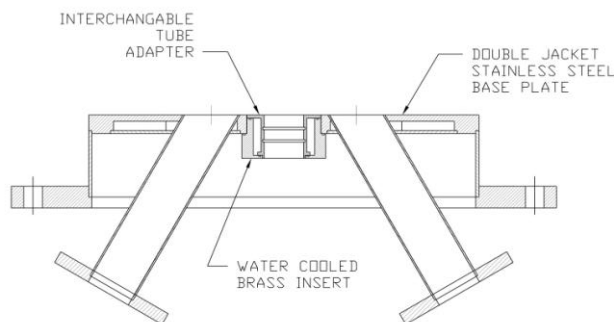


**Figure 6. Schematic of the revised base plate to increase cooling and allow for the use of multiple sized quartz tubes**

The quartz tube adapter connects the quartz tube to the base plate and provides proper cooling to o-rings. Installation of the adapter and base plate is depicted in Fig 6. The tube adapter is made of brass to promote cooling through conduction. It also adapts for 34mm and 40mm OD quartz tubes which can be changed without removing the entire bottom plate. It is designed to simplify the installation process. Two grooves were machined for 1.5mm diameter o-rings for a face seal. 1.5mm o-rings maximize the longevity and provide an adequate base pressure for multiple runs without melting. Smaller o-rings have been found to promote conductive heat transfer and to minimize the surface area in contact with the quartz tube causing them to be less susceptible to melting.

The chamber heat exchanger in the upper cap is comprised of two different sections. The first section comprises of approximately 8 meters of 6mm coiled copper tubing with 40mm diameter windings. This has proven to be a robust design with a negligible pressure drop, but it did not provide sufficient cooling of the exhaust gases going into the vacuum pump. A second heat exchanger section was built using L shaped aluminium finned copper tubing from a

baseboard heating element. This provides efficient cooling but for higher pressures and higher power the un brazed fins exhibited failure. A replacement section with 6mm brazed copper fins is being developed.

A rooftop chiller circulates glycol from the roof to the lab. It provides cooling to the power supply and to a glycol / water heat exchanger. This chiller was designed for a 24kW capacity. The glycol is continuously circulated through a bypass valve until needed during the operation of the facility.

The glycol / water heat exchanger provides cooling to the torch water cooling system. It is used to regulate the temperature of the cooling system. The temperature is typically maintained at  $\pm 3$  degrees C of room temperature. If the temperature rises too high it might not provide adequate cooling of the torch and if it drops too low condensation will collect on the system and may cause damage to the electrical components. The water reservoir allows for water to be drained or filled for the water cooling system. The heat exchanger can be seen in Fig. 1 located above the pumps to provide adequate head to prime them. The additional water in the reservoir increases the thermal mass of the system and helps to keep the water at a stable temperature. The large volume of water allows the torch to be run at operating conditions for over 5 minutes without the rooftop chiller, while keeping the water at a safe operating temperature. The average operating temperature of the cooling system is measured in the water reservoir.

## **II.E Exhaust and Pressure Control**

The flow exits the vacuum chamber to an elevated vacuum pump, which exhausts into a ventilated duct terminating on the roof. The vacuum pump is connected to the chamber with KF-flanges through a flexible tube on the top of the upper cap. The vacuum pump was sized with the capability of reaching a base pressure in the test chamber of 0.2 torr. It allows the proper range of desirable pressures for start up and test conditions. A gate valve controls the pressure inside the test chamber. It is necessary to vary the pressure from initiation of the plasma ball to conversion to the test gas and to achieve desirable operating conditions. A refurbished 5cm inner diameter knobbed gate controls the chamber pressure for operation at the required pressure.

## **II.F. Gas Feed**

The gas that enters the vacuum chamber is from tanks fixed securely to the wall out of the way of the optical and torch components. The gas tanks contained argon, nitrogen, carbon dioxide and air ( $N_2$ ,  $O_2$  mixture). Each tank has a regulator and an auxiliary shut off valve. Poly tubing connects the tanks to a stainless steel manifold. Two separate stainless steel lines are used to bring gases to the injector block to limit contamination. A 10mm diameter line provides the argon start gas to the facility, and the larger 13mm line carries the pre-mixed gases for the plasma test. All connections were made with Swagelock fittings. All gas feed lines have mass flow meters/controllers to allow for appropriate gas mixtures. The mass flow meters operate from 0 to 50 slpm for argon and 0 to 50 slpm for the test gas. The gas flow rate is changed with two gate valves. Initial operation has relied on gate valve control of mass flow but for future operation precise flow rates will be preset on the controllers.

## **III. Probe and Sample Holder Access**

Two ports on the vacuum chamber are designated for probe insertion in and out of the plasma flow. Two probes were developed to allow multiple diagnostics to be performed during the same test run by inserting and removing each probe individually. Each probe was designed to mount interchangeable diagnostic equipment and test samples. The different probes are each described in the following sections.

### **III.A. Gooseneck Probe**

A temporary copper probe was designed and built to take initial measurements while another probe was being engineered for more permanent usage. The objective of the probe was to be built quickly and cheaply. The probe is made of sweat copper tubing with internal plumbing providing water cooling throughout. This design has proven to withstand the intense heat loads without leaking or becoming damaged. It has an internal vacuum-sealed tube that allows thermocouple leads to be easily wired to the head of the probe. Its gooseneck design allows the probe to be swung in and out the direct plasma flow by rotating the probe externally of the vacuum chamber as seen in Fig. 7.

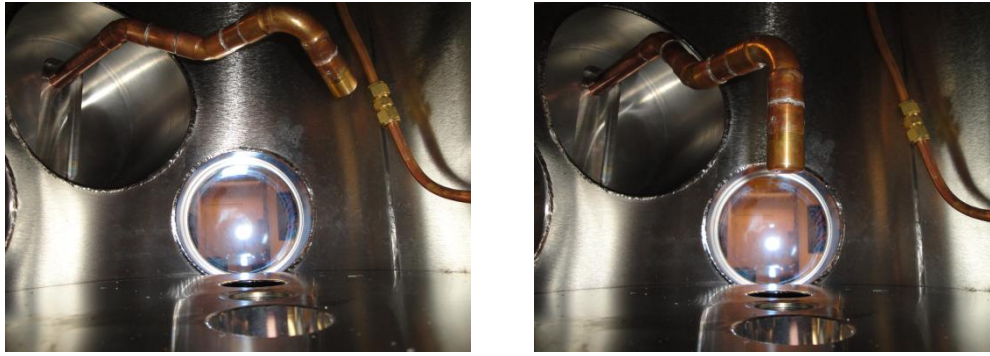


**Figure 7. Pictures of inside the vacuum chamber with the gooseneck probe removed from the plasma flow (left) and in the stagnation point configuration for data collection (right)**

Limitations of this probe include its inability to be easily disassembled if it ever needs to be modified. It must be completely removed from the torch to interchange the diagnostics at the head of the probe. Its vertical height in the flow cannot be changed while a vacuum is present. Another concern is the probe only allows for limited cooling through conduction to the diagnostic apparatus causing them to be damaged with prolonged exposure to the direct plasma flow. Fortunately this simple design has shown to be very robust, require little care, and exceed the requirements for initial tests.

### **III.B. Machined Brass Probe / Sample Holder**

This design incorporates the use of three concentric tubes to provide water cooling and to allow for instrument or thermocouple leads to reach a sample or calorimeter. Attached to the front adapter is a cup segment that will hold the material samples. This cup segment has an insulating feature and has specific channelling features that allow for the reversal of the water flow. The holder is designed in such a way as to provide an effective, yet simple fastening mechanism that allows its users to easily take apart and reattach the sample holder.

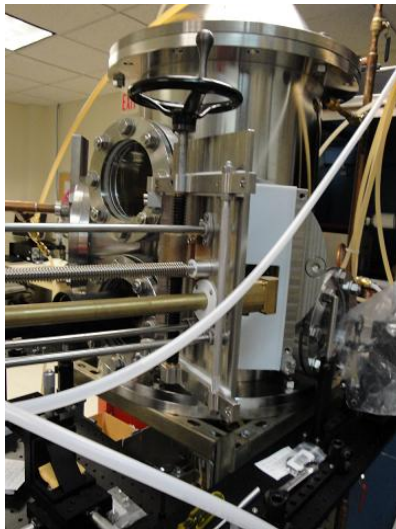


**Figure 9. Photo of the probe and opened external support apparatus**

This probe/sample holder has an adjustable, external support apparatus, which allows horizontal and vertical movement. A series of five compressed plates, a screw, and a hand crank to provide the capacity for vertical movement. Compression of the plates for sealing is provided by a series of bolts that connect the plates. This design allows for the external apparatus to be adjusted while maintaining a constant pressure in the actual plasma chamber.

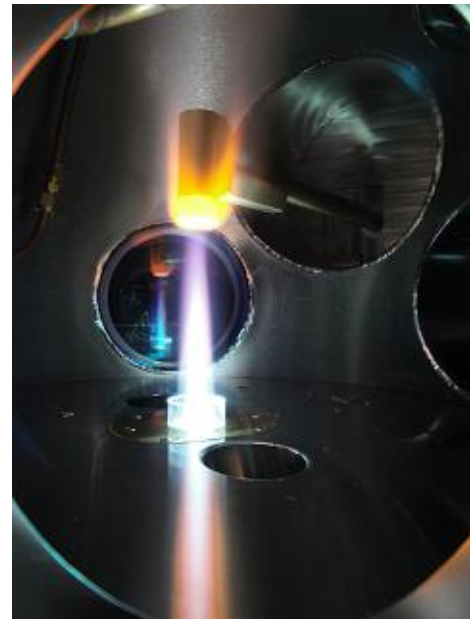


**Figure 8. Photo of the machined brass probe holding a graphite sample in a argon/carbon dioxide flow**

The mount also has a hinged section that allows easy opening and closure, making the set up and adjustment of the material sample on the end of the probe relatively simple.

### III.C. Optical Access

The test chamber was designed with optical access for spectroscopic measurements, as shown below in Fig. 10 for a typical Laser-Induced Fluorescence (LIF) configuration. The four lower ports on the chamber are arranged orthogonally, with two for laser beam access and one for fluorescence imaging. All ports accommodate 15 cm windows, and the two laser access windows are coated with a broad uv anti-reflection coating to minimize scattered light. The detection port has an uncoated 15 cm diameter window, and all windows are fused silica. To help reduce stray light, the port opposite the detection side is covered by a stainless steel flange that contains bulkhead fittings for additional cooling as needed within the chamber. Additional spectroscopic instruments that are being implemented in the facility include a diode-laser absorption system and an emission spectrometer. Details of the laser spectroscopic instrument implementation in this are presented in Ref. 3.

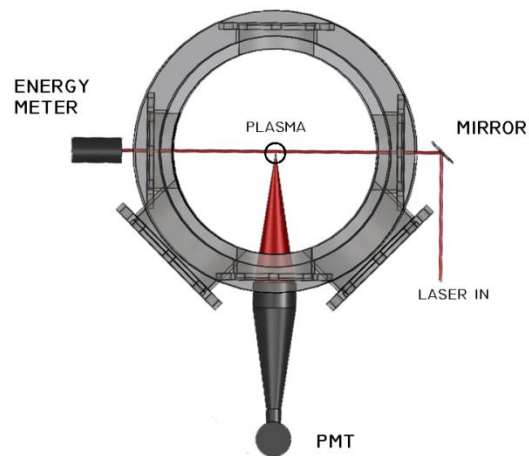


**Figure 10. Optical access for spectroscopic measurements**

#### IV. Facility Characterization

The 30 kW ICP Torch Facility currently provides usable operating conditions and its capabilities are continuously being improved; including its run duration, peak heat flux, operational gas composition and pressure range. The completely assembled torch is shown in Fig. 11. Preliminary tests have been conducted for a limited range of conditions for different gases including: argon (100%), air (100%), nitrogen (100%), carbon dioxide and variable mixtures with argon.

A typical operation always starts with argon at a low pressure of less than 10 torr. Argon is easily ignited and then the flow rate and pressure are immediately increased to prevent damage to the induction region of the torch. A 100% argon plasma can be seen in Fig 12. The test gas is then slowly added to the flow as the power is increased. The ability to carefully control the flow rates is essential for initiation of the argon plasma and conversion to the test gas. An air/argon plasma can be seen in Fig 12. Once the test gas is added, the argon is slowly removed until the desired flow rate is achieved. Typically a small flow rate of argon is kept on to improve the stability of the plasma and allow for continuous operation of the torch. Complete removal of argon is possible at our facility but run time and control is limited. A 100% nitrogen plasma can be seen in Fig 17. Our current ICP torch capabilities can be seen in Table 1.

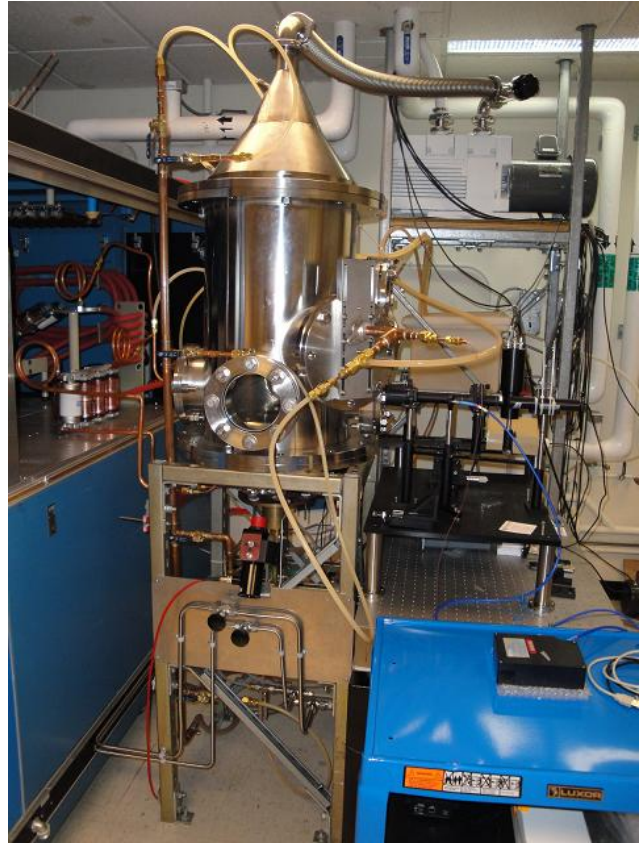


**Figure 11. A picture of the completely assembled ICP Torch. The installation of initial diagnostic equipment can be seen**

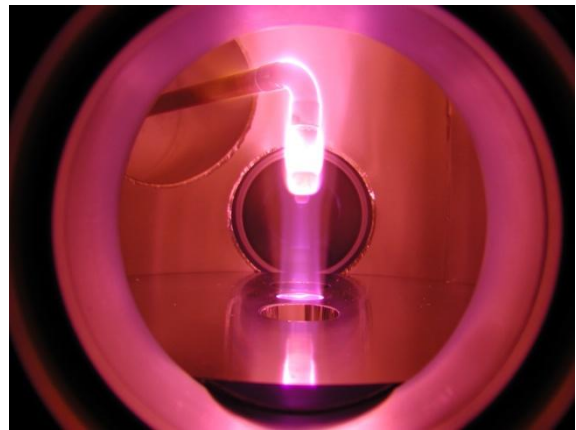
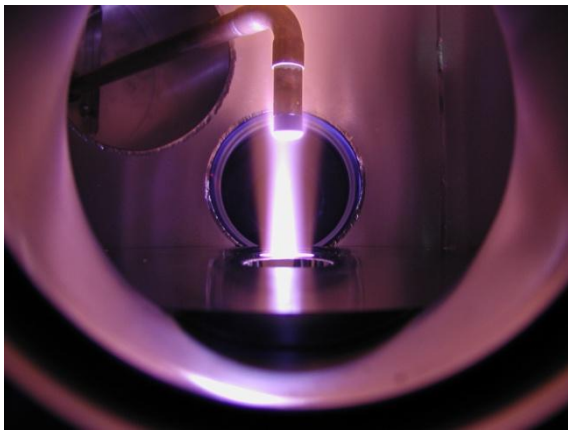
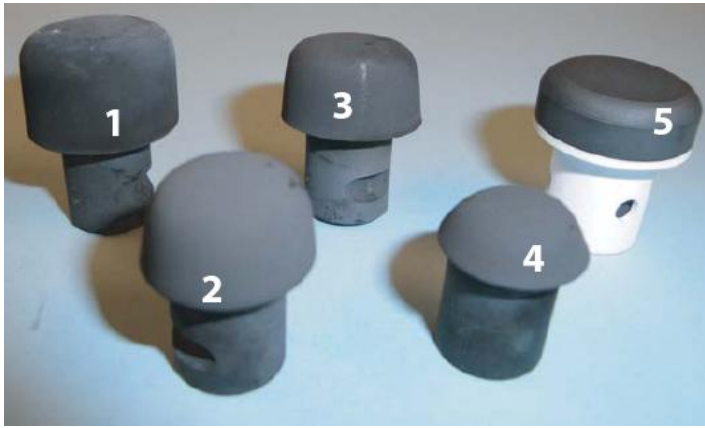


**Figure 12. Photograph of a graphite sample in an; argon plasma (left), air/argon plasma mixture (right)**



Ablation of graphite test samples as well as a virgin sample can be seen in Fig 13. Samples labelled 1 through 4 were exposed to increasing durations of an air plasma flow in a stagnation point configuration. Sample 5 is a virgin nitrogen sample housed inside a machined ceramic insulator. Air samples are thicker due to the more rapid ablation of the surface.

Improvements to the torch include increased cooling to high heat load locations to increase run duration. The base plate was redesigned and a more efficient heat exchanger is in the process of being built. The tank circuit and load coil designs are continuously being optimized for the test gas to provide more efficient energy transfer into the plasma.

**Figure 13. Graphite samples with varying exposures to air and nitrogen flows**

---

Max Run Time:	6 <i>min.</i> with manual shut down
Max Recorded Heat Flux:	85 $W\ cm^{-2}$ (Slug)
Max Graphite Surface Temperature:	2123 <i>K</i>
Max Operating Chamber Pressure:	180 <i>torr</i>
Gas Composition:	Ar, Air, N <sub>2</sub> , and CO <sub>2</sub> mixtures
Operating Frequency:	2.7 <i>MHz</i>

---

**Table 1. Current capabilities of the ICP Torch at UVM**

#### IV.A. Surface Temperature Measurements

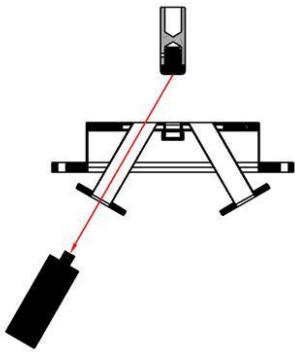


**Figure 14. Schematic of the pyrometer view of the sample through the angled viewports**

A Marathon two-color infrared optical pyrometer is used to measure surface temperatures on test samples. Surface temperature provides a direct measure of the performance of the test material exposed to the plasma flow. The pyrometer is installed with a direct view of the leading surface through an angled viewport on the base plate. The device that is used for our application is a two color close focus pyrometer with a temperature range from 1000 to 3000 degrees C. The two color mode determines the temperature from the ratio of two separate and overlapping infrared bands. This device is best for measuring temperatures of partially obscured objects through viewing windows that reduce energy.

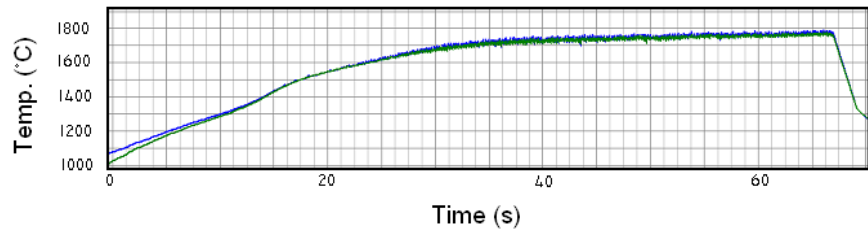


**Figure 15. Graphite surface temperature measured by the two-color IR pyrometer during an air plasma test.**

Currently, the ICP torch is capable of producing surface temperatures of over 1800 degrees C with air plasmas. These temperature values were measured on graphite which has a reliable emissivity value of  $\sim 0.9$  (Ref. 4). In the original configuration of the sample holder, there is no insulating piece between the water cooled copper holder and the graphite sample. Graphite has a very high thermal conductivity, so a significant amount of energy is being transferred to the cooled holder by conduction. In fact, the cooling water was boiling in the sample holder at these test conditions. From Fig. 15 it can be seen that the torch is capable of sustaining a steady high temperature operating condition. The dynamic start up and shut down can be seen at the beginning and end of the plot. The surface temperature appears to drift up over time which is due to a slow increase in chamber pressure.

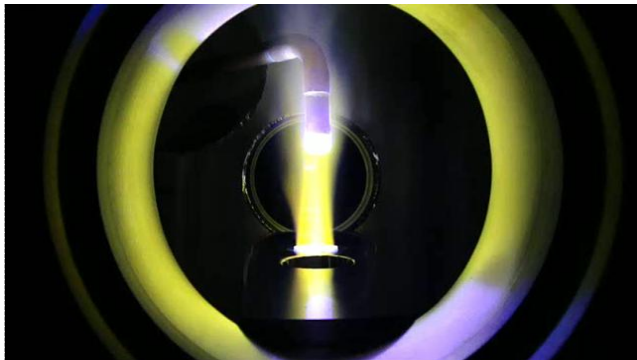


**Figure 16. Graphite sample in 100% nitrogen plasma at 100 torr**

Nevertheless, one can calculate a lower bound on the convective heat flux assuming radiative equilibrium conditions and neglecting the conduction loss, which gives a value of approximately  $70 \text{ W cm}^{-2}$  for the peak surface temperature of the test performed in Fig. 16.

#### IV.B. Slug Calorimeter Heat Flux Measurements

A thermal capacitance calorimeter is used to measure the stagnation region heat transfer rate produced by the plasma. The calorimeter is used for the purpose of calibrating the thermal environment into which test specimens are placed for evaluation. The technique assumes one-dimensional heat conduction into a cylindrical piece of material (slug) with known physical properties. Using the temperature-time curve recorded by a back-face thermocouple, and knowing the slug's dimensions and material properties, the heat flux can be calculated. Compared to other heat flux measuring devices, slug calorimeters are simple to fabricate, inexpensive and easily installed since they are not water-cooled. The primary disadvantages are its short lifespan and relatively long cool down time after exposure to the plasma flow<sup>5</sup>.

The slug device is illustrated schematically in Fig. 17. The apparatus shown is the current design of the slug calorimeter used in the UVM 30kW ICP Torch Facility. Velocity gradients must be matched, so the brass body of the calorimeter is configured with the same size and shape as that used for the ablation test samples to establish equivalent flow and experimental conditions. The slug is made of oxygen-free high-conductivity copper that is ultra-pure (99.99%) and is polished on the front face. Copper was chosen because its high thermal conductivity will minimize required exposure times for a linear thermocouple measurement. In addition copper is known to provide a high rate of surface-catalyzed recombination, which allows a measurement of the fully-catalytic heat flux. The copper slug is held in place by compressing the Teflon insulating ring when the brass body is bolted together. An annular air gap and Teflon insulator serve to minimize heat transfer to or from the body of the calorimeter, thus promoting one-dimensional heat transfer. Teflon was chosen because of its relatively high melting point and low thermal diffusivity. The air gap was limited to .05mm to reduce pressure variations across the face of the calorimeter that might cause flow in and out of the gap. A thermocouple is mechanically fixed to the back face of the copper slug and linked to a computer based data acquisition system. The brass body is conduction cooled from intimate contact with the water cooled probe and is attached using 3 set screws.

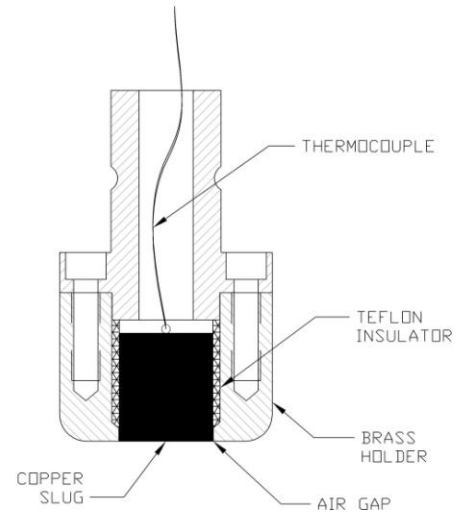


**Figure 17. Schematic of the copper slug calorimeter**

The steady state heat transfer rate is derived from the heat equation. Assuming only 1-D heat transfer along the axis, a steady heat flux on the front face, insulated boundary conditions on the back face, and a constant temperature initial condition, the heat equation can be reduced to Eq. 5.

$$q = \rho c_p \frac{dT}{dt} \quad (4)$$

Slug calorimeter data were collected for the present range of torch operation. A plot of a typical run can be seen in Fig. 18. The start-up and shut-down of the torch can be identified as well as the entry and exit of the calorimeter into the plasma flow. The exposure to the plasma flow is seen as the sharp increase in the slug back-face thermocouple reading. The slope of the temperature-time curve can be extracted from the plot. The initial and final temperature transient effects must be eliminated by using only the linear portion of the curve for the heat flux calculations.

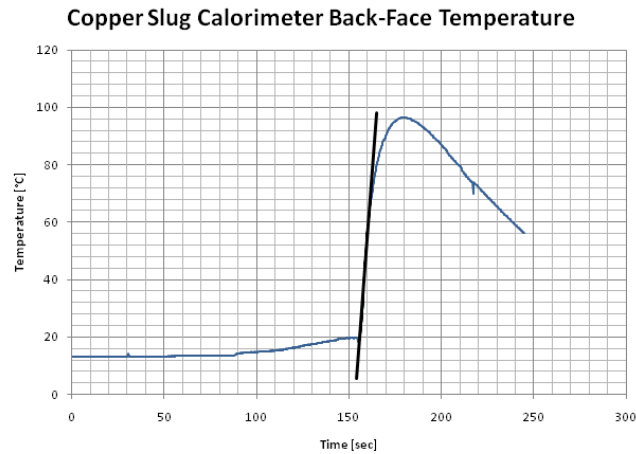


**Figure 18. Plot of the copper slug calorimeter temperature time curve through the entirety of a typical run**

The heat loss rate due to conduction can be seen from the negative slope of the temperature-time curve once the slug is removed from the plasma flow. To ensure that energy losses are minimized, the cooling rate should compare to the heating rate according to Eq. 5 (Ref. 5):

$$\left(\frac{dT}{dt}\right)_{cooling} \leq 0.05 \left(\frac{dT}{dt}\right)_{heating} \quad (5)$$

As with any calorimeter, reliability can be seen with its repeatability and its comparison with other calorimeters at the same operating conditions. For a slug calorimeter, error in the temperature time curve measurements and the appropriate use of a 1-D approximation must be considered in determining the accuracy of the calculated heat flux. The method of temperature measurement must be sufficiently sensitive and reliable to ensure accurate temperature rise data for the back face thermocouple. Attachment of the thermocouples were made with a best attempt to record true back-side temperatures. The thermocouple recording speed was appropriately chosen for the heat transfer rate level and exposure time.

The results can be seen in Table 2. The losses were calculated by applying the same linear regression to the decreasing temperature-time curve after the removal of the calorimeter. The total heat flux is the summation of the calculated heat flux and the estimated losses.

Run	Power Supply		Operating Gas	Chamber Pressure	Calculated Heat Flux	Estimated Losses	Total Heat Flux
(Date)	(kV)	(A)	(lpm)	(torr)	(W cm <sup>-2</sup> )	(W cm <sup>-2</sup> )	(W cm <sup>-2</sup> )
2010_05_11	10.0	2.7	35 N <sub>2</sub> / 17 Ar	112	81.0	3.9	<b>85.0</b>
2010_05_14	9.6	2.6	35 N <sub>2</sub> / 17 Ar	110	62.6	4.4	<b>67.0</b>
2010_05_18	9.5	2.6	35 N <sub>2</sub> / 18 Ar	120	58.7	3.9	<b>62.6</b>
2010_05_19	9.6	2.6	36 N <sub>2</sub> / 17 Ar	115	67.0	3.5	<b>70.5</b>
2010_05_20	9.1	2.5	25 CO <sub>2</sub> / .8 N <sub>2</sub> / 18 Ar	108	38.1	3.5	<b>41.6</b>
2010_05_21	9.2	2.5	24 CO <sub>2</sub> / .8 N <sub>2</sub> / 18 Ar	100	52.6	3.5	<b>56.1</b>

**Table 2. Calculated heat flux at typical power levels and operating pressures for different gas mixtures using the copper slug back face temperature data**

## **V. Summary and Future Work**

The design, construction and operation of the 30kW ICP Torch Facility at the University of Vermont have been presented. Detailed descriptions of the facility subsystems were discussed and shortcomings were noted. Heat flux and graphite surface temperature measurements from facility tests were also presented for a number of different test cases using a range of gas mixtures.

Future work will include further optimization of the tank circuit, integration of the gas and material diagnostics, and performance of aerospace material tests.

## **VI. Acknowledgements**

This work was supported by AFOSR Grant #FA 9550-08-1-0414.

## **VII. References**

<sup>1</sup>Lieberman, M. A., and Lichtenberg, A. J., *Principles of Plasma Discharges and Material Processing*, John Wiley & Sons, New York, 1994, Chap. 12.

<sup>2</sup>Playez, M., "Titan Atmosphere Plasma Characterization Using Spectroscopic Measurement Techniques," Ph.D. Dissertation, Ecole Centrale. Paris, Laboratoire D'Energetique Moleculaire et Macroscopique Combustion, June 2006

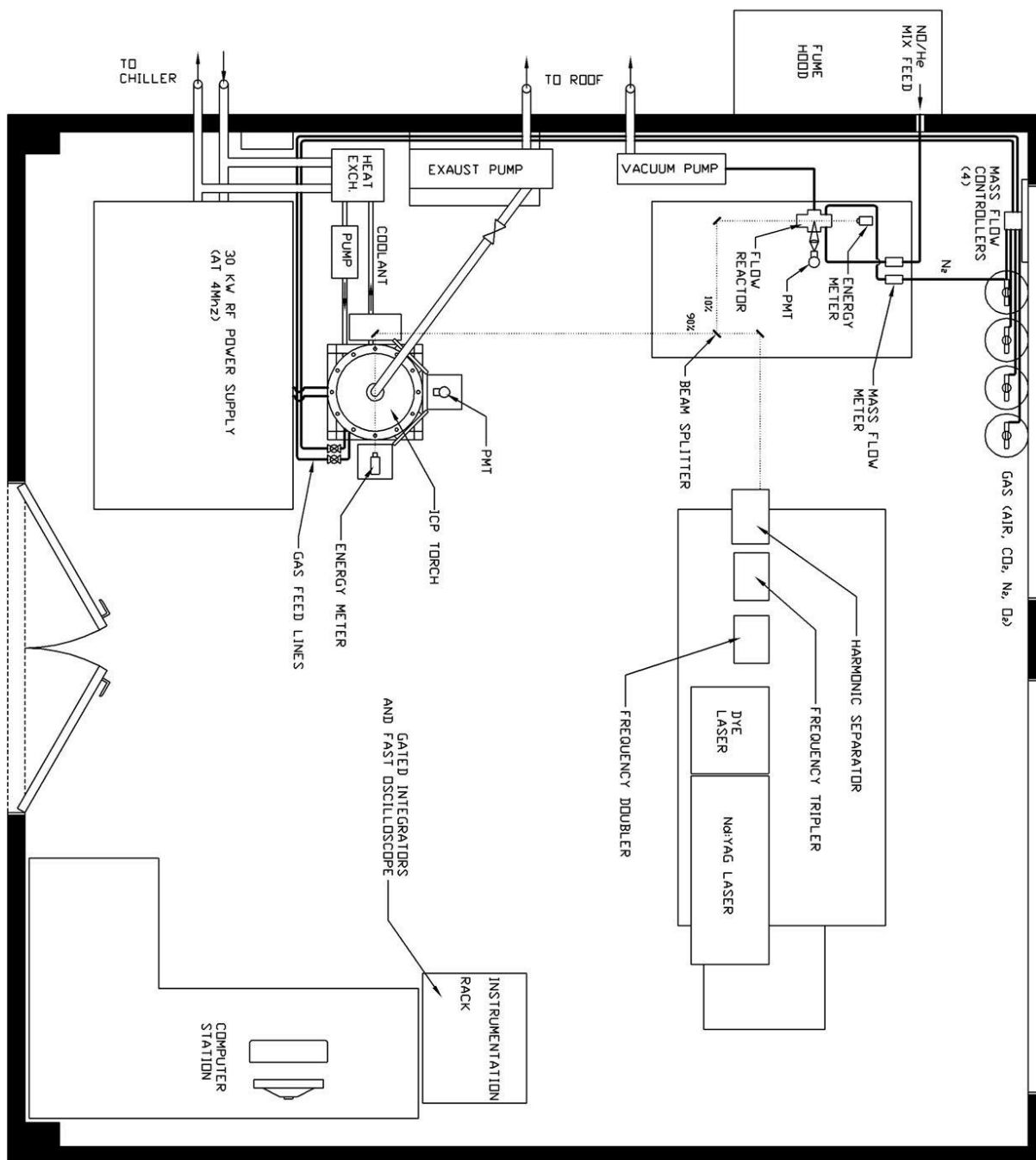
<sup>3</sup>Meyers, J., and all, "Laser Spectroscopic Investigation of Surface-Catalyzed Reactions for Mars Exploration Vehicles," The University of Vermont, Burlington, Vermont, 2010

<sup>4</sup>Vancraynest, B., "Heat Flux and Surface Temperature Measurements in High Enthalpy Plasma Flows," von Karman Institute for Fluid Dynamics, Belgium, 2002.

<sup>5</sup>"Standard Test Method for Measuring Heat-Transfer Rate Using a Thermal Capacitance (Slug) Calorimeter," ASTM.

<sup>6</sup>Tobin, C., and Uhl, J., "Hypersonic Plasma Probe," The University of Vermont, Burlington, Vermont, 2009

## VIII. Appendix



PLASMA DIAGNOSTICS LABRATORY



This article appeared in a journal published by Elsevier. The attached copy is furnished to the author for internal non-commercial research and education use, including for instruction at the authors institution and sharing with colleagues.

Other uses, including reproduction and distribution, or selling or licensing copies, or posting to personal, institutional or third party websites are prohibited.

In most cases authors are permitted to post their version of the article (e.g. in Word or Tex form) to their personal website or institutional repository. Authors requiring further information regarding Elsevier's archiving and manuscript policies are encouraged to visit:

<http://www.elsevier.com/copyright>



# High-enthalpy test environments, flow modeling and *in situ* diagnostics for characterizing ultra-high temperature ceramics

Jochen Marschall<sup>a,\*</sup>, Douglas G. Fletcher<sup>b</sup>

<sup>a</sup> SRI International, 333 Ravenswood Avenue, Menlo Park, CA 94025, USA

<sup>b</sup> University of Vermont, 201 Votey Hall, 33 Clochester Avenue, Burlington, VT 05405, USA

Available online 19 February 2010

## Abstract

Ultra-high temperature ceramic materials and composites under development as nose-tip and wing leading edge components for hypersonic flight vehicles must operate in extreme aerothermal heating environments. The performance of ultra-high temperature ceramics for this application is ultimately evaluated using high-enthalpy, long duration flow facilities that simulate the reactive gas environment encountered in hypersonic flight. In this paper, we describe the test environments generated by two types of these ground test facilities – subsonic inductively coupled plasma tunnels and supersonic arc-jet tunnels – and discuss the important roles of computational fluid dynamics modeling and *in situ* optical diagnostics for interpreting test results from a materials science perspective.

© 2010 Elsevier Ltd. All rights reserved.

**Keywords:** Ultra-high temperature ceramics; Borides

## 1. Introduction

Transition metal borides and carbides, as well as their composites with various sintering aids and glass formers, are collectively known as ultra-high temperature ceramics (UHTCs). The field of UHTC research has expanded substantially over the last decade, motivated by the unique potential of these ceramics for applications in extreme high-temperature, reactive environments.<sup>1,2</sup> A central driver for UHTC research is the need for sharp leading edge and control surface components for future generations of hypersonic flight vehicles.<sup>3–5</sup> Sharp leading edges enable vehicles with flight performance at hypersonic speeds (e.g., maneuverability, extended cross-range capability) that cannot be achieved with blunt body designs.<sup>6,7</sup> The main hurdle for sharp vehicle designs is the severe aerothermal heating environment that acts on sharp leading edges. The concentrated combination of high temperature and aggressive chemistry causes most materials to fail by melt-

ing, vaporization/sublimation, oxidation, ablation, spalling, or some combination of these processes.

While a battery of conventional mechanical and thermal tests aid in the development of UHTC materials, the performance of UHTCs intended for leading edge applications must ultimately be demonstrated in a representative aerothermal test environment. Such test environments are provided by arc-jet or inductively coupled plasma (ICP) wind tunnels which expose test articles to high-enthalpy reactive gas flows. Tests of UHTC materials in arc-jet facilities have been reported in the scientific literature by Kaufman,<sup>3</sup> Metcalfe et al.,<sup>8</sup> Wuchina and Opeka,<sup>9</sup> Opila et al.,<sup>10</sup> Gasch et al.,<sup>11</sup> Chamberlain et al.,<sup>12</sup> Savino et al.,<sup>13</sup> Monteverde and Savino,<sup>14</sup> and Zhang et al.<sup>15</sup> Tests of UHTC materials in ICP facilities have been reported by Ito et al.,<sup>16</sup> Marschall et al.,<sup>17</sup> and Playez et al.<sup>18</sup>

In this paper we discuss the test environments provided by these two types of plasma wind tunnel facilities. We highlight the coupling between the high-enthalpy reactive flow stream and the test specimen in determining UHTC material response to these environments. The importance of computational fluid dynamics (CFD) modeling of the free-stream and boundary layer flows is discussed, and the value of *in situ* diagnostics for

\* Corresponding author. Tel.: +1 650 859 2667; fax: +1 650 859 6196.  
E-mail address: [jochen.marschall@sri.com](mailto:jochen.marschall@sri.com) (J. Marschall).

documenting test conditions and monitoring UHTC evolution during testing is emphasized.

## 2. High-enthalpy test environments

### 2.1. Plasma wind tunnel facilities

The need for long-duration, high-enthalpy gas flows for the characterization and qualification of thermal-protection system (TPS) materials and components led to the development of plasma wind tunnel facilities for aerospace applications.<sup>19</sup> A variety of different designs have been investigated and implemented for plasma wind tunnels but in general all facilities consist of an electrical power supply, an input gas supply, an arc-discharge or inductively coupled heater section, a test section, and an exit gas handling system.

Arc-discharge devices in which a current passes directly through a flowing gas were developed extensively in the USA because of their large energy deposition rates. Stable arc discharges are achieved in large length-to-diameter ratio heaters constructed of segmented metal elements and fitted with magnetically spun electrodes. Various arc-jets are now in operation around the world, including facilities in the USA, Europe, and Asia.<sup>19</sup> Direct-arc heating facilities can typically operate with large test gas mass flows and with pressures on the order of 1–2 MPa within the heater, enabling supersonic flow conditions in the test section. Most constricted-arc plasma facilities use conical nozzles to produce supersonic flows and can operate stably for long test times. The United States Air Force (USAF) arc-jet facilities have been developed to simulate aero-heating for ballistic atmospheric trajectories, while the National Aeronautics and Space Administration (NASA) arc-jet facilities have been tailored to simulate lower pressure trajectories associated with upper atmospheric and planetary entry.<sup>19</sup>

In ICP devices energy is coupled into the test gas flow inductively using high-frequency, high-power, high-voltage electrical supplies. Gases flow through a quartz tube (typically) in the heater section and direct contact between the gas stream and hot metal surfaces is avoided. One advantage of the ICP design for materials science studies is that the free-stream is usually free of metal contaminants (e.g., copper) often found in arc-jet flows. Such contaminants may interfere with important chemical processes like oxidation, reactive volatilization and surface catalysis, or change important surface properties like the emittance. Although these devices were investigated in the USA,<sup>20</sup> they were developed extensively in Russia and large-scale ICP facilities are now also in operation in Europe and Asia.<sup>19</sup> These devices can generate either subsonic or supersonic flows, however because of their more limited capability for supporting high gas pressures in the heater section, most ICP testing is done in the subsonic regime.

The test environments generated by these two types of facilities differ in significant ways, both from each other and from actual flight environments. No ground facility can reproduce all features of hypersonic flight accurately, because of physical constraints and operating envelope limitations. Choices for test conditions are usually made to match particularly important

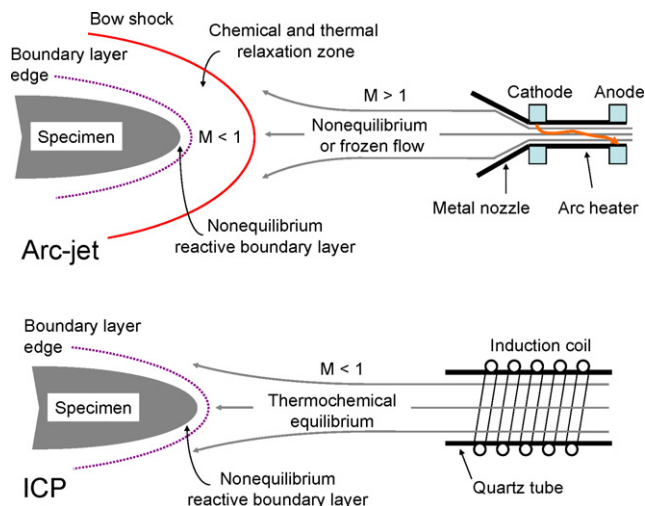


Fig. 1. Flow features for arc-jet and ICP free-streams interacting with a test specimen.

trajectory parameters like the anticipated peak heat flux, peak pressure, maximum heat load, etc. The extrapolation of ground test conditions to flight environments is an on-going area of concern and research<sup>21,22</sup> and will not be addressed further here. Rather, we focus on differences between supersonic arc-jet and subsonic ICP environments as they impact TPS materials testing in general and UHTC testing in particular.

### 2.2. Test conditions

Each plasma facility has its unique envelope of operation that limits the range of free-stream enthalpies that can be obtained. Together with the model size, shape, and chemical composition, the available free-stream enthalpy determines the heat flux that can be applied to a test specimen. Typically, the power delivered to the heater, the mass flow rate of the test gas, and the test section static pressure can be adjusted within prescribed ranges. The stagnation point conditions achieved for a particular combination of facility settings are then measured using a calibration probe (or probes) of the same geometry as the test sample, but fitted with a calorimeter to measure heat flux and a Pitot gauge to measure pressure. These calibration probes are usually made of copper and are water cooled.

Fig. 1 illustrates the salient features of the flow interactions with a test specimen for the each type of facility. An important difference between supersonic arc-jet and subsonic ICP flows is the thermochemical state of the gas approaching the test article. Because of the relative fluid dynamic and chemical relaxation time scales in arc-jet facilities, gases exiting the nozzle and flowing into the test chamber are typically in a chemically frozen or non-equilibrium state. This means that the chemical composition of the free-stream gas may differ considerably from the thermodynamic equilibrium composition associated with the translational gas temperature. In supersonic arc-jet flows the interaction of the free-stream with the test article produces a bow shock in which the gas undergoes adiabatic compression. High energy intermolecular collisions heat the gas, depositing energy

into a manifold of excited electronic, vibrational, and rotational states, and driving ionization and molecular dissociation processes. Behind the shock front, where the flow is subsonic, the residence time is now longer than typical chemical reaction times and gases undergo thermal and chemical relaxation as they approach the boundary layer edge.<sup>23</sup> The gas temperature at the boundary layer edge may be 1000s of degrees hotter than the surface of the test specimen. As the gas flow passes through the boundary layer edge to the surface, chemical reactions change the gas composition further. However, the chemical and flow time scales in the boundary layer may be such that the gas interacting directly with the specimen is not in chemical equilibrium at the surface temperature.

In contrast, in ICP facilities the flow path and timescales are typically such that gases can relax towards their thermochemical equilibrium state in the free-stream before reaching the boundary layer edge at the test article, making the prediction of the boundary layer edge composition much more straight forward.<sup>22</sup> In a subsonic ICP flow, no bow shock is produced when the flow encounters the test specimen, but a reactive boundary layer is still formed. There is still a large temperature difference between the boundary layer edge and the specimen, and similar drivers for chemical non-equilibrium in the gases at the surface exist.<sup>24</sup>

In supersonic arc-jet flows the pressure at the stagnation point of a test article is largely determined by the dynamic pressure of the flow stream, while in subsonic ICP flows the stagnation pressure is largely determined by the static pressure in the test section because the dynamic pressure of the flow stream is small. The aerodynamic shear stresses exerted on model surfaces can be much higher in supersonic arc-jet flows than in subsonic ICP flows. While UHTC materials should have sufficient mechanical strength to withstand aerodynamic shear stresses, this may not be true for developing surface oxides. At sufficiently high temperatures in oxygen-bearing environments, many UHTC materials form glassy oxide phases (e.g.,  $B_2O_3$  and  $SiO_2$ ) that permeate and seal porous poly-crystalline oxides (like  $ZrO_2$  and  $HfO_2$ ) creating a composite scale that acts as an efficient oxygen diffusion barrier.<sup>25–28</sup> Aerodynamic shear stresses may redistribute low-viscosity glassy phases and alter the formation of such composite oxide scales.

Survey probe heat flux measurements are often reported as part of UHTC test conditions, but it is important to recognize that this heat flux is a *cold wall* heat flux to a *highly catalytic* surface, which is *not the same* as the heat flux delivered to a UHTC test specimen under identical test conditions. The convective heat flux to a specimen is driven by the temperature difference between the specimen surface and the hotter gas at the boundary layer edge. A UHTC surface will reach very high temperatures during an arc-jet or ICP test because it is not actively cooled. Because of the smaller temperature difference, the *hot wall* heat flux to a hot sample surface is always lower than the *cold wall* heat flux measured by a water-cooled survey probe. In addition, a UHTC surface may be less efficient than a copper surface at catalyzing the recombination of atomic species in the flow and will therefore experience less chemical heating from exothermic surface recombination reactions like  $O + O \rightarrow O_2$ ,  $N + N \rightarrow N_2$ , and  $O + N \rightarrow NO$ .

The primary utility of cold wall heat flux measurements is to provide experimental calibration data to aid in the reconstruction of the free-stream enthalpy using CFD computations (discussed further below). Cold wall heat flux measurements are also useful for confirming the reproducibility of test conditions, but caution must be used when using free-stream enthalpy or cold wall heat flux to compare test conditions from supersonic arc-jet tests with subsonic ICP tests. Previous investigations have shown that three parameters must be replicated to match stagnation point convective heating conditions in ground test facilities: (1) stagnation point enthalpy; (2) stagnation (or impact) pressure; and (3) velocity gradient at the boundary layer edge.<sup>22,29</sup> The velocity gradient is the rate that the velocity increases as gas flows around the test article. Thus, the convective heat transfer to the same test specimen exposed to arc-jet and ICP flows with similar free-stream enthalpy and total pressure values can be substantially different, owing to the large difference in velocity gradients between subsonic and supersonic test facilities. When differences in the velocity gradients in the two types of facilities are properly considered (for example, by scaling test article dimensions appropriately) similar boundary layer edge compositions and surface heat flux values can be obtained.<sup>22,29</sup>

We note that the characterization of high-enthalpy flow test environments remains an active research area and that comparison of flow configurations and boundary layer environments can also be made on the basis of non-dimensional similarity parameters such as the Reynolds, Schmidt, and Damköhler numbers. The use of non-dimensional similarity parameters is a valid approach, but one practical aspect worth mentioning is that (with some work) the stagnation enthalpy, stagnation pressure, and velocity gradient can be measured more easily than most non-dimensional similarity parameters in arc-jet and ICP test facilities.

From a materials science perspective, and particularly for studies of UHTC oxidation, the most relevant metrics for comparing different tests are the surface temperature, the stagnation point pressure, and the gas composition at the sample surface. This information is vital for associating physical changes in test specimens with specific environmental conditions, and for developing models of thermal and chemical material response. The first two quantities are routinely measured during arc-jet and ICP tests, but the gas composition at the surface – which can be influenced both by chemical and transport kinetics – is not currently experimentally accessible.

### 3. CFD modeling

Since the chemical nature of the gas at the test specimen surface is not measured, a combination of facility data, calibration probe measurements and CFD modeling must be used to compute the gas composition at the specimen surface for each test run. This process involves two steps. First, CFD model inputs are adjusted until free-stream flow conditions result in computed heat flux and pressure values consistent with those measured using calibration probes; then the free-stream flow conditions are held fixed and the CFD model is used to compute the tem-

perature drop and the changing gas composition through the boundary layer to the sample surface.

This procedure was described in detail for a recent series of UHTC oxidation tests run in the 1.2 MW Plasmatron facility at the von Karman Institute for Fluid Dynamics (VKI).<sup>17</sup> The CFD codes used for this procedure are the VKI Boundary Layer Code<sup>24,30</sup> and the VKI ICP Code,<sup>31,32</sup> both of which use the PEGASE library to perform thermodynamic and transport property calculations.<sup>33</sup> The ICP code solves the time-averaged magneto-hydrodynamic equation at low Mach and low magnetic Reynolds numbers, assuming axisymmetric flow and local thermodynamic equilibrium, to simulate the flow inside the plasma torch and around the test article in the vacuum chamber. The Boundary Layer Code solves the boundary layer equations for an axisymmetric or two-dimensional, steady, laminar flow of chemically reacting gas over a catalytic surface, including thermal and chemical non-equilibrium. The temperature and velocity at the boundary layer edge are adjusted until the computed and measured heat flux agrees.

At NASA Ames Research Center, arc-jet flows are computed using the Data Parallel Line Relaxation (DPLR) code.<sup>34</sup> DPLR is a parallel multiblock finite-volume code that solves the Navier–Stokes equations including finite-rate chemistry and the effects of thermal non-equilibrium. The code is used to compute non-equilibrium expanding flow in the arc-jet nozzle and supersonic jet entering the test section, as well as the reacting flow around test articles.<sup>35–37</sup> Thermodynamic properties are taken from NASA Glenn curve fits.<sup>38</sup> Transport properties are computed using the self-consistent effective binary diffusion method<sup>39</sup> and expressions and mixing rules presented by Gupta et al.,<sup>40</sup> together with collision integrals compiled by Wright et al.<sup>41,42</sup> Simulations are typically started at the nozzle throat assuming thermochemical equilibrium flow properties and some radial profile of enthalpy and mass flux. Facility and calibration data include measurements of the chamber pressure, mass flow rate, and test section pressure, calorimeter probe heat flux and pressure measurements. The total enthalpy of the arc-jet flow and its radial distribution are inferred from facility data and previous survey measurements. In the CFD reconstruction, these inferred values and distributions serve as the starting point for iterative adjustments to match computational predictions to the heat flux measured by the calibration probe.

The energy balance at the surface of a test article or calibration probe is the key relationship that couples the gas-phase and the solid material. For an environment free of gas radiation, the energy balance for any non-ablating/non-pyrolyzing material surface can be written as

$$q_{conv} + q_{chem} = q_{rad} + q_{cond}, \quad (1)$$

where the terms on the left-hand side account for convective and chemical heating by the gas stream and those on the right-hand side represent cooling by radiation and in-depth heat conduction. With some simplifying assumptions (a sensible gas enthalpy convective transfer coefficient representation, independent surface recombination of O and N atoms with equal catalytic efficiencies, negligible gas radiation) this equation can

be expanded as

$$C_H [H_e(T_e) - H_s(T_s)] + \gamma'(T_s) \Delta E_{O_2} n_O \sqrt{\frac{RT_s}{8\pi M_O}} + \gamma'(T_s) \Delta E_{N_2} n_N \sqrt{\frac{RT_s}{8\pi M_N}} = \varepsilon \sigma T_s^4 - k(T_s) \frac{dT}{dx} \Big|_s, \quad (2)$$

where  $C_H$  is the convective transfer coefficient;  $H_e$  and  $H_s$  are the gas enthalpies at the boundary layer edge and at the surface;  $\Delta E_{O_2}$  and  $\Delta E_{N_2}$  are molecular dissociation energies;  $n_O$  and  $n_N$  are atom number densities above the surface;  $M_O$  and  $M_N$  are molar masses;  $R$  is the universal gas constant;  $T$  is temperature;  $\sigma$  is the Stefan–Boltzmann constant; and  $x$  is the coordinate into the surface. Eq. (2) also shows how the surface energy balance depends explicitly on temperature-dependant surface and bulk material properties: the total catalytic efficiency  $\gamma'$ , the emittance  $\varepsilon$ , and the thermal conductivity,  $k$ . The total catalytic efficiency is defined as  $\gamma' = \gamma\beta$ , where  $\gamma$  is the species recombination efficiency (the fraction of collisions with the surface that result in atom loss) and  $\beta$  is the energy accommodation coefficient (the fraction of exothermic reaction energy transferred to the surface).

In calibration measurements the right-hand side of Eq. (2) is measured directly using water-cooled calorimeters. Then CFD inputs are adjusted to reproduce this calibration heat flux measurement, usually with values of  $\gamma'$  fixed at 1 (a fully catalytic surface) and  $T_s$  fixed to a low temperature like 300 K (a cold wall). This process derives the convective transfer coefficient  $C_H$  and the boundary layer edge temperature  $T_e$  for a particular test condition, quantities that are then kept fixed in simulations seeking to reproduce surface temperatures subsequently measured during UHTC tests.

When  $q_{cond}$  is negligible, and with  $C_H$ ,  $T_e$ , and  $T_s$  fixed, Eq. (2) shows that the energy balance is determined by  $\gamma'$  and  $\varepsilon$  through the chemical and surface radiation fluxes. (For sharp UHTC test articles, a thermal model of the heat transfer within the UHTC is likely required to evaluate  $q_{cond}$ . However for other configurations, like stagnation point testing with disk specimens in a flat-faced cylinder configuration,  $q_{cond}$  can be set to zero with minimal error.) If a numerical value is assigned to the surface emittance, the total catalytic efficiency can be adjusted iteratively until Eq. (2) is satisfied, and the gas composition at the surface is computed simultaneously. In practice, it is not straightforward to choose the “correct” value of emittance for a UHTC component at high temperature.<sup>17</sup>

As an illustrative example of the process described above, we show some results obtained for a recent series of stagnation point oxidation tests performed in the VKI Plasmatron on UHTC specimens of a hot-pressed ZrB<sub>2</sub> material containing 30 volume percent SiC (termed ZrB<sub>2</sub>–30SiC).<sup>17</sup> Tests were performed at static chamber pressures of 10<sup>4</sup> Pa with an air mass flow rate of 16 g s<sup>−1</sup> over a range of Plasmatron powers from 150 to 210 kW.

The upper portion of Fig. 2 shows the cold wall heat flux measured by a calibration probe and the steady-state UHTC sample surface temperature measured using a two-color pyrometer during each test run. Both the cold wall heat flux and the

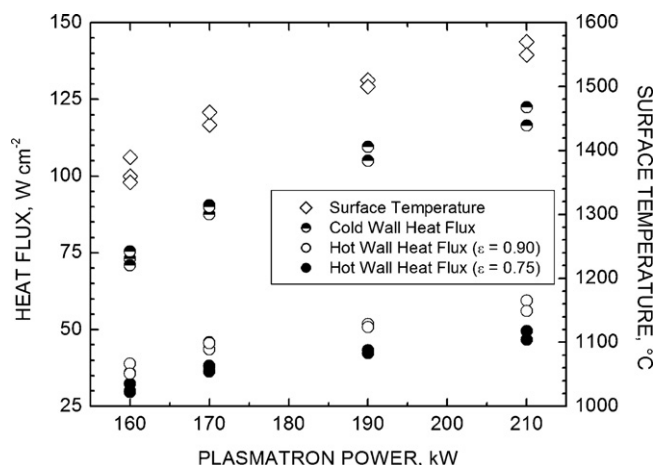


Fig. 2. Heat fluxes and surface temperatures versus Plasmatron power.<sup>17</sup> The cold wall heat flux is measured by a calibration probe and the sample surface temperature is measured by a two-color pyrometer during each test run. The hot wall heat fluxes are estimated from  $q_{hw} = \epsilon \sigma T_s^4$  with  $\epsilon = 0.90$  and  $\epsilon = 0.75$ , assuming  $q_{cond} \approx 0$ .

specimen surface temperature increase with Plasmatron power as expected. The lower portion of Fig. 2 shows the hot wall heat flux for each test run computed from  $q_{hw} = \epsilon \sigma T_s^4$  with  $\epsilon = 0.90$  and  $\epsilon = 0.75$ , assuming  $q_{cond} \approx 0$ . Both values of emittance are reasonable estimates for oxidized ZrB<sub>2</sub>–SiC composites.<sup>14,17,43</sup> Without an *in situ* method for determining the high-temperature emittance during testing, such a level of uncertainty (~15%) in emittance is unavoidable. Note that the hot wall heat fluxes are only about half of the corresponding cold wall heat fluxes, which suggests that the surface catalytic efficiencies of the oxidized UHTC surface must be low.

Fig. 3 plots the total catalytic efficiency obtained for each test condition from the surface energy balance constraint, for values of  $\epsilon = 0.90$  and  $\epsilon = 0.75$ . The derived catalytic efficiencies are much less than 1 consistent with a surface of low catalytic activity. Catalytic efficiencies derived for  $\epsilon = 0.90$  are 2–6 times

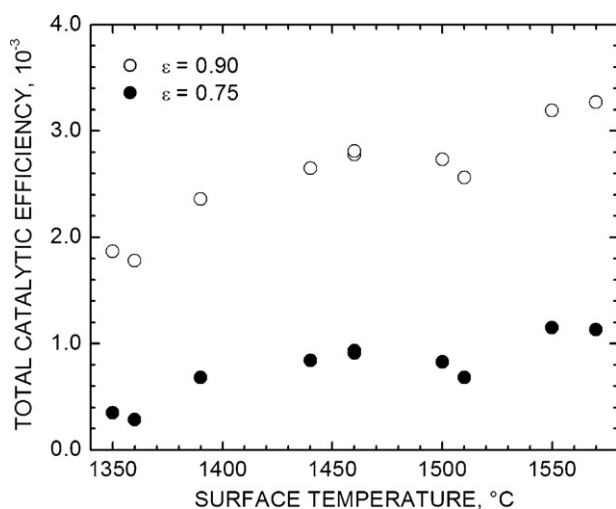


Fig. 3. Recombination efficiency versus surface temperature calculated for surface emittances of 0.75 and 0.90.<sup>17</sup> The total catalytic efficiencies for O + O and N + N are assumed identical.

higher than those for  $\epsilon = 0.75$ . Thus uncertainties in emittance become amplified in derived catalytic efficiencies.

Fig. 4 shows the calculated number densities of O, N, N<sub>2</sub>, O<sub>2</sub>, and NO at the UHTC surface for emittance values of 0.90 and 0.75. N<sub>2</sub>, O and N (in that order) are the dominant species with number densities around 10<sup>23</sup> molecules per cubic meter; the number densities of O<sub>2</sub> and NO are about 2 orders of magnitude smaller. Atomic oxygen number densities are relatively unaffected by the choice of emittance values, but atomic nitrogen number densities computed for  $\epsilon = 0.90$  are only 55–75% of the magnitudes computed for  $\epsilon = 0.75$ . The number densities of the minor species are larger for  $\epsilon = 0.90$  than  $\epsilon = 0.75$ , by factors of about 3–7 for O<sub>2</sub> and about 2–3.5 for NO.

As this example demonstrates, considerable uncertainties can propagate into CFD-derived quantities like catalytic efficiency and surface gas composition, by errors in experimental measurements and material properties. Additional, and hard to quantify, error is also undoubtedly present in the details of the formulations, assumptions, solution procedures, and the chemical, transport and thermodynamic data employed in particular CFD codes. Nevertheless, CFD modeling is a crucial element of UHTC testing, because it offers the best tool currently available for evaluating the state of the gas interacting directly with the test surface specimen. It is also the only practical way to estimate quantities like the surface shear stress or to map out changes in gas composition over the surface of more complex three-dimensional UHTC test articles.

We note that most published accounts of UHTC testing in arc-jet or ICP facilities have not reported quantitative estimates of the gas composition at the sample surface during testing. From a materials science perspective, this makes the comparison of different experiments problematic and the construction of materials response models more difficult. The value of UHTC arc-jet and ICP test results would be greatly increased if surface gas compositions, and the numerical procedures used to estimate them, were routinely reported. Further benefits would result from mea-

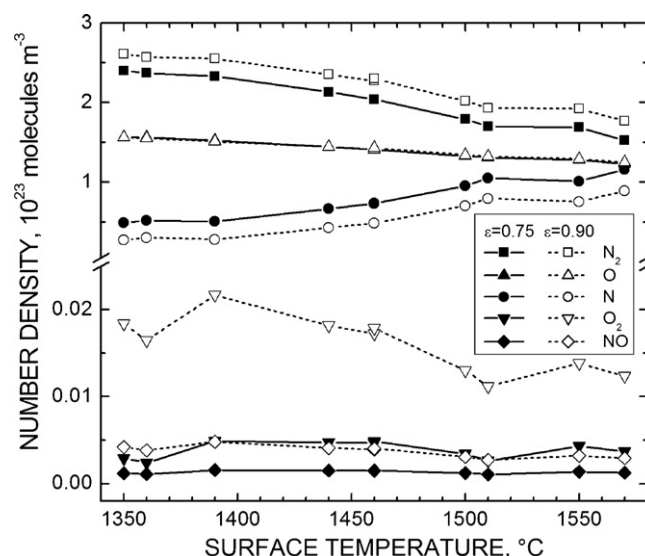


Fig. 4. Number densities at specimen surfaces versus surface temperature, computed for surface emittances of 0.75 and 0.90.

surements of boundary layer gas compositions and gradients, as discussed in the following section.

#### 4. Optical diagnostics

In this section we examine different optical techniques for obtaining information about the test environment and the evolution of UHTC specimens exposed to high-enthalpy flows.

##### 4.1. Surface radiometry

Surface temperature is perhaps the most important quantity required for the interpretation of test results. Surface temperatures are typically measured *in situ* by collecting thermal radiation emitted by the hot specimen using one-color or two-color radiometers. One-color radiometers collect radiation over a single wavelength range, while two-color radiometers collect radiation over two wavelength ranges (which may overlap). Both types of radiometers are calibrated as a function of emission temperature using blackbody radiation sources (special furnaces with an effective normal emittance approaching 1). One-color radiometers require knowledge of the specimen emittance over the detection wavelength range to convert radiation intensity to surface temperature. Two-color radiometers only require that the ratio of emittance values for the two detection ranges be known; for a surface with wavelength-independent emittance this ratio is 1. Typical experimental issues include transmittance losses due to windows, interference by absorbing gases, parasitic collection of reflected light, and geometric limitations for viewing the sample surface. Single-color radiometers typically respond to the average temperature in the field of view, while two-color radiometers tend to reflect the peak temperature in the field of view. Facility geometry usually dictates that specimen surfaces be viewed at non-normal incidence, enlarging the surface area seen by the radiometer. The possibility of non-uniform surface temperatures in the field of view must be considered for UHTC specimens with small stagnation regions like sharp wedges or cones.

Radiometry can also be used to obtain information about the emittance of UHTC specimens at high temperature. Laboratory measurements of UHTC emittance at high temperature are difficult and rare. The emittance measurements of Scatteia et al. on various UHTC composites (ZrB<sub>2</sub>–15SiC, ZrB<sub>2</sub>–15SiC–2MoSi<sub>2</sub>, and ZrB<sub>2</sub>–15SiC–10HfB<sub>2</sub>) are notable in this regard.<sup>43,44</sup> Scatteia et al. have also demonstrated how UHTC emittance is influenced by surface finish and oxidation. Because it may be difficult to reproduce oxidized UHTC surfaces in the laboratory that are the same as those formed in the low-pressure, highly dissociated-oxygen environments of arc-jet and ICP flows, *in situ* measurements would be preferred.

If both one- and two-color radiometers are trained on the same surface location, surface temperature can be measured using the two-color instrument and, with the surface temperature known, the *in situ* emittance can be derived from the one-color instrument. Such a procedure was used by Monteverde and Savino<sup>14</sup> to find  $\varepsilon \cong 0.9$  for a hot-pressed ZrB<sub>2</sub>–15SiC composite during testing in a 80-kW plasma torch. This type of measurement

could in principle be done using a single instrument, by calibrating and collecting both channels of a two-color radiometer. A further extension of this procedure would be the use of a spectral radiometer to capture wavelength-resolved emission intensity over a broad wavelength range. The captured intensity curve is fit by the Planck blackbody radiation function,  $E_b(\lambda, T)$ , convoluted with a wavelength-dependent emittance, yielding both surface temperature and emittance values. Spectral radiometers are expensive instruments and their application in arc-jet or ICP testing of UHTC materials has not yet been reported.

Emittance is a function of wavelength, emission direction, and temperature. The surface energy balance requires the total hemispherical emittance – the emittance averaged over all wavelengths and emission directions – as input, where it plays a crucial role in the determination of surface catalytic efficiency and thus the computed gas-phase species concentrations above the surface. The emittance obtained by Monteverde and Savino<sup>14</sup> yields a directional value valid over the wavelength range of their one-color radiometer. The direct use of this value in the surface energy balance implies assumptions of wavelength independence (a gray surface) and directional independence (a diffuse surface) which may not be true. Extension of this method using a spectral radiometer would produce a wavelength-dependent directional emittance that can be averaged over wavelength to yield a total, directional emittance value. However, some assumptions or approximations would still have to be made about the relationship between total directional and total hemispherical emittance before this derived value could be used in the surface energy balance. Since it does not seem possible to make a total hemispherical emittance measurement *in situ*, the best available alternative is probably the extrapolation of *in situ* emittance measurements with the directional and/or spectral dependencies documented in pre- and post-test laboratory measurements.

##### 4.2. Gas emission spectroscopy

The radiation emitted by gases in the free-stream or in the near-surface region of test specimens contains information about the species present. Atoms and molecules emit radiation when they transition from higher to lower energy states. Each species has a unique set of energy levels and the energies of emitted photons correspond precisely to differences between these levels. Emission spectroscopy collects this emitted light and disperses it by wavelength, generating spectra with characteristic intensity features (atomic lines and molecular bands) that can be associated with individual species. Emission is a path-integrated measurement technique without spatial resolution along the light collection axis. Reconstruction of the spatial distribution of emission requires measurements along multiple axes and/or assumptions of symmetry together with a mathematical procedure known as an Abel inversion.<sup>45</sup> Further complications ensue if the gas is optically thick and significant re-absorption of emitted radiation occurs along the collection axis.

During the Plasmatron testing of hot-pressed ZrB<sub>2</sub>–30SiC materials described in Section 3, prominent bluish-green emissions were observed around the test articles. These emis-

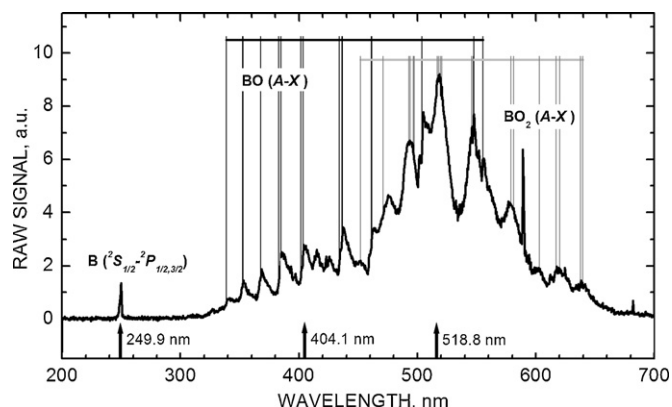


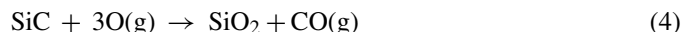
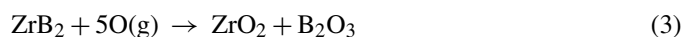
Fig. 5. Raw signal versus emission wavelength 55 s after injection of sample into the free-stream. Background emissions from the Plasmatron free-stream have been subtracted to remove contributions from the  $N_2^+$  band system. The strong line at 589 nm can be assigned to sodium. The bandhead positions for BO and  $BO_2$  are from Spalding et al.<sup>46</sup> and atomic lines were identified from the NIST Atomic Spectra Database.<sup>47</sup> Arrows indicate the wavelengths used to monitor B, BO, and  $BO_2$  as a function of test time.

sions first appeared and intensified as the sample temperature increased, then reached a plateau, and finally decreased in intensity at longer test times. Follow-on tests were performed in which emission spectra were collected directly adjacent to the specimen surface as a function of test time. Light was captured through an aperture, focused onto the end of an optical fiber by a spherical mirror, and transmitted to a spectrometer with a wavelength range of 200–1100 nm and a resolution of 0.25 nm. Spectra were collected at 1 Hz during the test.

These measurements confirmed that the visible emission originated from electronically excited BO and  $BO_2$  molecules, and in addition detected ultraviolet emission associated with atomic boron. An example of these spectra is shown in Fig. 5, which plots background-subtracted raw signal against emission wavelength (background subtraction removes  $N_2^+$  emissions originating from the Plasmatron free-stream). The band head positions for the BO ( $A^2\Pi \rightarrow X^2\Sigma^+$ ) and  $BO_2$  ( $A^2\Pi_u \rightarrow X^2\Pi_g$ ) systems are from Spalding et al.<sup>46</sup> and the B ( $2S_{1/2} \rightarrow 2P_{1/2,3/2}$ ) doublet was identified from the NIST Atomic Spectra Database.<sup>47</sup> Since all boron species must originate from  $ZrB_2$ , emission spectroscopy in this case provides an *in situ* monitor for the oxidation of the UHTC composite and the volatilization of boron from the resulting oxide scale.

UHTC composites containing both  $ZrB_2$  and SiC oxidize to form complex oxide scales with an outer glassy layer rich in silica and an inner layer depleted of SiC. The structure of these oxide scales has been extensively investigated with post-test analytic techniques (microscopy, X-ray diffraction, chemical analysis),<sup>26,48,49</sup> and their formation hypothesized in terms of transport processes and thermodynamic arguments.<sup>27,28</sup>

In dissociated-oxygen environments, the passive oxidation of zirconium diboride forms zirconia and boron oxide, and the passive oxidation of silicon carbide forms silica and carbon monoxide:



The oxidation rate of  $ZrB_2$  at moderate temperatures (below 1000 °C) is significantly faster than the oxidation rate of SiC. Therefore the initial oxide scale is expected to be predominantly  $B_2O_3$ . Amorphous  $B_2O_3$  has a very low softening temperature (~560–630 °C)<sup>50</sup> and liquid  $B_2O_3$  seals the surface slowing inward oxygen transport. At higher temperatures, the SiC oxidation rate increases and the oxide scale becomes a borosilicate glass. However liquid  $B_2O_3$  has a much larger vapor pressure than silica and boron oxides are predicted to volatilize preferentially from the oxide surface leaving a silica rich glass. As the glassy scale thickens and becomes more silica rich, inward oxygen diffusion slows further and oxygen concentrations at the reaction interface decrease. Under these conditions active SiC oxidation becomes favored over  $ZrB_2$  oxidation, slowing  $B_2O_3$  production and leading to the formation of a porous SiC-depleted sub-layer via:



Gaseous SiO formed at the bottom of the SiC-depleted layer diffuses to the top of that layer where it is thought to condense, augmenting the glassy top scale from below.

In detail this process is quite complicated, involving heterogeneous media, transitions between different controlling chemistries, the growth of multiple oxide layers, moving interfaces, changing glass compositions, evolving transport properties, etc. However, a simple “shape function” for the expected time variation of boron species volatilization can be constructed based on the premise that boron oxide is formed by reaction (3) at the bottom of the glassy scale and diffuses through the scale to the surface where it evaporates according to a Hertz–Langmuir relationship. The diffusion and evaporation fluxes can be written in terms of the boron oxide concentrations at the reaction interface,  $C_{B_2O_3,i}$ , and the outer surface,  $C_{B_2O_3,s}$ , as

$$J_{B_2O_3,dif} = D_{B_2O_3} \frac{C_{B_2O_3,i} - C_{B_2O_3,s}}{\Delta_{glass}} \quad (6)$$

$$J_{B_2O_3,ev} = \frac{P_{B_2O_3,v}}{\sqrt{2\pi M_{B_2O_3} RT}} \frac{C_{B_2O_3,s}}{[\rho/M]_{glass}} \quad (7)$$

These expressions can be combined by assuming diffusion and evaporation fluxes are in quasi-steady-state at any time:

$$J_{B_2O_3,ev} = \frac{C_{B_2O_3,i}}{\left( \sqrt{2\pi M_{B_2O_3} RT} [\rho/M]_{glass} / P_{B_2O_3,v} \right) + (\Delta_{glass} / D_{B_2O_3})} \quad (8)$$

Both the vapor pressure and the diffusion coefficient are presumed to follow Arrhenius dependencies on temperature:  $P_{B_2O_3,v} \propto \exp(-E_v/RT)$  and  $D_{B_2O_3} \propto \exp(-E_D/RT)$ . If parabolic scale growth is assumed,  $\Delta_{glass} \propto \sqrt{t}$ , and if falling boron oxide production with growing scale thickness is approximated by an inverse power law,  $C_{B_2O_3,i} \propto t^{-n}$ , the following shape function for the temperature and time dependencies of the

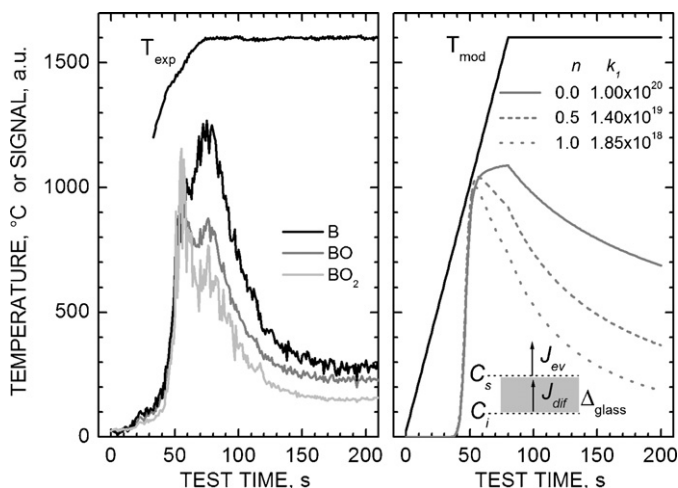


Fig. 6. Experimental temperature and emission signal history collected during a Plasmatron test of a hot-pressed  $\text{ZrB}_2\text{--}30\text{SiC}$  specimen (left-hand panel) and representative volatilization profiles computed by Eq. (9) (right-hand panel). Emission was collected at the three wavelengths indicated in Fig. 5; the radiometer cut-on temperature was  $\sim 1100^\circ\text{C}$ . The  $\text{B}_2\text{O}_3$  fluxes and concentrations leading to the shape function model are illustrated in the right-hand panel. Shape functions were computed with  $k_2 = 10^4$ ,  $E_v = 320$  kJ/mole, and  $E_D = 10$  kJ/mole, and the values of  $n$  and  $k_1$  listed on the figure.

boron oxide vaporization flux results:

$$J_{\text{B}_2\text{O}_3, \text{ev}} \cong \frac{k_1 t^{-n}}{\sqrt{T} \exp(E_v/RT) + k_2 \sqrt{t} \exp(E_D/RT)}, \quad (9)$$

where  $k_1$ ,  $k_2$ ,  $n$ ,  $E_v$ , and  $E_D$  are constants.

Fig. 6 compares the experimental temperature and emission signal history (in the left-hand panel) collected during a Plasmatron test to some representative volatilization profiles (in the right-hand panel) computed by Eq. (9) for a piecewise linear temperature history and several numerical choices of constants. The experimental emission signals were collected at the wavelengths indicated in Fig. 5; the experimental temperature was collected by a radiometer with a low temperature cut-on of  $\sim 1100^\circ\text{C}$ .  $E_v$  was fixed at a low 10 kJ/mole on the premise that boron diffusion in high temperature amorphous or liquid silica is very fast.  $E_D$  was adjusted to 320 kJ/mole to reproduce the sharp rise in boron emission signatures observed between 40 and 50 s. The activation energy predicted by thermodynamic calculations for the vapor pressure of  $\text{B}_2\text{O}_3$  over liquid boron oxide is closer to 380 kJ/mole.<sup>25,51</sup> The decay of the shape function with time is controlled by the exponent  $n$ . Computations are shown for  $n = 0$ , 0.5 and 1.0, with  $k_2$  fixed to  $10^{14}$  and  $k_1$  adjusted to maintain similar peak magnitudes for all profiles and to put the shape function on the same (arbitrary) scale as the emission data.

In general this very simple model captures the qualitative trends seen in the emission data quite well. The largest exponent ( $n = 1$ ) seems to reproduce the relatively steep emission signal decay the best. This is consistent with the idea that the concentration of  $\text{B}_2\text{O}_3$  produced at the reaction interface should vary inversely with time *at least as fast as* the scale grows and probably faster as the decreasing oxygen pressure at the interface begins to favor active SiC oxidation over  $\text{ZrB}_2$  oxidation.

At higher temperatures (above  $\sim 1750^\circ\text{C}$ ), the vapor pressure of silica increases significantly and a similar process of volatilization from the UHTC oxide scale should lead to Si-containing species in the gas-phase. Hirsch et al.,<sup>52</sup> Altman et al.,<sup>53</sup> and Jentschke et al.<sup>54</sup> have monitored Si atom densities in front of C/C–SiC composites exposed to nitrogen–oxygen plasma flows, using high-resolution spectroscopy of Si I multiplet emissions in the 250–253-nm range. Herdrich et al.<sup>55</sup> observed Si emission near 252 nm and 288 nm while testing SiC specimens in oxygen–nitrogen plasmas, and also captured emission from  $\text{SiO}_2$  molecules near 423 nm. Emission from SiO molecules was not reported in any of these studies, which is surprising given that reaction mechanism (5) should have been operating under some of the test conditions reported.

#### 4.3. Laser induced fluorescence

Laser induced fluorescence (LIF) is a species selective, non-intrusive diagnostic that has been widely applied for the characterization of combustion and plasma environments.<sup>56,57</sup> A pulsed, tunable laser source is used to generate monochromatic light at a unique atomic or molecular absorption wavelength. The absorbed photon energy excites the target species to a higher electronic energy level, from which it subsequently decays to a lower energy level (or levels) emitting radiation at a characteristic wavelength (or wavelengths).

One advantage of the LIF technique is that ground-state species populations can be probed, whereas emission spectroscopy detects only electronically excited species. Even at relatively high temperatures, the ground electronic state populations typically predominate over the populations in higher electronic levels. Another advantage of LIF is that spatially resolved measurements are more easily made and interpreted than by emission spectroscopy, since the fluorescence collection optics field-of-view and the excitation laser beam axis can be independently oriented to intersect at a desired location, as shown schematically on the left side of Fig. 7. Generally speaking LIF detection works best for light atoms and diatomic molecules.

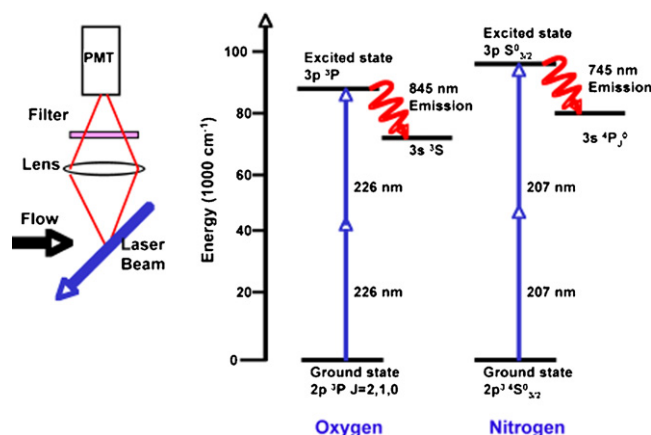


Fig. 7. Energy level diagrams for two common two-photon LIF schemes for probing atomic oxygen and atomic nitrogen. The spatial resolution of the LIF approach is indicated by the cartoon at the left.

Applications of LIF to plasma stream characterization typically involve measurement of three variables: translational temperature, convective velocity, and species concentration. Air and nitrogen plasma species probed by LIF have included O atoms, N atoms, and nitric oxide (NO).<sup>58–62</sup> For NO, single-photon excitation in either the ultraviolet  $\gamma$  band ( $A \leftarrow X$ ) or  $\beta$  band ( $B \leftarrow X$ ) is possible. However, the large energy level spacing of the oxygen and nitrogen atoms requires a two-photon excitation scheme, and the excitation cross sections are correspondingly smaller.<sup>63–66</sup> The energy levels involved in common two-photon excitation schemes for atomic oxygen and nitrogen are shown in the center and right side of Fig. 7. Atomic nitrogen is a useful target species for highly dissociated air or nitrogen plasmas, because its concentration is a sensitive indicator of the degree of plasma dissociation.<sup>58,59</sup> Atomic oxygen number densities are critical for quantifying both passive and active surface oxidation processes. Both atomic species are involved in exothermic surface recombination processes that can contribute substantially aerothermal heating.

The experimental arrangement for probing either atomic oxygen or nitrogen is essentially the same, as shown in Fig. 8. A Nd:YAG-pumped dye laser provides the fundamental output, which is converted by the appropriate tripling crystal arrangement to the desired ultraviolet, two-photon wavelength. As indicated in the figure, the ultraviolet output is split into three different paths. The first is directed toward the plasma stream (either ICP or arc-jet), while the other two paths are directed toward a NO reference cell and a microwave-discharge flow reactor, respectively. The NO cell is used to assess the laser performance and to guide laser tuning toward the relatively sparse two-photon excitation wavelengths. Within the flow reactor, the microwave discharge creates a stable, non-equilibrium population of atoms at known pressure and temperature, and the fluorescence from this population can be used to calibrate the fluorescence signals from the plasma stream. This calibration enables measurement of translation temperature, flow velocity (depending on the facility and beam orientation), and number density of the target species.

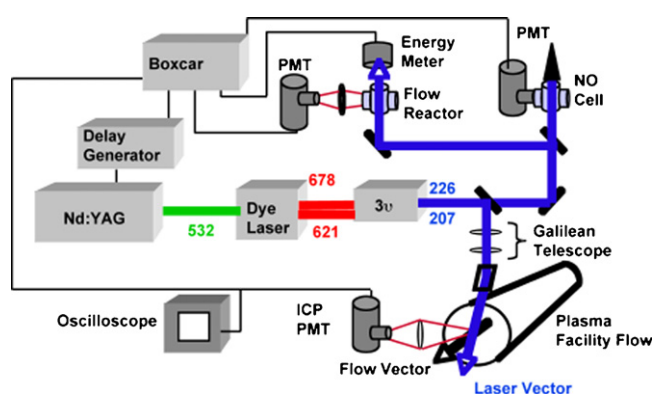


Fig. 8. Schematic of the experimental configuration for two-photon LIF implementation in arc-jet and ICP facilities. In addition to measuring LIF from the plasma facility, measurements are made in a nitric oxide cell for laser wavelength monitoring and in a flow reactor for calibration of the facility measurements. The temperature and atomic number density in the flow reactor are known independently of the laser measurements.

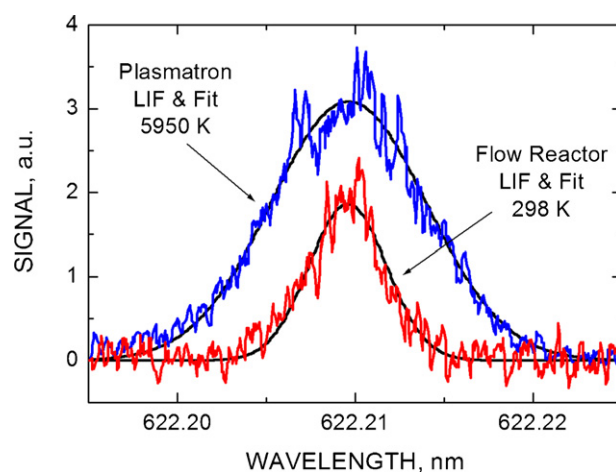


Fig. 9. Two-photon LIF signals from excitation of the 207-nm transition of atomic nitrogen at the boundary layer edge in the VKI Plasmatron ICP Torch Facility. Despite the fact that the beam is angled with respect to the axial stream velocity (as shown in Fig. 8) the subsonic flow speed does not provide a measurable shift between the flow-reactor and ICP stream transition line centers. The spectral fit assumes that Doppler broadening is the dominant line broadening mechanism.

An example of atomic nitrogen fluorescence acquired in an ICP facility is shown in Fig. 9, where the atomic nitrogen fluorescence is plotted as a function of the dye laser fundamental wavelength. The broader of the two traces is the signal collected from plasma stream at the boundary layer edge and the narrower, less noisy signal is from a microwave-discharge flow reactor. The smooth curves for each LIF signal are nonlinear least-squares fits to the line profiles using a spectral model that includes the relevant broadening mechanisms and uses the total line width as a fitting parameter. Line shape fit results from the flow reactor signal are used to extract information from the plasma stream measurements as explained in the following paragraphs. Finally, the temperature value derived for this particular measurement is indicated on the figure, along with the flow reactor temperature used to extract the laser line width.

The translation gas temperature is derived from a measurement of the total width of the transition once the laser line width is determined from the flow reactor line shape as

$$T = \frac{M_N c^2}{8 \ln(2) k_B n_A \hat{v}^2} \left[ \Delta \hat{v}_{T,F}^2 - \left( \Delta \hat{v}_{T,R}^2 - \Delta \hat{v}_{D,R}^2 \right) \right], \quad (10)$$

where  $M$  is the molar mass,  $c$  is the speed of light,  $k_B$  is the Boltzmann constant,  $n_A$  is Avogadro's number, and  $\hat{\nu}$  is the transition frequency in  $\text{cm}^{-1}$ . The different widths  $\Delta\hat{\nu}^2$  (also in  $\text{cm}^{-1}$ ) are labeled with subscripts that designate Total or Doppler and Flow or Reactor. The flow velocity can be determined from the Doppler shift of the central transition wavelength,  $\lambda$ , as

$$v = \frac{c \Delta \lambda}{\lambda \cos \theta}, \quad (11)$$

and only a separate measurement of the angle between the velocity and laser propagation vectors,  $\theta$ , is needed. While the Doppler shift in the free-stream of supersonic arc-jet facilities is quite large, and can be used to reliably measure the free-stream veloc-

ity, the Doppler shift in subsonic ICP facilities is too small for velocity determination, as is clearly evident in Fig. 9.

Finally, the local number density of atomic nitrogen is determined from integrated LIF signal. Several additional measurements are required to obtain absolute values of number density, including characterization of the fluorescence collection efficiency, the temporal and spatial characteristics of the laser beam, and finally the use of either a known N-atom reference population, a rare gas calibration,<sup>67–69</sup> or a two-photon excitation cross-section measurement.<sup>64–66</sup> For the latter approach, the expression for nitrogen atom number density is

$$n_N = \frac{4\pi}{D} \frac{\tau_{rad}}{\tau_{obs}} \frac{A_p}{\int F^2(t) dt} \frac{(hv)^2}{G^{(2)}\sigma^{(2)}} \int \frac{S_N}{E_p^2}(\omega) d\omega, \quad (12)$$

where  $S_N$  is the LIF signal in volts,  $\tau_i$  are the radiative and observed lifetimes,  $A_p$  is the beam area,  $D$  is the collection optics calibration factor,  $F^2(t)$  is the square of the temporal laser pulse shape and the  $G^{(2)}\sigma^{(2)}$  product represents the two-photon LIF cross section.

Two-photon LIF has been implemented in arc-jets to characterize the free-stream conditions<sup>58,59</sup> and to investigate free-stream property gradients.<sup>61,70</sup> By measuring the three quantities noted above in nitrogen/argon plasma flows, and making use of a pitot pressure measurement and facility data, it is possible to calculate the stream total enthalpy and to quantify the different contributions: thermal, kinetic, and chemical. This is extremely useful for establishing stream conditions, extrapolating the free-stream test conditions to a flight environment, and provides experimental data against which a CFD computation of gas flow through the arc-jet nozzle and towards the test article can be tested. However, arc-jet free-stream measurements still only provide a different starting point for the eventual assessment of the boundary layer conditions above a test article.

The arc-jet free-stream measurements indicate low translational temperatures, high velocity and non-equilibrium atom number densities.<sup>58,59</sup> In contrast, the boundary layer edge measurement from the ICP facility discussed above (Fig. 9) indicates high translational temperature and low velocity. It is reasonable to expect that within the boundary layer in an arc-jet test, LIF measurements would be quite different from those of the free-stream, and more likely, similar to those of the ICP facility boundary layer edge.

For material test applications temperature and species information from the reacting boundary layer is extremely important. While LIF measurements in the boundary layer are relatively rare, recent experiments indicate their feasibility.<sup>60,70</sup> Two strategies exist for measuring species and temperature profiles above the surface. The first is a point-wise approach that involves translating the laser probe volume toward the surface, as indicated in Fig. 10, and the other is a planar approach that requires sufficient laser pulse energy to spread the beam into a light sheet. In the latter, an intensified camera is needed to record the fluorescence signals, which complicates the interpretation of the measured signals.

Fig. 11 shows computed boundary layer profiles of temperature, and total and species number densities, for an air plasma

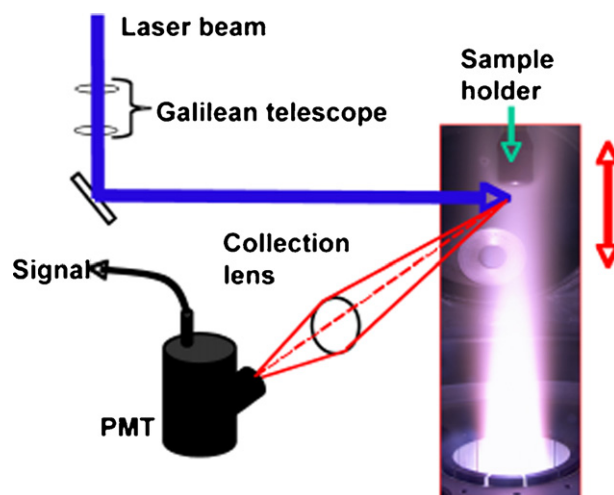


Fig. 10. Translation of either the test article or the beam delivery and collection optics to measure the species number densities and temperature in the boundary layer approaching the test article in the stagnation region.

along the stagnation streamline for a particular high-enthalpy test condition.<sup>17</sup> The catalytic efficiency of the surface was set to a relatively low  $10^{-4}$  for these computations. Temperature and number densities are normalized by their boundary layer edge values. Different information is available from different species measurements. All species number densities increase with approach to the surface because of the decreasing gas temperature in a constant pressure boundary layer. The relative O-atom number density and total mixture number density curves overlay each other in Fig. 11, indicating that for these

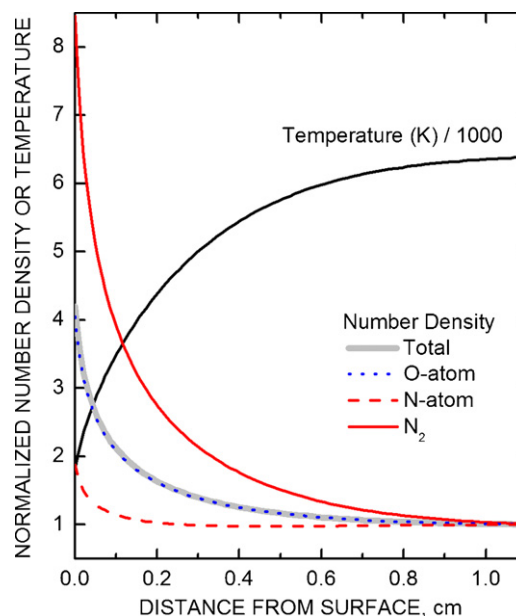


Fig. 11. Computed temperature, mixture density, and species number density variations along the stagnation streamline for the flow over a low-catalycity sample in the VKI Plasmatron ICP Torch Facility. The number densities are normalized by their free-stream (boundary layer edge) values. Note that the total and O-atom number density curves overlay one another, indicating that for these boundary layer conditions there is little gas-phase recombination of O to  $O_2$ .

plasma conditions, relatively little gas-phase recombination of O to O<sub>2</sub> occurs. The N-atom number density increases more slowly and the N<sub>2</sub> number density more rapidly than the total number density, indicating that gas-phase recombination of N to N<sub>2</sub> is important at these conditions.

Whether probing N or O, if a simultaneous measurement of the atom number density and translational temperature can be obtained (as described above) as a function of distance from the sample surface, the total number density can then be computed from a pressure measurement and the translational temperature using the ideal gas equation of state  $n = P/k_B T$ . This, along with the measured atom number density, gives the mole fraction of the probed atomic species. For a pure nitrogen plasma this can completely characterize the local thermodynamic conditions, as long as ionization is not significant, since the N<sub>2</sub> number density can be found from  $n_{N_2} = n - n_N$ . For an air plasma, measurements of both O-atom and N-atom number densities are needed for a complete understanding of the local thermodynamic state.

The relative species density profiles presented in Fig. 11 show trends characteristic of a low catalytic, non-reacting surface, wherein the relative number densities increase towards the wall as determined by the gas temperature profile and gas-phase recombination reactions. For a highly catalytic surface the atomic species number densities should trend downward approaching the surface to very small levels. Reported species density uncertainties<sup>60,70</sup> suggest that measurement of gradients with density changes of two to four are realizable, especially when relative LIF signals are used to measure the trend of a normalized species density.

The monitoring of volatile products during high-enthalpy UHTC testing by LIF is also possible, although such work has not yet been reported. Both B atoms<sup>71</sup> and BO molecules<sup>72,73</sup> have been detected by LIF schemes, as have Si atoms<sup>74,75</sup> and SiO molecules.<sup>74,76</sup> Feigl and Auweter-Kurtz<sup>77</sup> have used LIF to monitor SiO concentrations in front of SiC materials oxidized in argon–oxygen–nitrogen plasma flows, by exciting the SiO ( $A^1\Pi \leftarrow X^1\Sigma^+(0, 0)$ ) transition near 234 nm and collecting fluorescence near 260 nm from the ( $A^1\Pi \rightarrow X^1\Sigma^+(0, 3)$ ) band. They associate rapid rises of SiO in the gas-phase with the transition between passive and active SiC oxidation (i.e., between reactions (4) and (5)). Beyond the simple detection of volatile species, spatially resolved LIF of volatiles in the boundary layer would enable the measurement of species gradients that could in principle be related to volatilization rates from the surface. No measurements of this type have yet been attempted and their interpretation would require additional gas-phase chemistry inputs to existing CFD programs.

#### 4.4. Other techniques

##### 4.4.1. Fourier transform infrared spectroscopy

Fourier Transform Infrared (FTIR) spectroscopy is a technique used to capture and spectrally resolve infrared radiation using a scanning interferometer, typically at wavelengths between 1 and 40  $\mu\text{m}$ . Transmission FTIR spectroscopy is often used as a laboratory technique to identify chemical species in gas or liquid samples, by absorption features that occur at char-

acteristic energies (wavelengths) related to particular vibrational modes of different chemical bonds. These characteristic absorption features are relatively sharp in the gas-phase, and often broaden and shift slightly in the liquid phase. A similar technique is used to detect molecules on surfaces by reflection FTIR and can be used to monitor thin film growth.

Estimates of the temperature-dependant total, hemispherical emittance are often derived from spectrally resolved, hemispherical reflectance measurements performed at room temperature using FTIR instruments fit with integrating spheres.<sup>17</sup> The measured spectral reflectance,  $\rho_{298}(\lambda)$ , is converted to spectral absorbance,  $\alpha_{298}(\lambda)$ , using the relation  $\alpha_{298}(\lambda) = 1 - \rho_{298}(\lambda)$  valid for an opaque surface, and the spectral absorbance is equated to the spectral emittance based on Kirchhoff's law,  $\varepsilon_{298}(\lambda) = \alpha_{298}(\lambda)$ . Total hemispherical emittance at any temperature is then computed by averaging the room-temperature emittance over the Planck blackbody radiation function:

$$\varepsilon(T) \cong \frac{\int_{\lambda_1}^{\lambda_2} \varepsilon_{298}(\lambda) E_b(\lambda, T) d\lambda}{\int_{\lambda_1}^{\lambda_2} E_b(\lambda, T) d\lambda}. \quad (13)$$

This process assumes that the temperature dependence of total emittance is dominated by the temperature dependence of the Planck function and not by the optical constants of the material. It also presumes that the spectral range of the measurement,  $\lambda_1$  to  $\lambda_2$ , is sufficiently broad that it contains the spectral region dominating the emissive power at each temperature.

A variant of this technique – emission FTIR – was recently used in a laboratory setting to capture thermal emission from C/ZrB<sub>2</sub>–SiC composites over the 200–800 °C temperature range and an effective temperature-dependant emittance was computed.<sup>78</sup> However, the spectral range of the FTIR instrument used in this work was only 8–14  $\mu\text{m}$  and this limited range contains just ~40% of the radiative power emitted at 200 °C and less than 10% of the emitted power at 800 °C. The derived emittance values are thus tenuous approximations for the total emittance.

Marshall et al.<sup>17</sup> have shown how a broad feature in the FTIR reflectance spectra of virgin ZrB<sub>2</sub>–30SiC in the 10–13- $\mu\text{m}$  range was removed and replaced by a sharper feature centered near 9  $\mu\text{m}$  after oxidation. The former feature can be related to stretching mode vibrations of Si–C bonds and the latter to stretching mode vibrations of Si–O bonds. A similar enhanced reflectance feature predicted for ZrO<sub>2</sub> near 14  $\mu\text{m}$  was not observed in oxidized samples, consistent with the fact that the outer scale was dominated by silica rich glass.

Related spectral features should appear as emittance modifications to the Planck blackbody radiation function in thermal emission. This suggests that FTIR emission spectroscopy might be used as an *in situ* monitor for changing surface compositions during high-enthalpy testing. Measurements of this type were made by Hirsch et al.<sup>52</sup> for characterizing the oxidation behavior of carbon/carbon and carbon/silicon carbide composites in the ICP wind tunnels. However, this concept has never been explored as an *in situ* diagnostic for UHTC materials systems.

Even without reference to a blackbody standard, the broad mid-IR spectral features associated with SiO<sub>2</sub>, SiC, ZrO<sub>2</sub> and

HfO<sub>2</sub> are sufficiently separated that difference spectra should track shifts in the dominant surface composition with time. This approach has the potential to monitor important thermodynamic and chemical transitions as test conditions are varied or as constituents are depleted over time. For example, changes in the relative strengths of the SiO<sub>2</sub> and SiC spectral features could be used to track the important transition from passive SiC oxidation with the formation of condensed silica to active SiC oxidation with the formation of volatile SiO. The identification of temperature and pressure thresholds at which the loss of SiO<sub>2</sub> from the oxide scale becomes large – be it by active oxidation, evaporation, or melt flow – is critical to UHTC performance and should be evidenced by the appearance of the ZrO<sub>2</sub> or HfO<sub>2</sub> features above 14 μm.

#### 4.4.2. Absorption spectroscopy

The spatial resolution advantage of the LIF technique has been contrasted above with path-integrated emission measurements, which can also clearly provide useful information for material test applications. Similarly, absorption measurements can provide useful information since they typically probe either ground or low-lying electronic states even though this information is also path-integrated. One such application is the measurement of molecular species formed by gas/surface interactions.

Advances in semiconductor processing have enabled rapid development of Tunable Diode Laser Absorption Spectroscopy (TDLAS). Relatively inexpensive, but tunable, diode lasers operating with narrow line widths can be optimized for overlap with favorable rotational–vibrational transition features of important molecular species that have dipole moments, such as NO, CO<sub>2</sub>, CO, H<sub>2</sub>O, SiO, and BO. Access to ground electronic state population information is often available by probing rotational–vibrational transitions in the 1–5-μm wavelength region. Neither O<sub>2</sub> nor N<sub>2</sub> have dipole moments, and so are not considered candidate species for this approach; however, in the case of O<sub>2</sub>, it is possible to probe the ground state by absorption via the A electronic band transition ( $b^1\Sigma_g^+ \leftarrow X^3\Sigma_g^-$ ) near 760 nm. This approach has been used to characterize shock tube flows,<sup>79</sup> but has not yet been applied to either arc-jet or ICP facility measurements.

Recently, the TDLAS technique was used to probe CO in a Mars atmosphere study in an arc-jet facility, where path-integrated values of translation temperature, velocity, and CO concentration were obtained.<sup>80</sup> To date however, the application of TDLAS in the boundary layer near a catalytic or reacting material surface in a plasma facility to quantify recombined or reaction-produced molecules has not been reported.

#### 4.4.3. Raman spectroscopy

Raman scattering, like LIF, is an inelastic scattering process, but involves excitation to a virtual upper energy level. In Raman spectroscopy, a laser beam illuminates the gas mixture and Raman scattered photons are detected at wavelengths offset from the illumination wavelength by increments determined by the vibrational and rotational energy spacing of molecules in gas. By choosing an appropriate laser wavelength (typically

in the ultraviolet since Raman cross sections scale as frequency to the fourth power), and using a high-resolution spectral filter (often a spectrometer), scattered signals from molecules in a gas mixture can be recorded and analyzed for species concentration and temperature. Details of this common spectroscopic technique can be found in Eckbreth.<sup>56</sup>

An attractive attribute of Raman scattering is that, as in the case of LIF, it provides spatially resolved information, and so can be used to map temperature and species gradients. In addition, each molecular species present scatters at its characteristic Raman wavelengths, so a single laser frequency can access multiple species, depending on the strength of their Raman cross sections. Since all molecules are Raman-active, this technique can detect important species involved in UHTC oxidation and volatilization processes, like SiO, SiO<sub>2</sub>, BO, BO<sub>2</sub>, CO, and CO<sub>2</sub>.

While applications to plasma flows in arc-jet and ICP facilities are relatively sparse, one recent investigation has demonstrated the potential of this technique in the area of recombined molecular species quantification.<sup>81</sup> In this investigation a frequency tripled Nd:YAG laser operating at 355 nm was used to probe the boundary layer of an air plasma flowing over a flat stainless steel plate in an ICP facility. Despite the relatively weak Raman cross sections ( $\sim 10^{-31}$  cm<sup>2</sup> sr<sup>-1</sup>) profiles of N<sub>2</sub> and O<sub>2</sub> number density, rotational temperature, and vibrational temperature were obtained in the boundary layer flow. Long steady test times were needed to achieve usable signal-to-noise levels, but the results are promising for future applications.

## 5. Summary

Arc-jet and ICP plasma tunnels remain the primary facilities used to ground test the performance of UHTC TPS materials and components for hypersonic flight. We have highlighted the main features of the test conditions obtained in these two types of facilities and discussed their similarities and differences. Various *in situ* optical diagnostics, both established and under development, were described, that can provide information to document test conditions, monitor the evolution of test articles, and provide data that can be used to strengthen the accuracy of CFD models. The importance of CFD modeling of the arc-jet and ICP test environments, and in particular the computation of species concentrations at specimen surfaces, is emphasized as essential for materials science interpretations of UHTC test results. The increasing integration of CFD modeling and *in situ* optical diagnostics in plasma tunnel testing is sure to enhance the understanding and optimization of UHTC material performance in aerothermal environments.

## Acknowledgements

This work was supported by the High-Temperature Aerospace Materials Program of the Air Force Office of Scientific Research through contracts FA9550-08-C-0049 (J. Marschall) and FA9550-08-1-0414 (D. Fletcher). We acknowledge Jan Thömel for the CFD results presented in Sections 3

and 4.3, and Mickaël Playez for the emission measurements highlighted in Section 4.2.

## References

- Fuller J, Blum Y, Marschall J. Topical issue on ultra-high-temperature ceramics. *J Am Ceram Soc* 2008;**91**:1397–502.
- Fuller J, Sacks M. Special section: ultra-high temperature ceramics. *J Mater Sci* 2004;**39**:5885–6066.
- Kaufman L. Boride composites—a new generation of nose cap and leading edge materials for reusable lifting re-entry systems. In: *AIAA advanced space transportation meeting*, AIAA Paper 70-278. February 1970.
- Bull J, Kolodziej P, Salute J, Keese D. Design, instrumentation and pre-flight testing of a sharp ultra-high temperature ceramic nosetip. NASA TM-1998-112229; October 1998.
- Kolodziej P, Bull J, Salute J, Keese DL. First flight demonstration of a sharp ultra-high temperature ceramic nosetip. NASA TM-112215; December 1997.
- Kinney DJ, Bowles JV, Yang LH, Roberts CD. Conceptual design of a “SHARP”-CTV. In: *35th AIAA thermophysics conference*, AIAA Paper 2001-2887. June 2001.
- Reuther J, Kinney D, Smith S, Kontinos D, Gage P, Saunders D. A reusable space vehicle design study exploring sharp leading edges. In: *35th AIAA thermophysics conference*, AIAA Paper 2001-2884. June 2001.
- Metcalfe AG, Elsner NB, Allen DT, Wuchina E, Opeka M, Opila E. Oxidation of hafnium diboride. *Electrochem Soc Proc* 1999;**99**:38:489–501.
- Wuchina EJ, Opeka MM. Oxidation of Hf-based ceramics. *Electrochem Soc Proc* 1999;**99**:38:477–88.
- Opila E, Levine S, Lorincz J. Oxidation of ZrB<sub>2</sub>- and HfB<sub>2</sub>-based ultra-high temperature ceramics: effect of Ta additions. *J Mater Sci* 2004;**39**:5969–77.
- Gasch M, Ellerby D, Irby E, Beckman S, Gusman M, Johnson S. Processing, properties, and arc jet oxidation of hafnium diboride/silicon carbide ultra high temperature ceramics. *J Mater Sci* 2004;**39**:5925–37.
- Chamberlain A, Fahrenholtz W, Hilmas G, Ellerby D. Oxidation of ZrB<sub>2</sub>-SiC ceramics under atmospheric and reentry conditions. *Refract Appl Trans* 2005;**1**:2–8.
- Savino R, De Stefano Fumo M, Silvestroni L, Sciti D. Arc-jet testing on HfB<sub>2</sub> and HfC-based ultra-high temperature ceramic materials. *J Eur Ceram Soc* 2008;**28**:1899–907.
- Monteverde F, Savino R. Stability of ultra-high temperature ZrB<sub>2</sub>-SiC ceramics under simulated atmospheric re-entry conditions. *J Eur Ceram Soc* 2007;**27**:4797–805.
- Zhang X, Hu P, Han J, Meng S. Ablation behavior of ZrB<sub>2</sub>-SiC ultra high temperature ceramics under simulated atmospheric re-entry conditions. *Compos Sci Technol* 2008;**68**:1718–26.
- Ito T, Kurotaki T, Sumi T, Fujita K, Ishida K, Mizuno M. Evaluation of surface catalytic effect on TPS in 110 kW ICP-heated wind tunnel. In: *43rd AIAA aerospace sciences meeting and exhibit*, AIAA Paper 2005-189. January 2005.
- Marschall J, Pejaković DA, Fahrenholtz WG, Hilmas GE, Zhu S, Ridge J, Fletcher DG, Asma CO, Thömel J. Oxidation of ZrB<sub>2</sub>-SiC ultra-high temperature ceramic composites in dissociated air. *J Thermo Heat Trans* 2009;**23**:267–78.
- Playez M, Fletcher DG, Marschall J, Fahrenholtz WG, Hilmas GE, Zhu S. Optical emission spectroscopy during plasmatron testing of ZrB<sub>2</sub>-SiC ultra-high temperature ceramic composites. *J Thermo Heat Trans* 2009;**23**:279–85.
- Smith RK, Wagner DA, Cunningham J. A survey of current and future plasma arc-heated test facilities for aerospace and commercial applications. In: *36th AIAA aerospace sciences meeting and exhibit*, AIAA Paper 1998-0146. January 1998.
- Ragsdale R, Lanzo C, Randall D, Thorpe M. Reentry heating experiments using an induction heated plasma. NASA TM X-1978, Cleveland, OH; March 1970.
- Bose D, Skokova K, Wright MJ, Reuther J. Ground-to-flight traceability analysis of arcjet testing for the crew exploration vehicle. In: *41st AIAA thermophysics conference*, AIAA Paper 2009-3845. June 2009.
- Kolesnikov AF. The concept of local simulation for stagnation point heat transfer in hypersonic flows: applications and validation. In: *21st AIAA aerodynamic measurement technology and ground testing conference*, AIAA Paper 2000-2515. June 2000.
- Gökçen T. Effects of flowfield nonequilibrium on convective heat transfer to a blunt body. In: *34th Aerospace sciences meeting and exhibit*, AIAA Paper 96-0352. January 1996.
- Barbante PF, Chazot O. Flight extrapolation of plasma wind tunnel stagnation region flowfield. *J Thermo Heat Trans* 2006;**20**:493–9.
- Parthasarathy TA, Rapp RA, Opeka M, Kearns RJ. A model for the oxidation of ZrB<sub>2</sub>, HfB<sub>2</sub>, and TiB<sub>2</sub>. *Acta Mater* 2007;**55**:5999–6010.
- Rezaie A, Fahrenholtz WG, Hilmas GE. Evolution of structure during the oxidation of zirconium diboride-silicon carbide in air up to 1500 °C. *J Eur Ceram Soc* 2007;**27**:2495–501.
- Fahrenholtz WG. Thermodynamic analysis of ZrB<sub>2</sub>-SiC oxidation: formation of a SiC-depleted region. *J Am Ceram Soc* 2007;**90**:143–8.
- Li J, Lenosky TJ, Först CJ, Yip S. Thermochemical and mechanical stabilities of the oxide scale of ZrB<sub>2</sub> + SiC and oxygen transport mechanisms. *J Am Ceram Soc* 2008;**91**:1475–80.
- Fletcher DG, Playez M. Characterization of supersonic and subsonic plasma flows. In: *25th AIAA aerodynamic measurement technology and ground test conference*, AIAA Paper 2006-3294. June 2006.
- Barbante PF, Degrez G, Sarma GSR. Computation of nonequilibrium high-temperature axisymmetric boundary-layer flows. *J Thermo Heat Trans* 2002;**16**:490–7.
- Magin T, Vanden Abeele DP, Degrez G. An implicit multiblock solver for inductive plasma flows. In: *Fluids 2000*, AIAA Paper 2000-2480. June 2000.
- Vanden Abeele DP, Degrez G. Numerical model of high-pressure air inductive plasma under thermal and chemical non-equilibrium. In: *31st AIAA plasmadynamics and laser conference*, AIAA Paper 2000-2416. June 2000.
- Bottin B, Vanden Abeele DP, Carbonaro M, Degrez G, Sarma GSR. Thermodynamic and transport properties for inductive plasma modeling. *J Thermo Heat Trans* 1999;**13**:343–50.
- Wright MJ, Candler GV, Bose D. Data-parallel line relaxation method for the Navier–Stokes equations. *AIAA J* 1998;**36**:1603–9.
- Gökçen T, Chen Y-K, Skokova KA, Milos FS. Computational analysis of arc-jet stagnation tests including ablation and shape change. In: *41st AIAA thermophysics conference*, AIAA Paper 2009-3596. June 2009.
- Gökçen T, Skokova K, Balboni JA, Terrazas-Salinas I, Bose D. Computational analysis of arc-jet wedge calibration tests in IHF 6-inch conical nozzle. In: *47th AIAA aerospace sciences meeting*, AIAA Paper 2009-1348. January 2009.
- Gökçen T, Stewart DA. Computational analysis of semi-elliptical nozzle arc-jet experiments: calibration plate and wing leading edge. In: *35th AIAA fluid dynamics conference and exhibit*, AIAA Paper 2005-4887. June 2005.
- Gordon S, McBride BJ. Computer program for calculation of complex chemical equilibrium compositions and applications I. Analysis. NASA RP-1311, Cleveland, OH; October 1994.
- Ramshaw JD. Self-consistent effective binary diffusion in multicomponent gas mixtures. *J Non-Equilib Thermodyn* 1990;**15**:295–300.
- Gupta R, Yos J, Thompson R, Lee K. A review of reaction rates and thermodynamic and transport properties for an 11-species air model for chemical and thermal nonequilibrium calculations to 30000 K. NASA RP-1232; August 1990.
- Wright MJ, Bose D, Palmer GE, Levine E. Recommended collision integrals for transport property computations. Part 1. Air species. *AIAA J* 2005;**43**:2558–64.
- Wright MJ, Hwang HH, Schwenke DW. Recommended collision integrals for transport property computations. Part 2. Mars and Venus entries. *AIAA J* 2007;**45**:281–8.
- Scatteia L, Borrelli R, Cosentino G, Bêche E, Sans J-L, Balat-Pichelin M. Catalytic and radiative behaviors of ZrB<sub>2</sub>-SiC ultrahigh temperature ceramic composites. *J Spacecraft Rock* 2006;**43**:1004–12.
- Scatteia L, Alfano D, Monteverde F, Sans J-L, Balat-Pichelin M. Effect of machining method on the catalytic and emissivity of ZrB<sub>2</sub> and ZrB<sub>2</sub>-HfB<sub>2</sub>-based ceramics. *J Am Ceram Soc* 2008.

45. Park C, Moore D. A polynomial method for determining local emission intensity by Abel inversion. NASA TN D-5677; February 1970.
46. Spalding MJ, Krier H, Burton RL. Boron suboxides measured during ignition and combustion of boron in shocked Ar/F/O<sub>2</sub> and Ar/N<sub>2</sub>/O<sub>2</sub> mixtures. *Comb Flame* 2000;**120**:200–10.
47. Ralchenko Y, Kramida AE, Reader J. NIST atomic spectra database (Version 3.1.5). National Institute of Standards and Technology. <http://physics.nist.gov/asd3>; 2008.
48. Monteverde F, Bellosi A. Oxidation of ZrB<sub>2</sub>-based ceramics in dry air. *J Electrochem Soc* 2003;**150**:B552–9.
49. Monteverde F, Bellosi A. The resistance to oxidation of an HfB<sub>2</sub>–SiC composite. *J Eur Ceram Soc* 2005;**25**:1025–31.
50. Rizzo HF. Oxidation of boron at temperatures between 400 and 1300 °C in air. In: Kohn JA, Nye WF, editors. *Boron—synthesis, structure, and properties*. New York: Plenum Press; 1968. p. 175–89.
51. Roine A. *HSC chemistry for windows, version 5.11*. Pori, Finland: Outokumpu Research Oy; 2006.
52. Hirsch K, Roth B, Altmann I, Barth K-L, Jentschke H, Lunk A, Schumacher U. Plasma-induced silica-like protection layer formation on C/C–SiC heat-shield materials for re-entry vehicles. *High Temp–High Press* 1999;**31**:455–65.
53. Altmann I, Bauer G, Hirsch K, Jentschke H, Klengel S, Roth B, Schinköth D, Schumacher U. In-situ diagnostics of the interaction region between a nitrogen–oxygen plasma jet and hot C/C–SiC ceramic materials. *High Temp–High Press* 2000;**32**:573–9.
54. Jentschke H, Hirsch K, Klengel S, Schumacher U. High resolution emission and absorption spectroscopy for erosion product analysis in boundary plasmas. *Rev Sci Instrum* 1999;**70**:336–9.
55. Herdrich G, Fertig M, Löhle S, Pidan S, Augweter-Kurtz M. Oxidation behavior of siliconcarbide-based materials by using new probe techniques. *J Spacecraft Rock* 2005;**42**:817–24.
56. Eckbreth AC. *Laser diagnostics for combustion temperature and species*. Cambridge: Abacus Press; 1988.
57. Crosley DR, Jeffries JB, Smith GP. Absolute concentration measurements of chemically-important flame radicals. *Isr J Chem* 1999;**39**:41–8.
58. Fletcher D. Arc-jet flow properties determined from laser-induced fluorescence of atomic nitrogen. *Appl Opt* 1999;**38**:1850–8.
59. Fletcher DG, Bamford DJ. Arcjet flow characterization using laser-induced fluorescence of atomic species. In: *7th AIAA/ASME joint thermophysics and heat transfer conference*, AIAA Paper 98-2458. June 1998.
60. Löhle S, Auweter-Kurtz M, Herdrich G, Laux T. Measurements of NO in N<sub>2</sub>/O<sub>2</sub> and N<sub>2</sub>/CO<sub>2</sub> plasma flows. In: *36th AIAA thermophysics conference*, AIAA Paper 2003-3487. June 2003.
61. Grinstead J, Driver D, Raiche G. Radial profiles of arc-jet flow properties measured with laser-induced fluorescence of atomic nitrogen. In: *41st Aerospace sciences meeting and exhibit*, AIAA Paper 2003-0400. January 2003.
62. Laux T, Feigl M, Stöckle T, Auweter-Kurtz M. Estimation of the surface catalyticity of PVD-coatings by simultaneous heat flux and LIF measurements in high enthalpy air flows. In: *34th AIAA thermophysics conference*, AIAA Paper 2000-2364. June 2000.
63. Bamford DG, Dyer MJ, Bischel WK. Single-frequency laser measurements of two-photon cross sections and Doppler-free spectra for atomic oxygen. *Phys Rev A* 1987;**36**:3497–500.
64. Bamford DJ, Bischel WK, Hickman AP, Dyer MJ. *Proceedings of the society of photo-optical instrumentation engineers*; vol. 912. 1988. p. 139–44.
65. Bamford DJ, Jusinski LE, Bischel WK. Absolute two-photon absorption and three-photon ionization cross sections for atomic oxygen. *Phys Rev A* 1986;**34**:185–98.
66. Fletcher DG. Arcjet flow properties determined from laser-induced fluorescence of atomic nitrogen. In: *36th Aerospace sciences meeting and exhibit*, AIAA Paper 98-0205. January 1998.
67. Goehlich A, Kawetzki T, Döbele HF. On absolute calibration with xenon of laser diagnostic methods based on two-photon absorption. *J Chem Phys* 1998;**108**:9362–70.
68. Niemi K, Gathen VS-vd, Döbele HF. Absolute atomic oxygen density measurements by two-photon absorption laser-induced fluorescence spectroscopy in an RF-excited atmospheric pressure plasma jet. *Plasma Sour Sci Technol* 2005;**14**:375–86.
69. Niemi K, Gathen VS-vd, Döbele HF. Absolute calibration of atomic density measurements by laser-induced fluorescence spectroscopy with two-photon excitation. *J Phys D Appl Phys* 2001;**34**:2330–5.
70. Koch U, Gülhan A, Esser B. Two dimensional spatially resolved two photon oxygen atom laser induced fluorescence measurements in the flow field of the arc heated facility L3K. In: Danesy D, editor. *Proceedings of the fifth European symposium on aerothermodynamics for space vehicles (SP-563)*. Noordwijk, The Netherlands: European Space Agency; 2005. p. 493.
71. Canosa A, Le Picard SD, Geppert WD. Experimental kinetics study of the reaction of boron atoms, B(<sup>2</sup>P<sub>1</sub>), with ethylene at very low temperatures (23–295 K). *J Phys Chem A* 2004;**108**:6183–5.
72. Stanton CT, Garland NL, Nelson HH. Temperature dependence of the kinetics of the reaction BO + O<sub>2</sub>. *J Phys Chem* 1991;**95**:8741–4.
73. Hinchin JJ. Kinetics for quenching and relaxation of boron oxide. *J Chem Phys* 1993;**99**:4403–10.
74. Takahara A, Tezaki A, Matsui H. Production of SiO and Si(<sup>3</sup>P) in the reaction of silane with O(<sup>1</sup>D). *J Phys Chem A* 1999;**103**:11315–20.
75. Okano A, Takayanagi K. Laser-induced fluorescence from collisionally excited Si atoms in laser ablation plume. *J Appl Phys* 1999;**86**:3964–72.
76. Walkup RE, Raider SI. *In situ* measurements of SiO(g) production during dry oxidation of crystalline silicon. *Appl Phys Lett* 1988;**53**:888–90.
77. Feigl M, Auweter-Kurtz M. Investigation of SiO production in front of Si-based material surfaces to determine the transition from passive to active oxidation using planar laser-induced fluorescence. 35th AIAA Thermophysics Conference, AIAA Paper 2001-3022.
78. Tang S, Deng J, Wang S, Liu W. Comparison of thermal and ablation behavior of C/SiC composites and C/ZrB<sub>2</sub>–SiC composites. *Corros Sci* 2009;**51**:54–61.
79. Philippe L, Hanson R. Tunable diode laser absorption sensor for temperature and velocity measurement of O<sub>2</sub> in air flows. In: *29th AIAA aerospace sciences meeting and exhibit*, AIAA Paper 91-0360. January 1991.
80. Koch U, Riehmer J, Esser B, Gülhan A. Laser induced fluorescence and diode laser absorption spectroscopy measurements in CO/CO<sub>2</sub> hypersonic flow of LBK. In: Lacoste H, Ouwehand L, editors. *Proceedings of the sixth European symposium on aerothermodynamics for space vehicles (SP-659)*. Noordwijk, The Netherlands: European Space Agency; 2009.
81. Studer D, Vervisch P. Raman scattering measurements within a flat plate boundary layer in an inductively coupled plasma wind tunnel. *J Appl Phys* 2007;**102**, 03303-1-8.

## Realization of a Gas-Surface Interaction Test Case for Model Validation

D. G. Fletcher <sup>†</sup>	J. Thömel <sup>‡</sup> & O. Chazot <sup>‡*</sup>	J. Marschall <sup>*</sup>
U. Vermont	von Karman Institute	SRI International
Burlington, VT	Rhode-St-Genese, Belgium	Menlo Park, CA

**Abstract:** This paper describes a numerical investigation of a surface exposed to a plasma flow for different plasma and material boundary conditions to allow an assessment of laser diagnostic measurements in the boundary layer. The eventual goal is to develop a test case to validate physical and chemical models underlying current gas-surface interaction simulations. Using an existing numerical model, boundary layer gradients of temperature and key species are predicted for different boundary layer edge and surface conditions in an inductively coupled plasma facility. These predictions are then used to assess which species can be measured quantitatively with sufficient accuracy for model validation purposes.

### I. Introduction

One of the critical issues in the development of economical yet robust atmospheric entry vehicles is the accurate modeling of aero-thermal heating of the vehicle thermal protection system (TPS). This issue has also been identified as a risk driver for the development of a new manned exploration vehicle [1] as well as an enabling technology for better-equipped unmanned exploration of the solar system. While understanding the physical and chemical processes that determine the surface heat flux has been an active pursuit of the aero-thermal research community for many years, investigations that couple accurate modeling of convective and radiative heating with the material response remain at an empirically limited level.

As part of an international effort to improve this situation, a dedicated session of the 6<sup>th</sup> European Aerothermodynamics Symposium was held to establish the state of the art in this field for one of the many critical gas-surface interaction phenomena: surface catalysis. Different research groups participating in this session were asked to document their method for determining surface catalycity for candidate thermal protection materials tested in plasma facilities. This activity was expected to establish a reference point for further activities directed toward validation of the physical and chemical models that comprise the methods. All of the approaches for determining surface catalycity values that could be used to model material boundary conditions in flight relied largely on computational simulations of the test environment that included conservative and possibly limiting assumptions.

---

<sup>†</sup> Professor, Associate Fellow AIAA.

<sup>‡</sup> PhD Candidate, Member AIAA.

<sup>‡\*</sup> Associate Professor, Member AIAA.

<sup>\*</sup> Senior Research Scientist, Senior Member, AIAA.

Copyright © 2009 by the University of Vermont. Published by the American Institute of Aeronautics and Astronautics, Inc. with permission.

In this paper, we present an analysis of stagnation-point testing that may lead to a useful experimental test case for validation of the underlying physical and chemical models that are used to interpret heat flux measurements in plasma facilities. As these same models are used in codes that estimate aero-thermal heating for entry and re-entry trajectories, interest in such a test case extends beyond plasma testing. By validation we mean a data set that allows an assessment of the surface-driven and gas-phase chemical reaction rates, physical transport properties and fluid dynamics of a reacting boundary layer above a well-known material exposed to high-temperature, or plasma gas flow. Since gas-surface interactions depend directly on the material exposed to the plasma, this first analysis cannot address all interactions. Instead, we have chosen to consider a stable surface material (non-eroding) with a relatively low surface temperature, such as a metallic material, to illustrate the approach. Subsequent efforts may involve more interesting materials that could offer a wider range of complex, and likely coupled, gas-surface interactions, such as oxidation, nitridation, erosion, sublimation, pyrolysis, or ablation.

The work described in the following sections begins with a discussion of stagnation point heating as the basis for the choice of test conditions for this study. The discussion includes consideration of trajectory conditions, available diagnostic techniques, and test facility considerations. Following this discussion, predictions of species density and temperature gradients in the reacting boundary layer above the material surface are presented, with a description of the limiting assumptions used for these predictions. Key parameters are varied to establish which variables should be quantified to provide the most information about the state of the boundary layer. This is followed by an analysis of which diagnostic techniques can be used to accurately measure target species and thermodynamic property gradients, along with estimations of likely measurement signal levels. All of these precedent sections lead to a recommendation of a candidate test case for validating gas-surface interaction models.

## **II. Stagnation Point Heating and Plasma Testing**

Since stagnation point heating rates are the highest on any atmospheric entry, or re-entry, vehicle, all plasma ground-test facilities have stagnation point testing capability. Thus, our analysis considers only the stagnation test configuration. Two different types of plasma facility have been developed for testing thermal protection materials, and both are designed to replicate the local trajectory-heating rate for a wide range of trajectories and for different test gas mixtures. Tests of TPS materials are done to evaluate material performance at peak heating and total heat load conditions. Arc-jet facilities are the most common plasma test facilities in the US, with large-scale installations at NASA, AEDC, and Boeing [2]. These plasma tunnels use a constricted-arc heater to operate at the high-reservoir conditions needed to produce supersonic plasma streams that provide post-shock stagnation conditions that match trajectory conditions. While arc-jet facilities exist in Europe and Russia, inductively coupled plasma (ICP) facilities are also used to simulate trajectory-heating conditions for stagnation-point testing [3]. Owing to the inductor designs, ICP facilities are typically operated in the subsonic flow regime, and thus provide a shock free subsonic plasma flow over the test article. Duplication of the

flight post-shock stagnation pressure is achieved by controlling the static pressure in the test chamber.

Arc-jets and ICP facilities each have advantages and disadvantages. Clearly, the arc-jets provide a closer, but still not exact, match of the flight fluid dynamic conditions, but the energy deposition is based on a direct arc discharge that must attach to specially designed electrodes. Arc attachment in these devices results in avoidable entrainment of electrode material, typically copper, in the plasma stream as a contaminant. As yet there is no proof that copper in the plasma stream has a significant impact on the interpretation of material test results. In contrast, the ICP facilities use inductive coupling at radio frequency to energize the plasma, and there are no electrodes present in the flow path. This not only ensures contaminant-free operation, but also allows operation on a wide range of test gas mixtures. Another important difference between these facilities exists in the flow processes leading to the boundary layer edge conditions over a test sample. In the case of supersonic arc-jet operation, the rapid acceleration through a converging-diverging nozzle can lead to nonequilibrium or frozen conditions ahead of the detached shock at the test article. From these conditions, the plasma is compressed flowing through the shock, and then relaxation processes drive the plasma toward equilibrium at the boundary layer edge. For a subsonic ICP flow the plasma leaves the induction zone and flows toward the sample with a velocity less than 100 m/s along a roughly 150 cm length at nearly constant pressure. As with the post-shock arc-jet flow, relaxation processes drive the plasma toward equilibrium as it flows toward the boundary layer edge. Note that, to date, there have been no measurements that establish whether or not thermo-chemical equilibrium is actually reached at the boundary layer limit.

For both facility types TPS material test conditions are established by a combination of heat flux (usually with a fully catalytic, cold-wall probe), pitot pressure, and surface temperature measurements. As long as the heat-flux probe has the same geometry as the probe holding the test sample, the test conditions at the boundary layer edge above the sample are expected to be the same as those above the cold-wall calorimeter (discussed further below). While these probe measurements alone may be able to characterize the aero-thermal heating conditions, they are not at all sufficient to establish the free stream plasma conditions in either facility. In both cases, unless there are additional measurements, modeling is required to extract free stream conditions [3-6]. This modeling is based on physical and chemical models that have been developed for aerothermal heating analysis, along with some assumptions about either initial conditions or the thermochemical state of the plasma at a certain location. Continued reliance on modeling to determine the boundary layer edge conditions presents a challenge for detailed investigations of gas-surface interactions, since any investigation must be able to establish edge conditions as a starting point.

In a previous paper heat flux measurements from a standard model tested in both arc-jet and ICP facilities were shown to give the same results when the three similarity parameters: enthalpy, pressure, and velocity gradient; were properly accounted for. This is consistent with the theoretical view of stagnation point heating, as shown in the earlier paper [7]. While either facility can and should be used for detailed gas-surface interaction investigations, we have chosen to focus on ICP facilities for the remainder of

this paper, owing to easier access to the boundary layer in the shock-free flow and to contaminant-free operation.

For incompressible flow, as in the subsonic ICP facilities, stagnation point heat transfer to a hemisphere can be represented by the following correlation of non-dimensional parameters:[8]

$$St\sqrt{Re_x} = 0.76(Pr)^{-0.6} \quad , \quad (1)$$

where the Stanton Number,  $St$ , is the non-dimensional heat transfer, defined as:

$$St = \frac{q_w}{\rho u c_p (T_\infty - T_w)} \quad , \quad (2)$$

$Re_x$  is the length-based Reynolds number, and  $Pr$  is the Prandtl number. After substituting for the Stanton number, Eq. (1) can be rearranged and solved for the actual stagnation point heat transfer:

$$q_w = 0.76(Pr)^{-0.6}(\rho\mu\beta)^{0.5}(h_\infty - h_w) \quad , \quad (3)$$

where  $h$  is the enthalpy,  $\rho$  is the density,  $\mu$  is the viscosity and  $\beta$  is the velocity gradient at the boundary layer edge,  $\beta = du/dx$ . The velocity gradient characterizes the acceleration of the plasma flow around the test article. In a previous paper, measured values of free-stream velocity were used to compute velocity gradients in the 6 MW L3K arc-jet at the Deutsches Zentrum für Luft und Raumfahrt (DLR) and the 1.2 MW Plasmatron ICP at the von Karman Institute for Fluid Dynamics (VKI). These calculations showed that the velocity gradient in the ICP facility was nearly a factor of 10 less than in the supersonic arc-jet flow at the same nominal enthalpy and pressure [7]. Since the flow residence time is inversely proportional to the local velocity gradient, this implies that there is more time available for gas-phase and surface-initiated reactions in ICP facilities than in arc-jets, which provides an additional motivation for choosing an ICP test facility for this study.

With this scaling for heat flux in mind, the VKI Boundary Layer Code was used to calculate stagnation-line profiles of temperature and species number densities in the boundary layer above a material surface for different test and boundary conditions with a nearly constant value of the stream enthalpy. These calculations are presented in the following section.

### III. Boundary Layer Calculations

The aero-thermal test conditions for the proposed investigation were selected based on considerations of typical re-entry vehicle design trajectories. Although other planetary atmospheres pose significant challenges to exploration vehicle design, earth re-entry was chosen for this investigation since all plasma ground-test facilities are designed to operate with air. In addition, because of the efforts of the combustion community, there are diagnostic techniques available for probing most species of interest, and some of these diagnostic techniques have already been implemented in plasma facilities as part of stream characterization activities. [9-14]

The VKI Boundary Layer Code was developed as a computationally efficient means for analyzing stagnation point heating for trajectory simulation and for simulation of test

conditions in plasma facilities [15]. Rather than solving the full Navier-Stokes equations, the code instead solves the transformed boundary layer equations for chemically reacting flows over two-dimensional or axisymmetric stagnation region geometries. This allows the diffusion fluxes to be accurately modeled with the exact Stefan-Maxwell equations [16]. A full description of the code and comparisons with Navier-Stokes simulations can be found in Ref. 17.

The surface recombination reactions converting O atoms to O<sub>2</sub> and N atoms to N<sub>2</sub> are assumed to proceed independently and with the same efficiency. This reaction efficiency is specified by the recombination coefficient,  $\gamma$ , defined as the fraction of atoms that collide with the surface that result in loss of the atom from the gas phase. Nitric oxide production at the surface is assumed to be zero (despite evidence to the contrary [18]). In addition, full energy accommodation at the surface from the recombination reactions is assumed for calculating heat flux for the different recombination rates. Gas phase chemistry is modeled with a 5 species chemical non-equilibrium air chemical model under the thermal equilibrium assumption. Chemical reaction rate constants from Dunn & Kang [19] are computed using the Arrhenius constants given in Appendix A. This particular chemical kinetics model has been widely used within VKI and also in the literature. Minor differences in terms of heat flux have been found using alternative kinetics models, such as that of Park [20].

For the present study, the VKI Boundary Layer Code has been used in its “classical” mode, which means a high Re number outer flow and an infinitely thin boundary layer is assumed [17]. All computations are well converged and the 100 point discretization that was used has been shown to be sufficiently grid independent in an earlier study. [17] In all cases, we assume that the surface conditions are not varying with time.

The baseline configuration for the calculations was chosen to represent test capability in “small” ICP facilities, such as the 15 kW VKI Minitorch and the 30 kW ICP Facility at U. Vermont. The parameters for this configuration include a probe radius of 12.5 mm (with corresponding edge velocity gradient of 5000 s<sup>-1</sup>), a boundary layer edge temperature of 6000 K, static pressure of 50 hPa, and a non-catalytic surface. For an air plasma at this temperature and pressure, the corresponding enthalpy value is 25.9 MJ/kg, which represents an atmospheric entry speed of about 7.2 km/s. To assess the influence of changing parameters 8 computations were carried out varying: static pressure (50 hPa to 200 hPa), probe radius (12.5 mm to 25 mm) and surface recombination coefficient ( $\gamma = 0$  to  $\gamma = 1$ ). For all computations, the boundary layer edge temperature is kept constant, and the wall surface temperature is arbitrarily set to 1000 K. Finally, the boundary layer edge plasma is considered to be in thermo-chemical equilibrium, thereby fixing the chemical composition to be nearly identical for all cases.

The boundary layer properties for the baseline configuration ( $p = 50$  hPa,  $R = 12.5$  mm, and  $\gamma = 0$ ) are shown below in Fig. 1. Rather than using either mass fraction or mole fraction, species number densities are shown, along with temperature as a function of distance from the material surface. This is done because number density and temperature are the basic measurable quantities for laser diagnostics of reacting species. At these conditions, the air plasma is highly dissociated, and the major species are N, O, and N<sub>2</sub> in

order of number density. As there is not much change in these properties beyond 8 mm, the axial distribution is shown only that far. Temperature begins to decrease strongly at 4 mm from the surface. Owing to constant static pressure, the total density increases in the boundary layer going toward the surface. All the major species densities follow this trend, and the increasing density also leads to some gas phase recombination. After an initial decrease, the  $O_2$  and NO densities also increase toward the surface.

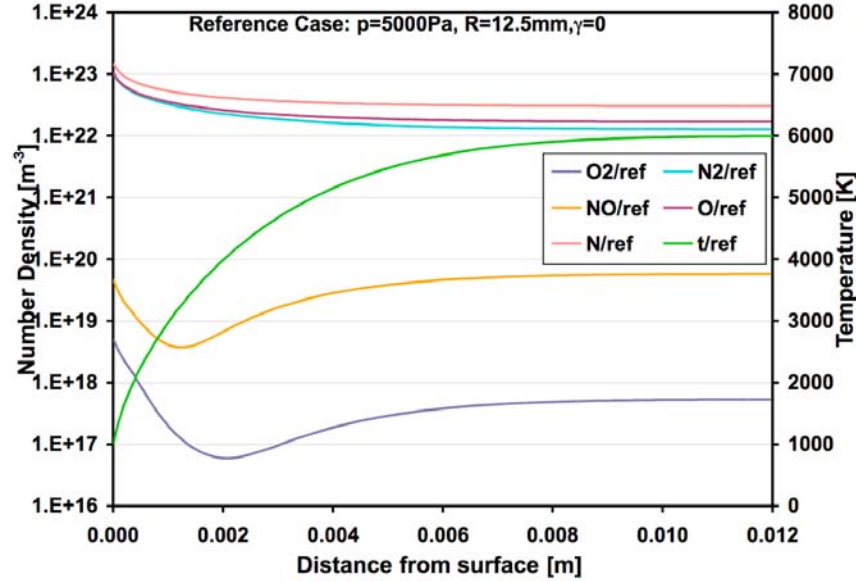


**Fig. 1.** Temperature and species number density distributions in boundary layer for baseline conditions ( $R = 12.5$  mm,  $p = 50$  hPa,  $\gamma = 0$ ).

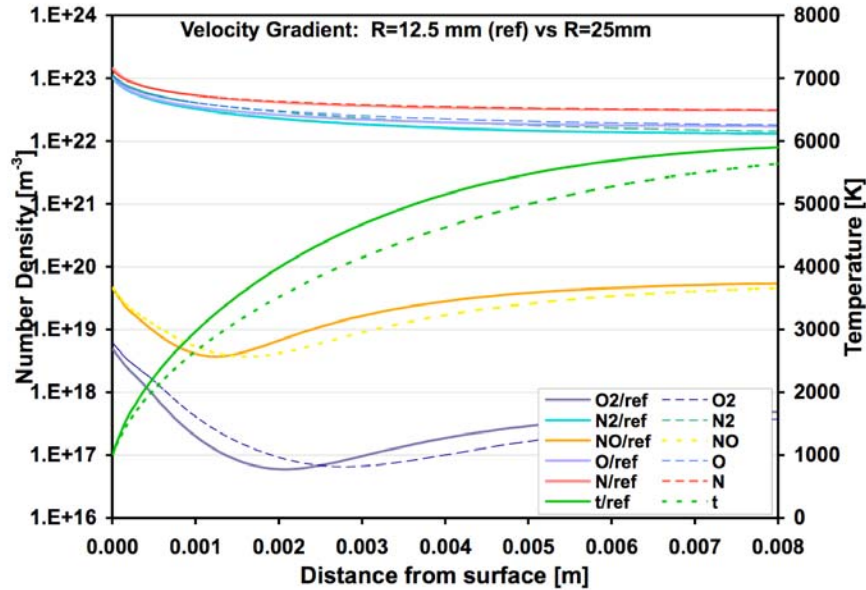


**Fig. 2.** Effect of increased probe radius (decreased velocity gradient) on species distributions in boundary layer for  $p = 50$  hPa and  $\gamma = 0$ .

The influence of the sample holder diameter on the boundary layer distributions for a non-catalytic surface was investigated by doubling the diameter, and a comparison of the two sets of temperature and species density profiles is shown above in Fig. 2. Although

the axial distribution is only shown out to 8 mm from the material surface, it is clear that the increased probe diameter thickens the reacting boundary layer. Doubling the probe diameter halves the velocity gradient (for the same free stream velocity), which doubles the flow residence time, thereby allowing further gas phase recombination. Evidence of this is seen in the increased  $O_2$  density at the wall. A thicker boundary layer provides more room for measuring property gradients, but here this appears to be only a marginal benefit.

The low pressure of 50 hPa for the baseline condition is expected to reduce gas-phase recombination in the cooling plasma flowing toward the surface, resulting in a nearly frozen flow. A higher pressure should increase gas phase recombination for flow to a non-catalytic surface. This is studied below in Fig. 3. Note that there is an increase in the overall number density at the outer edge of the boundary layer, owing to the constant temperature condition. The effect of increased pressure is similar to that of decreasing the sample holder radius, which thins the boundary layer region. At 200 hPa, the temperature and species density gradients are significantly increased, with the change now occurring over a 3 mm zone. As discussed further below, such a narrow, high-gradient condition would present a challenge even for optical diagnostic techniques. Clearly, a larger diameter sample holder would be needed to offset the boundary layer thinning at high pressure.

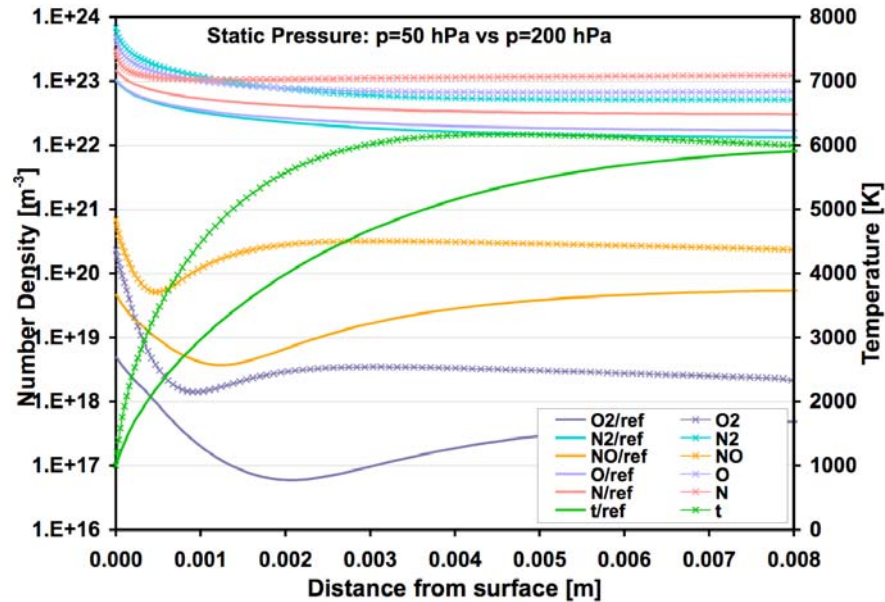


**Fig. 3.** Effect of increasing pressure on boundary layer species distribution for 12.5 mm radius sample holder and  $\gamma = 0$ .

The previous computations were performed to establish the basic boundary layer environment for a given set of plasma and boundary conditions. Those calculations will be used to develop the basic parameters for the optical diagnostic techniques, which would then be used to investigate gas-surface interactions, such as surface-catalyzed recombination. To illustrate this point, Fig. 4 shows a comparison of the baseline species distributions calculated for a non-catalytic wall with results for the same pressure, edge condition, and velocity gradient, but with full surface-catalyzed recombination. It should

be noted that these two limiting cases are ideal. The surface-catalyzed reactions significantly alter the temperature gradient, which shows much steeper change closer to the surface. As expected, there is a strong influence on the species distributions owing to the surface driven production of  $O_2$  and  $N_2$ . Instead of increasing N atom density toward the surface with increasing density, as for a non-catalytic wall, there is a strong decrease for the fully catalytic wall. Finally, although there is no surface production of NO, a strong increase in NO density approaching the surface is also evident.

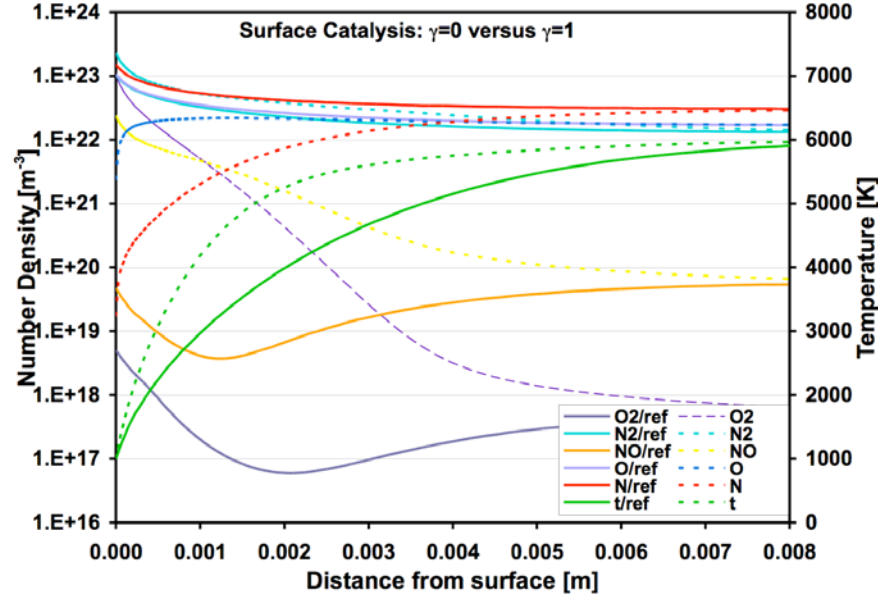


**Fig. 4** Species density distributions for  $p = 50$  hPa,  $R = 12.5$  mm and for different surface recombination rates ( $\gamma = 1$  and  $\gamma = 0$ ).

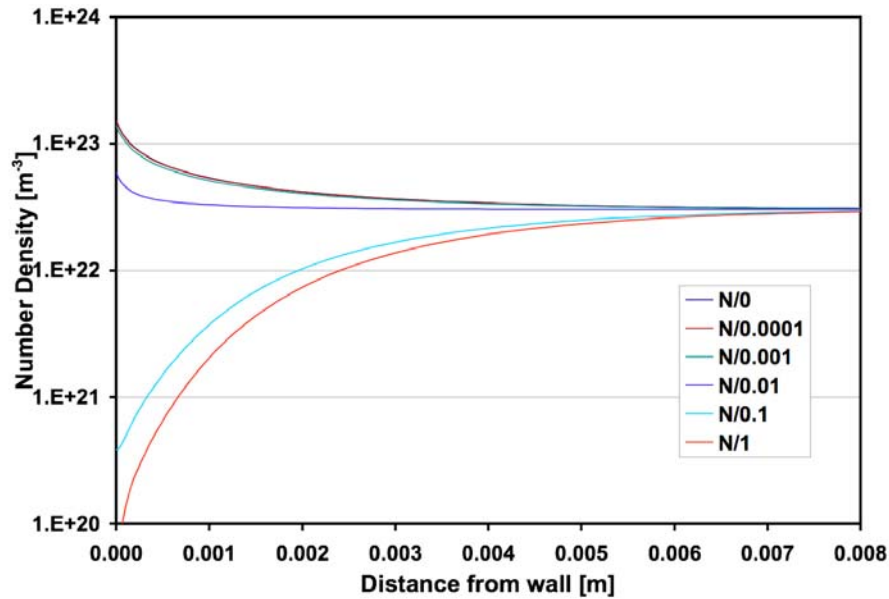


**Fig. 5.** Distribution of N number density for different values of surface recombination rate for the 12.5 mm radius sample holder and 50 hPa pressure.

Again, it should be noted that fully catalytic condition is based on the assumption of independent  $O+O$  and  $N+N$  surface recombination reactions. Moreover, the recombination rate that produces  $\gamma = 1$  is equivalent to assuming an infinitely fast surface reaction rate, which is not realistic. Actual species density distributions for real surface materials will probably lie between the two extremes shown in Fig. 4. This point is further examined in Fig. 5 for the N number density using four additional intermediate values of effective recombination rate. As the surface recombination efficiency decreases, the temperature-driven number density increase toward the wall overcomes N atom losses by the surface recombination to produce an upward trend at the wall. For N atoms, this occurs between  $\gamma = 0.1$  and 0.01.

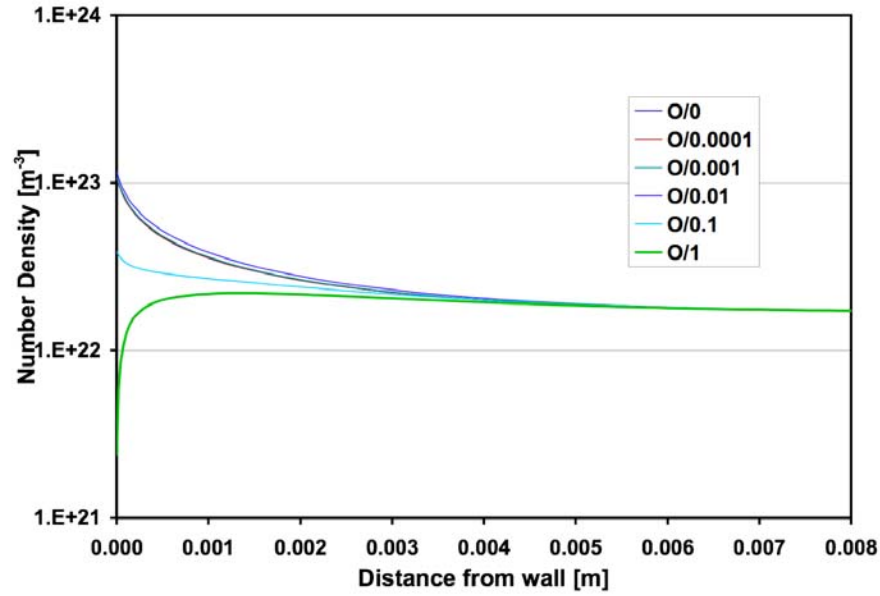


**Fig. 6** Distribution of O number density for different values of surface recombination rate for the 12.5 mm radius sample holder and 50 hPa pressure.

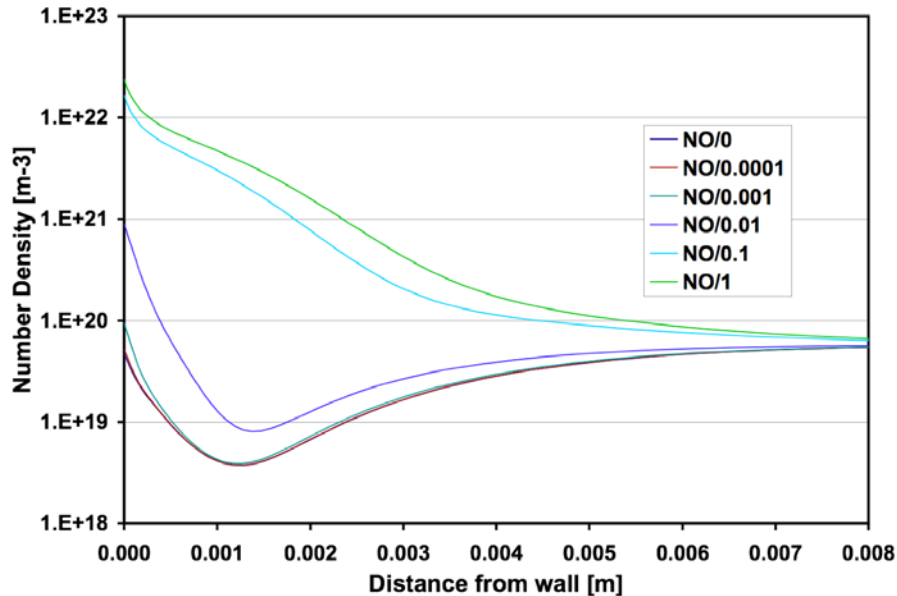


**Fig. 7** Distribution of NO number density for different values of surface recombination rate for the 12.5 mm radius sample holder and 50 hPa pressure.

Figure 6 above shows a similar plot of the different number density distributions for O atoms as a function of different surface recombination rates. Note that while it may be possible to distinguish between  $\gamma = 0.01$  and  $\gamma = 0.1$  (or 1) for  $O+O$  or  $N+N$  recombination, the lower rate trends are all dominated by the density increase toward the wall, and so are not easily identified.

Although the computations did not model  $N+O$  recombination, the different number density distributions for the different surface recombination rates are still interesting, because in all cases they show an increase in NO number density near the wall for any value of the combined  $O+O$  and  $N+N$  recombination rate, as shown below in Fig. 7. This is important for laser diagnostic applications, since it may be possible to obtain information about the rotational and vibrational energies of diatoms from NO.

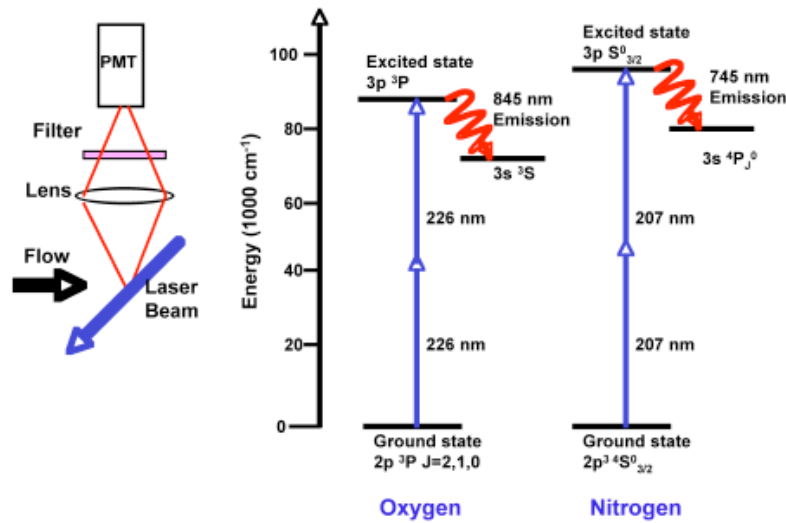


**Fig. 8** Energy levels for LIF of O and N.

#### IV. Laser Diagnostics to Quantify Boundary Layer Properties

Laser induced fluorescence (LIF) is a species selective, non-intrusive diagnostic that has been widely applied for the characterization of combustion and plasma environments. A pulsed, tunable laser source generates monochromatic light at a particular atomic or molecular absorption wavelength. The absorbed photon energy excites the target species to a higher electronic energy level, from which it subsequently decays to a lower energy level, emitting radiation at a characteristic detection wavelength. Applications of LIF to plasma stream diagnosis typically involve measurement of three variables: translational temperature, convective velocity, and species concentration. Air and nitrogen plasma species probed by LIF have included atomic oxygen, atomic nitrogen, and nitric oxide [9-14]. Two-photon LIF has been implemented in arc jets to characterize the free stream conditions and to investigate free stream property gradients [14]. Clearly, for material test applications information from the reacting boundary layer above the material surface is extremely important. While such measurements are relatively rare, published experimental results indicate their feasibility [21].

One advantage of the LIF technique is that ground-state species populations can be probed, since even at relatively high temperatures, the ground electronic state populations typically predominate over the populations in higher electronic levels. Another advantage of LIF is that spatially resolved measurements are more easily made given that the fluorescence collection optics field-of-view and the excitation laser beam axis can be oriented to intersect at a desired location, as shown schematically on the left side of Fig. 8.

For highly dissociated air or nitrogen plasmas, a useful target species is atomic nitrogen, which is a sensitive indicator of the degree of plasma dissociation [12]. Owing to the large electronic energy level spacing, LIF of either oxygen or nitrogen atoms requires two-photon excitation, which yields smaller excitation cross-sections than for single photon LIF. Energy levels involved in one approach for two-photon excitation of atomic nitrogen are shown on the right of Fig. 8 (the other approach is based at 211 nm), while energy levels for the most common excitation strategy for atomic oxygen are shown in the middle. For NO, single-photon excitation in either the ultraviolet  $\gamma$  band ( $A \leftarrow X$ ), near 226 nm or the  $\beta$  band ( $B \leftarrow X$ ) near 207 nm is possible. The convenient overlap between NO single-photon and the two-photon excitation wavelengths for either O or N suggests that two of the three species can likely be probed during a single facility test.

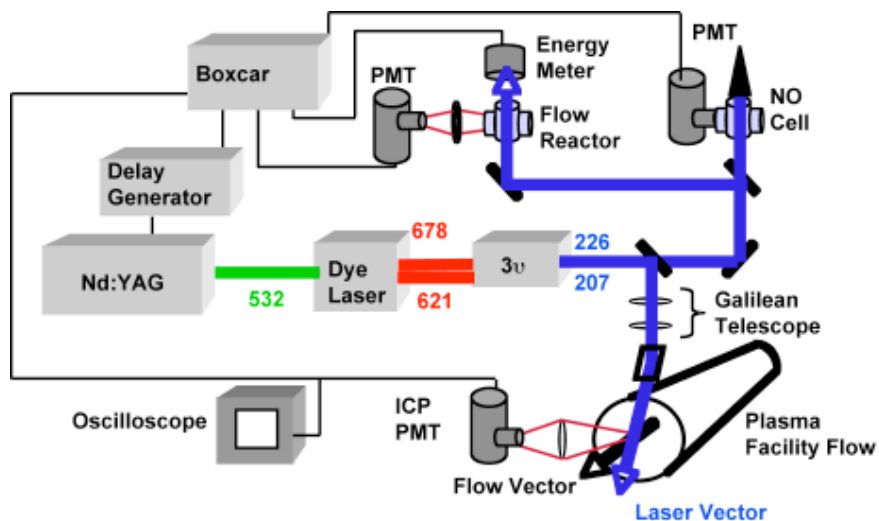


**Fig. 9** Experimental configuration for laser diagnostics of N, O and NO.

For probing either atomic oxygen or atomic nitrogen, the experimental arrangement is essentially the same, as shown below in Fig. 9. A Nd:YAG-pumped dye laser provides the fundamental output, which is converted by the appropriate doubling or tripling crystal arrangement to the desired ultraviolet, two-photon wavelength. Unfortunately, it is not possible with current laser dyes to access both the 207 nm or 226 nm UV wavelengths. As indicated in the figure, the UV output is split into three different paths. The first is directed toward the plasma stream (either ICP or arc-jet), while the other two paths are directed toward a NO reference cell and a microwave-discharge flow reactor, respectively. The NO cell is used to assess the laser performance and to guide laser tuning toward the relatively sparse two-photon excitation wavelengths, and it also provides a mechanism for calibrating NO LIF measurements in the plasma stream.

Within the flow reactor, the microwave discharge creates a stable, non-equilibrium population of atoms at known pressure and temperature, and the fluorescence from this population can be used to calibrate the fluorescence signals from the plasma stream. This calibration enables measurement of translation temperature, velocity (depending on the facility and beam orientation), and number density of the target species.

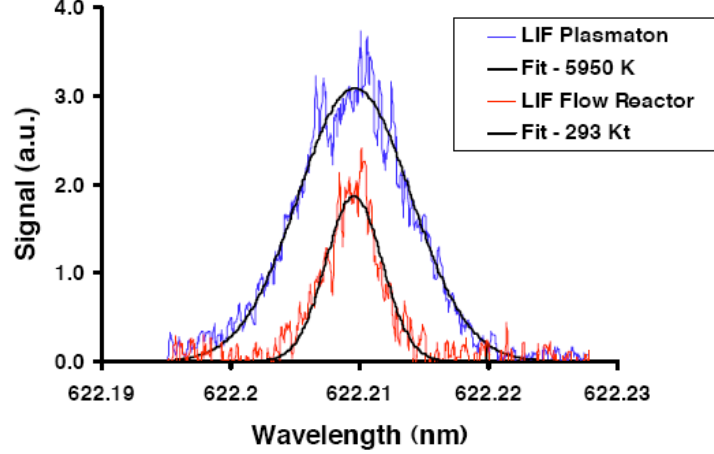


**Fig. 10** Atomic nitrogen LIF signal from boundary layer edge in VKI Plasmatron.

An example of atomic nitrogen fluorescence acquired in an ICP facility is shown above in Fig. 10, where the atomic nitrogen fluorescence is plotted as a function of the dye laser fundamental wavelength. The laser configuration for this system relied on frequency tripling of the dye laser output and the excitation wavelength was 207 nm. The broader of the two traces is the signal collected from plasma stream at the boundary layer edge and the narrower, less noisy signal is from a microwave-discharge flow reactor, where the measurement conditions are independently known. The smooth curves for each LIF signal represent nonlinear least squares fits to the line profiles using a spectral model that includes the relevant broadening mechanisms and uses the total line width as a fit parameter. Line shape fit results from the flow reactor signal are used to extract information from the plasma stream measurements as explained in the following paragraphs. The temperature value derived for this particular measurement is indicated on the figure, along with the flow reactor temperature used to extract the laser line width.

The translation temperature is derived from a measurement of the total width of the transition once the laser line width is determined from the flow reactor line shape as,

$$T = \frac{M_N c^2}{8 \ln(2) k n_A \hat{\nu}^2} [\Delta \hat{\nu}_{T,F}^2 - (\Delta \hat{\nu}_{T,R}^2 - \Delta \hat{\nu}_{D,R}^2)], \quad (4)$$

where  $M_N$  is the molar mass,  $c$  is the speed of light,  $k$  is the Boltzmann constant,  $n_A$  is Avogadro's number, and  $\hat{\nu}$  is the transition frequency in  $\text{cm}^{-1}$ . The different widths (also  $\text{cm}^{-1}$ ) are labeled with subscripts that designate Total or Doppler and Flow or Reactor.

The integrated fluorescence signal is proportional to the local number density of atomic nitrogen. Several additional measurements are required to convert the integrated signal

to number density, including characterization of the collection efficiency, fluorescence lifetime, temporal and spatial characteristics of the laser beam, and finally the use of either a known reference population, a rare gas calibration [14], or a measurement of the two-photon excitation cross-section [12]. For the latter approach, the expression for nitrogen atom number density is

$$n_N = \frac{4\pi}{D} \frac{\tau_{rad}}{\tau_{obs}} \frac{A_P}{\int F^2(t) dt} \frac{(h\nu)^2}{G^{(2)}\sigma^{(2)}} \int \frac{S_N}{E_p^2}(\omega) d\omega, \quad (5)$$

where  $S_N$  is the LIF signal in volts,  $\tau_i$  are the radiative and observed fluorescence lifetimes,  $A_P$  is the beam area,  $D$  is the collection optics calibration factor that can be measured by a Raman scattering experiment [22],  $F^2(t)$  is the square of the temporal pulse and the  $G^{(2)}\sigma^{(2)}$  product represents the cross section times the second-order coherence factor, which depends on the laser configuration [23].

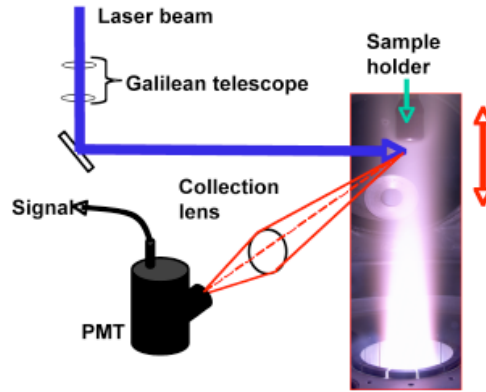


**Fig. 11** Single-point LIF measurements of property gradients in boundary layer.

Two strategies exist for measuring the species and temperature profiles above the surface. The first is a point-wise approach that involves translating the laser probe volume toward the surface, as indicated in Fig. 11, and the other is a planar approach that requires sufficient laser pulse energy to spread the beam into a light sheet. In the latter, an intensified camera is needed to record the fluorescence signals, which complicates the interpretation of the measured signals.

Whether probing N or O, a simultaneous measurement of both the species number density (from the integrated excitation signal as described above) and translational temperature (from the line width) can be obtained at the measurement location. Static pressure is also usually measured during tests in the ICP facility. Thus, from the static pressure and translational temperature, one has the total number density from the ideal gas equation of state

$$n = \frac{P}{kT} . \quad (6)$$

This, along with the species number density, gives the mole fraction of the species from the ratio of number densities. Note that for pure nitrogen plasmas, the measurement of translation temperature and species density can completely characterize the local

thermodynamic conditions, as long as ionization is not significant, since the  $N_2$  number density can be found from

$$n_{N_2} = n - n_N \quad . \quad (7)$$

For air plasmas, measurement of both O and N number densities is required to provide a more complete understanding of the boundary layer conditions.

Based on the species density distributions shown in Fig 4 for the two limiting cases of zero and complete surface recombination, any LIF approach must have a spatial resolution of at least 0.5 mm. This would allow at least eight separate measurements within the steepest gradient region. Both single photon and two-photon LIF techniques have to address nonlinear signal behavior that can result from too great a laser intensity (laser power/beam area) in the probe volume. One example is the onset of multi-photon ionization in the case of two-photon excitation of atomic oxygen, where the limit for avoiding ionization has been published by Bamford [24] as 25 MW/cm<sup>2</sup>. If we assume a uniform energy profile over a 0.5 mm diameter and a square temporal pulse of 5 ns, this limits the beam energy to about 250  $\mu$ J. This limit can be tested *in situ* by monitoring LIF signals as the beam energy is varied and then fitting the slope, which should be linear for single photon LIF and quadratic for two-photon LIF.

However, to evaluate the feasibility of measuring the N atom density gradients, we can use the 0.5 mm beam diameter and 250  $\mu$ J pulse energy to calculate the expected signal levels for comparison with previously published values. By rearranging Eq. 5 to solve for the integrated signal as

$$\int S(\omega) d\omega = \frac{D}{4\pi} \frac{\tau_{obs}}{\tau_{rad}} \frac{\int F(t)^2 dt}{A_p} \frac{G^{(2)} \sigma^{(2)}}{(h\nu)^2} E_p^2 n_N \quad , \quad (8)$$

and values for some of the terms on the right hand side from previously published arc-jet measurements [12], the expected integrated signal level for the 211 nm transition of N can be estimated for different values of  $n_N$ . (Here we use the 211 nm transition instead of the 207 nm transition shown in Fig. 8, owing to the availability of the experimental data.) However, for the arc-jet measurements the photomultiplier tube was far from the measurement location, giving a low value of the detector calibration factor for the f/18 optical system. For our application in a smaller ICP facility, we expect to achieve f/6, and so our value of  $D$  here is set to  $4.6(10)^{-7}$  V-cm-sr, rather than the value of  $1.93(10)^{-8}$  given in Table 2 of [12]. Our static pressure of 50 hPa is considerably greater than the arc-jet value of approximately 2 hPa, and so our fluorescence quantum yield is lower ( $\tau_{obs}/\tau_{rad} = 0.26$ , rather than 0.82 as in [12]). We also use our limiting value of beam area (0.02 cm<sup>2</sup>) and energy (250  $\mu$ J) calculated above. This gives

$$\int S(\omega) d\omega = 1.8(10)^{-12} n_N \text{ (V-rad-s}^{-1}\text{)} \quad , \quad (9)$$

and for a nitrogen atom number density of  $10^{20} \text{ m}^{-3}$  ( $10^{14} \text{ cm}^{-3}$ ) we expect an integrated signal level of approximately 180 V-rad-s<sup>-1</sup>. This is very close to the value of integrated signal (230 V-rad-s<sup>-1</sup>) for the lowest N number density measured in the arc-jet. While the uncertainty in the absolute number densities may be high owing to the low signal levels, the relative number densities are more precisely known, as discussed in [12]. This may allow a reasonable assessment of the predicted species density gradients.

This result suggests that direct measurements of temperature and atomic species density can be used to assess the surface-catalyzed recombination rate for materials with a catalysis parameter  $\gamma$  between 0.001 and 0.1 (refer to Fig. 5). For example, the use of a material surface with a catalysis parameter that has been quantified in a side-arm diffusion reactor (as in [18]) at a controlled surface temperature value in a pure nitrogen plasma would significantly limit the number of free parameters for modeling. While we have used the air plasma calculations as a basis for proposing a test case for reacting boundary layer model assessment, we recognize that the NO chemistry will complicate the interpretation of the test results. Thus, a better starting point for these experimental investigations would be to use a pure nitrogen plasma. Note that another interesting test case would be to measure the N atom density gradient for a non-catalytic material at different pressures. From such measurements it may be possible to assess the gas-phase recombination rate at the boundary layer condition.

The next step in the development of a validation test case is to conduct boundary layer measurements of atomic nitrogen and oxygen for some of the cases discussed here. Specifically, we recommend:

1. Measurement of the temperature and N atom density gradients in a nitrogen plasma for pressures ranging from 50 hPa to 200 hPa (at least) in the region near a non-catalytic material to assess the gas phase reaction:  $N+N+M \rightarrow N_2+M$ .
2. Measurement of the same variables plus the O atom and NO density gradients at the same conditions in air plasma.
3. Measurement of the temperature and N atom density gradient at 50 hPa in a nitrogen plasma in the near wall region of a highly catalytic material (with previously measured recombination probability to assess surface recombination).
4. Measurement of the same variables plus O atom and NO density gradients at the same conditions for air plasma.

For all of these cases, the stream conditions at the boundary layer edge must be well characterized. Based on the documented uncertainty in the measurements, future test case development should focus on the isolation of simpler gas/surface interaction rates for similar investigations.

## V. Summary

The VKI Boundary Layer Code has been used to estimate temperature and species density gradients in the stagnation region of an axisymmetric sample holder. These calculations were done assuming a 5 species air model and using a simplified surface recombination model (equal rates for O+O and N+N, with no NO production). Calculations of the gradients for different diameter sample holders, different static pressures, and varying surface recombination rates show that at the lowest pressure (50 hPa) there are significant differences in the gradients of N and NO approaching the surface.

Results of the calculations for the 50 hPa and smaller sample diameter were then used to assess N atom detection for the 211 nm transition based on published values of

experimental parameters for that two-photon excitation scheme. The estimated integrated signal value compares reasonably well with that from previous measurements, and suggests that N density measurements from two-photon LIF can provide a reliable indication of the reacting boundary layer gradient, which can provide useful information about gas/surface interactions, such as surface catalyzed recombination.

## VI. Acknowledgements

The work of U. Vermont is supported by NASA Grant NNX08AC98A and by AFOSR High-Temperature Aerospace Materials Program Grant FA9550-08-1-0414. The work of SRI International is supported by the High-Temperature Aerospace Materials Program of the Air Force Office of Scientific Research through contract FA9550-08-C-0049.

## VII. References

1. Z. Krevor, G. Epstein, P. Benfield, and G. Deckert, "Leveraging Reliability in Support of Risk Balancing and Weight Reduction on Orion", AIAA 2009-6725, AIAA SPACE 2009, Pasadena, 12-14 September (2009).
2. R. K. Smith, D. A. Wagner, and J. W. Cunningham, "A Survey of Current and Future Plasma Arc-Heated Test Facilities for Aerospace and Commercial Applications", AIAA Paper No. 98-0146, 36<sup>th</sup> Aerospace Sciences Meeting, 12-15 January, Reno, NV, (1998).
3. B. Bottin, O. Chazot, M. Carbonaro, V. Vander Haegen, and S. Paris, "The VKI Plasmatron Characteristics and Performance", NATO RTO EN-8, Neuilly-sur-Seine Cedex, France, pp. 6/1-26, (1999).
4. A. Gülhan and B. Esser, "A Study on Heat Flux Measurements in High Enthalpy Flows", AIAA Paper No. 2001-3011, 35<sup>th</sup> AIAA Thermophysics Conference, 11-14 June, Anaheim, CA (2001).
5. A. F. Kolesnikov, "Extrapolation from High Enthalpy Tests to Flight Based on the Concept of Local Heat Transfer Simulation", NATO RTO EN-8, Neuilly-sur-Seine Cedex, France, pp. 8B/1-14, (1999).
6. J. Grinstead, G. Raiche, T. Gökçen, "Test Engineering for Arc Jet Testing of Thermal Protection Systems: Design, Analysis, and Validation Methodologies", AIAA-2006-3290, 25<sup>th</sup> AIAA Aerodynamic Measurement Technology and Ground Testing Conference, San Francisco, California, June 5-8, (2006).
7. D. G. Fletcher and M. Playez, "Characterization of Supersonic and Subsonic Plasma Flows", AIAA 2006-3294, 25<sup>th</sup> AIAA Aerodynamic Measurement Technology and Ground Testing Conference, San Francisco, California, June 5-8, (2006).
8. F. M. White, Viscous Fluid Flow, McGraw-Hill, New York, p. 183, (1974).
9. D. J. Bamford, A. O'Keefe, D. S. Babikian, D. A. Stewart, and A. W. Strawa, "Characterization of Arc-Jet Flows Using Laser-Induced Fluorescence", *J. Thermophysics and Heat Transfer*, **9**, pp. 26-33, (1995).
10. U. Koch, A. Gülhan, B. Esser, F. Grisch, and P. Bouchardy, "Rotational and Vibrational Temperature and Density Measurements by Planar Laser-Induced NO Fluorescence in a Nonequilibrium High Enthalpy Flow", RTO/AGARD Fluid

- Dynamics Panel Symposium, Advanced Aerodynamic Measurement Technology, Seattle, Wa 22-25 September, (1997).
11. M. Feigl, and M. Auweter-Kurtz, "Investigation of Nitric Oxide in a High Enthalpy Air Plasma Flow Using Laser-Induced Fluorescence", AIAA Paper No. 98-2459, 7<sup>th</sup> AIAA/ASME Joint Thermophysics Conference, Albuquerque, NM, July, (1998).
  12. D. G. Fletcher, "Arcjet Flow Properties Determined from Laser-Induced Fluorescence of Atomic Nitrogen", *Applied Optics*, **38**, No. 9, pp. 1850-1858, March, (1999).
  13. D. G. Fletcher and D. G. Bamford, "Arcjet Flow Characterization Using Laser-Induced Fluorescence of Atomic Species", AIAA Paper No. 98-2458, 7<sup>th</sup> AIAA/ASME Joint Thermophysics Conference, Albuquerque, NM, July, (1998).
  14. J. H. Grinstead, D. M. Driver, and G. A. Raiche, "Radial Profiles of Arcjet Flow Properties Measured with Laser-Induced Fluorescence of Atomic Nitrogen", AIAA Paper No. 2003-0400, AIAA 41<sup>st</sup> Aerospace Sciences Meeting, Reno, NV, 6-9 January, (2003).
  15. P. F. Barbante, "Accurate and Efficient Modeling of High Temperature Non-equilibrium Air Flows," Ph.D. Thesis, Univ. Libre de Bruxelles, Bruxelles, Belgium, (2001).
  16. P. F. Barbante, "How Diffusion Modeling Affects Prediction of Heat Flux Loads," Sixth European Symposium on Aerothermodynamics of Space Vehicles, SP-659, ESA, Noordwijk, The Netherlands, p. 14-1, 3-6 Nov. (2008).
  17. P. F. Barbante, "Heat Flux Duplication Between Ground Facility and Hypersonic Flight", *J. Thermophysics and Heat Transfer*, **23**, pp. 684-692, October-December, (2009).
  18. D.A. Pejakovic, J. Marschall, L. Duan, and M.P. Martin, "Nitric Oxide Production from Surface Recombination of Oxygen and Nitrogen Atoms," *J. Thermophysics and Heat Transfer*, **22**, pp. 178-186, (2008).
  19. M. G. Dunn and S. W. Kang, "Theoretical and Experimental Studies of Reentry Plasmas", NASA Technical Report CR-2232, (1973).
  20. C. Park, "Review of Chemical-Kinetic Problems of Future NASA Missions, I: Earth Entries, *J. Thermophysics and Heat Transfer*, **7**, pp. 385-398, (1993).
  21. T. Laux, M. Feigl, T. Stockle, and M. Auweter-Kurtz, "Estimation of the surface catalycity of PVD-coatings by simultaneous heat flux and LIF measurements in high enthalpy air flows," AIAA 34<sup>th</sup> Thermophysics Conference, Denver, CO, 2000.
  22. W. K. Bischel, D. J. Bamford, and L. E. Jusinski, "Absolute calibration of a fluorescence collection system by Raman scattering of H<sub>2</sub>", *Appl. Opt.*, **25**, pp. 1215-1221, (1986).
  23. D. J. Bamford, W. K. Bischel, A. P. Hickman, and M. J. Dyer, "Measurement of Two-Photon Absorption Cross Sections in Atomic Oxygen at 226 nm: Single-Frequency versus Multi-mode Lasers", *SPIE*, **912**, pp. 139-144, (1988).
  24. D. J. Bamford, L. E. Jusinski, and W. K. Bischel, "Absolute two-photon absorption and three-photon ionization cross sections for atomic oxygen", *Phys. Rev. A*, **34**, pp. 185-198, (1986).

## VIII. Appendix A

Chemical model for the mixture air5.mix (Dunn & Kang)

-----  
The constants for the chemical reactions are in the order: cf bf ef

CGS Unit system

NR = 17.0

$O_2 + N = 2O + N$

3.600e+18 -1.00 5.950e+04

$O_2 + NO = 2O + NO$

3.600e+18 -1.00 5.950e+04

$O_2 + O = 2O + O$

9.000e+19 -1.00 5.950e+04

$O_2 + O_2 = 2O + O_2$

3.240e+19 -1.00 5.950e+04

$O_2 + N_2 = 2O + N_2$

7.200e+18 -1.00 5.950e+04

$N_2 + O = 2N + O$

1.900e+17 -0.50 1.130e+05

$N_2 + NO = 2N + NO$

1.900e+17 -0.50 1.130e+05

$N_2 + O_2 = 2N + O_2$

1.900e+17 -0.50 1.130e+05

$N_2 + N = 2N + N$

4.085e+22 -1.50 1.130e+05

$N_2 + N_2 = 2N + N_2$

4.700e+17 -0.50 1.130e+05

$NO + O_2 = N + O + O_2$

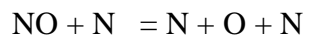
3.900e+20 -1.50 7.550e+04

$NO + N_2 = N + O + N_2$

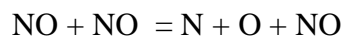
3.900e+20 -1.50 7.550e+04

$NO + O = N + O + O$

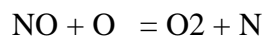
7.800e+21 -1.50 7.550e+04



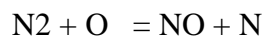
7.800e+21    -1.50   7.550e+04



7.800e+21    -1.50   7.550e+04



3.200e+09    1.00   1.970e+04



7.000e+13    0.00   3.800e+04

# Investigations of Surface-Catalyzed Recombination Reactions in the Mars Atmosphere

Max Dougherty\*, Walt Owens\*, Jason Meyers<sup>†</sup> and Douglas Fletcher<sup>‡</sup>

*University of Vermont, Burlington, Vermont, 05401, USA*

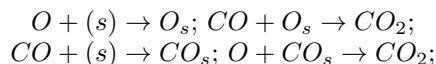
In the design of a thermal protection system (TPS) for a planetary entry vehicle, accurate modeling of the trajectory aero-heating poses a significant challenge owing to large uncertainties in chemical processes taking place at the surface. Even for surface-catalyzed reactions, which have been investigated extensively, there is no consensus on how they should be modeled; or, in some cases, on which reactions are likely to occur. Current TPS designs for Mars missions rely on a supercatalytic boundary condition, which assumes that all dissociated species recombine to the free stream composition. While this is recognized to be the most conservative approach and leads to an increased TPS mass, discrepancies in aero-heating measurements in ground test facilities preclude less conservative design options. The present work is aimed at providing more information about surface catalyzed reactions for Mars exploration missions. Measurements of dissociated species above a catalytic surface are obtained using two-photon absorption laser-induced fluorescence (TALIF) implemented in a new 30 kW inductively coupled plasma torch facility.

## I. Introduction

Aerothermodynamic heating presents a significant challenge in the design of a thermal protection system for atmospheric reentry. Surface catalyzed recombination reactions must be considered in any heat flux analysis of a candidate TPS due to the significant chemical energy produced during recombination.<sup>3</sup> Despite a sustained effort to investigate surface catalyzed reactions and to develop realistic physics based models for implementation in design codes, the state of the art relies on relatively simple surface boundary conditions. These are (in order of predicted heat flux level): a) supercatalytic, which assumes that all dissociated species recombine to their free stream values; b) fully-catalytic, in which surface catalytic reactions occur with an infinite rate; c) partially catalytic, which is used when catalytic properties of the surface material are known for all recombining species and includes finite reaction rates; and d) non-catalytic, which assumes that no surface recombination reactions occur. Depending on the gas composition and entry velocity, the difference in predicted heat flux between non-catalytic and fully catalytic can be a factor of two or more. Figure 1 shows a comparison of computed heat flux values for different surface recombination models. The extreme difference in heating between non-catalytic and supercatalytic is readily apparent.

Owing to high interest in scientific missions to Mars, surface catalysis in the Mars atmosphere is a topic that merits further study. The Martian atmosphere contains approximately 97% CO<sub>2</sub> and 3% N<sub>2</sub> by volume, and trace amounts of other species (Ar, O<sub>2</sub>, etc.). During entry into this atmosphere, CO<sub>2</sub> molecules readily dissociate into CO and O when a shockwave is encountered. The major species of interest are therefore CO, O, C, N, and NO.

The Mitcheltree model<sup>4</sup> considers the following reactions:



---

\*Graduate student, School of Engineering, 33 Colchester Ave, Burlington, VT 05401 USA

<sup>†</sup>Post-doctoral researcher, School of Engineering, 33 Colchester Ave, Burlington, VT 05401 USA, member AIAA

<sup>‡</sup>Professor, School of Engineering, 33 Colchester Ave, Burlington, VT 05401 USA, Associate Fellow AIAA

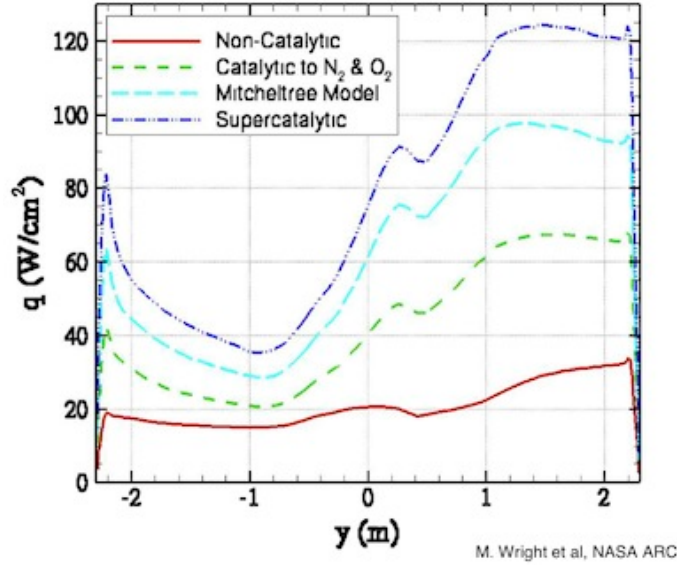
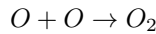


Figure 1: Computed heat flux for various catalytic models for Mars Science Laboratory trajectory peak heating<sup>5</sup>

where  $(s)$  represents a surface adsorption site. These reactions assume an Eley-Rideal (ER) recombination mechanism. Because it produces the dominant free stream molecule, it closely resembles the supercatalytic assumption. This model ignores the competing reaction:



However, in laboratory side-arm diffusion reactor tests,<sup>12</sup> it has been found that the oxygen recombination occurs more readily than carbon dioxide recombination and as a result, it is likely that the supercatalytic assumption is overly conservative.

For this reason, surface catalyzed reactions in the Mars atmosphere are being studied using laser spectroscopic techniques in a new 30 kW Inductively Coupled Plasma (ICP) Torch Facility. Despite its normally subsonic operation, an ICP facility has two main benefits over arc-jet facilities: 1) plasma is generated using radio-frequency coupling, without electrodes, and therefore is free of contaminants; and 2) the composition of the test gas can be varied quickly and accurately. Moreover, scaling of the stagnation point heat flux between an ICP facility and arc-jets is understood, as both facilities must match the same set of flight parameters: total enthalpy, post-shock total pressure, and stagnation point velocity gradient. In principle, the boundary layer of such a facility is very similar to that found in a flight condition at the stagnation point provided that these similarity parameters are duplicated.

The goal of the current work is to characterize surface catalyzed reactions in the Martian atmosphere by measuring the major species in the boundary layer, including the arriving species flux rates. It is expected that the results of these experiments will show which recombination reactions prevail for a Mars entry flight condition and will provide a basis from which to create more accurate surface recombination models for CO<sub>2</sub> and N<sub>2</sub> plasmas.

After a brief discussion of the thermodynamics of the Mars atmosphere mixture, the 30 kW ICP Torch Facility is described and the laser diagnostic strategies being implemented for this investigation are presented. Preliminary results from boundary layer surveys of the reactants are presented and discussed, and the present findings are summarized.

## II. Computational approach

In order to determine equilibrium properties for gas mixtures used in the ICP facility, the MUTATION (MUlti-component Transport And Thermodynamic properties/chemistry for IONized gases) library<sup>7</sup> is used.

MUTATION is a thermodynamic library that provides thermodynamic and transport properties for user-defined gas mixtures. Figure 2 is a plot of the equilibrium mass fraction for an 8 species  $\text{CO}_2$  model ( $\text{e}^-$ , C, O, CO,  $\text{CO}_2$ ,  $\text{O}_2$ ,  $\text{C}^+$ ,  $\text{O}^+$ ) at 100 torr from 600 to 10,000 K. At roughly 2000 K,  $\text{CO}_2$  begins to dissociate into O and CO. There is an increase in  $\text{O}_2$  with a maximum at 3000 K. Between 4000 and 6000 K, CO and O are the dominant species in the mixture. At roughly 6500 K, the ratio of CO to O is one-to-one. Beyond this point, CO dissociates and its constituent atoms begin to ionize. For pure  $\text{CO}_2$ , the 30 kW ICP Torch Facility has achieved boundary layer edge temperatures approaching 5500 K, suggests a CO:O mass ratio of approximately 65:35 entering the boundary layer.

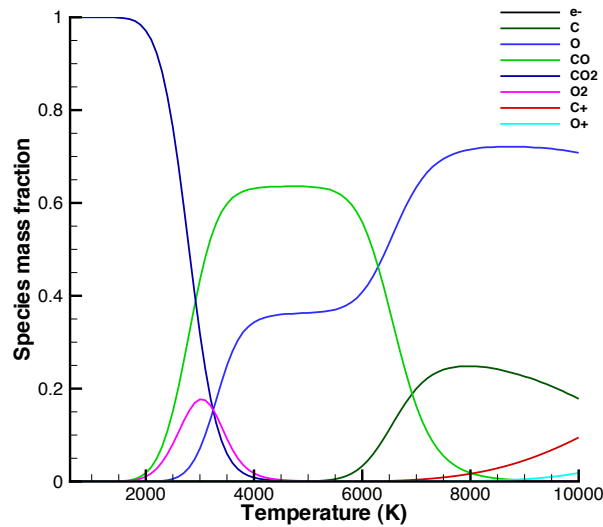


Figure 2: **Equilibrium composition of 8 species  $\text{CO}_2$  from MUTATION**

### III. Facility description

The plasma diagnostics lab at the University of Vermont is built around a 30 kW ICP Torch. The torch itself is comprised of three main systems: the radio frequency (RF) power supply, the injector block assembly, and the test chamber. The power supply can generate up to 30 kW at frequencies from 2.5 to 4 MHz. The plasma is generated within a quartz tube connected to the injector block. Quartz is used because it is considered to be a non-reacting material and thus will not alter the plasma chemistry. Surrounding the quartz tube is a water-cooled copper coil through which current is run from the power supply, inducing an RF magnetic field within the quartz tube and thus creating the plasma. A table of the ICP Torch Facility parameters is given in Table 1. Gas flows are metered by mass flow controllers, usually with a predetermined flow rate and a vacuum pump is used to regulate the static pressure in the test chamber.

Inductive heater power [kW]	30
Enthalpy range [ $\text{MJ kg}^{-1}$ ]	10 - 40 (for air)
Mach range	< 0.3 to 1
$q_{stag}$ , [ $\text{W cm}^{-1}$ ]	10-290
$P_{stag}$ , [atm]	0.05 - 1.0
Plasma jet diameter [mm]	36
Test gas	air, Ar, $\text{N}_2$ , $\text{CO}_2$ , variable mixture fractions

Table 1: **Plasma torch parameters**

Test sample surface temperature is measured with a two-color pyrometer that observes the sample surface directly through an angled viewport on the bottom flange of the test chamber. A two-color pyrometer is used because it can provide a surface temperature measurement without having to know the material surface emissivity. By calibrating both pyrometer channels, the device can also provide an emissivity value for the detection wavelength. Heat flux measurements are taken with either a slug calorimeter or a gardon gage before samples are placed in the plasma flow. Temperature measurements for the slug calorimeter are obtained from a thermocouple attached to the back of the copper slug. Measured heat flux values from the facility have been reported elsewhere.<sup>9</sup> Test chamber static pressure measurements are obtained from a port on the chamber. Table 2 shows a list of the current capabilities of the ICP facility.

Figure 3 shows a picture of the test chamber and the power supply. Although the photo is fairly crowded, the 30 kW RF power supply is on the left, and the stainless steel test chamber is in the center. Below the chamber, the two valves that provide back-up control of the start gas (argon) and gas mixture (variable) are visible, and the pyrometer is just above these two valves. The facility vacuum pump is seen at the upper right of the photo, and the optical bench containing the three-axis staging that allows translation of the photomultiplier tube (PMT) and detection optics is just to the right of the chamber.

Maximum run time [min]	60
Maximum recorded heat flux [ $\text{W cm}^{-2}$ ]	105
Maximum operating pressure [torr]	180

Table 2: **Current ICP capabilities**

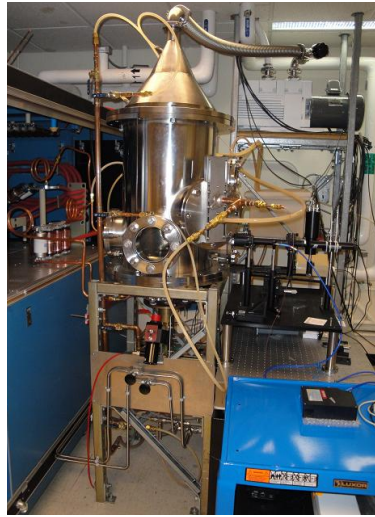


Figure 3: **Picture of the test chamber and power supply<sup>9</sup>**

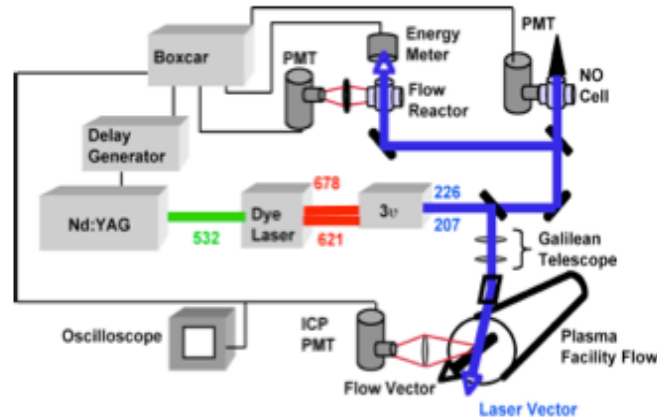


Figure 4: **Schematic of the plasma diagnostics facility and laser system**

The 30kW ICP Torch Facility at UVM was designed to accommodate laser-spectroscopic instrumentation, and so has substantial optical access through fused silica windows located on orthogonal flanges in the horizontal plane above the quartz tube. A Nd:YAG-pumped dye laser with attendant electro-optical components is installed along the wall opposite the ICP Torch. Figure 4 shows a schematic representation of the plasma diagnostics facility and the laser system. For the present investigation, a dye mixture of 75% LDS 698 and 25% DCM is used to provide tunable visible radiation over a wavelength range of 670 to 710 nm. Two INRAD Autotrackers are used to generate frequency tripled radiation from the dye fundamental and the UV photons enable two-photon laser induced fluorescence (LIF) probing of the target species for this investigation: CO and O. A beam splitter is used to direct 10% of the beam to a microwave discharge flow reactor. Additional beam splitters are used in the ICP beam path to control the laser energy density in the focal volume of the ICP facility. Currently, only 30% of the available beam energy is used in the ICP facility, as the laser beam is tightly focused to provide high spatial resolution in thin boundary layers. The energy is reduced to avoid stimulating additional multiphoton processes that can interfere with the LIF signals. Signals are detected at both locations using gated PMTs, and all signals are recorded with gated integrators. Pulse energies are measured at both locations with Molelectron energy meters.

The flow reactor is used to calibrate O atom LIF measurements acquired in the plasma stream of the ICP Torch Facility. This is done by creating an O atom population at known temperature and pressure in the discharge. Simultaneous excitation of the transition in the ICP and the flow reactor, along with measurement of additional detection parameters (detection efficiency, fluorescence lifetime, and beam waist) at the two locations allows a determination of the absolute concentration of the atomic oxygen in the ICP. For CO a simpler calibration is done by placing a cell containing CO at the measurement location. Ideally, the cell pressure will match the static pressure obtained during the ICP tests.

The objective of the present investigation is to obtain quantitative measurements of CO and O atom densities in the reacting boundary layer over catalytic and noncatalytic surfaces to assess their relative recombination probabilities. Figure 5 shows the excitation strategies for CO and O. Both of these schemes require two-photon excitation owing to the large separation between the lower and upper state energy levels. The excitation for O atoms occurs at 226 nm, with detection at 845 nm, while the excitation for CO occurs at 230 nm. The filter used for CO detection is a 70 nm bandpass filter centered at 480 nm, and is definitely sub-optimal. Fortunately both species can be accessed without changing the laser dye, and as the filters are mounted in a wheel at the detection PMT, both species can actually be accessed during a single facility test, although for reasons discussed below this has not yet been achieved.

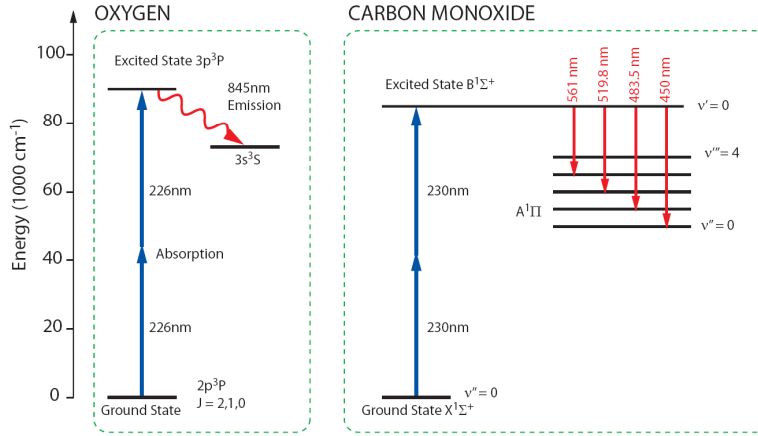


Figure 5: Excitation wavelengths for O and CO<sup>10</sup>

The methods for determining species density and translational temperature from the detected LIF signals are described in detail elsewhere.<sup>11</sup> Briefly, temperature is extracted from spectral model fits to the excitation spectra and number density for each species is determined from spectrally integrated LIF data. As long as the detection optics and PMT bias voltage are unchanged, the spectral integrated signals are proportional to relative species number density. Absolute number densities are determined through the calibrations mentioned above.

## IV. Results

Initial tests were performed during the summer to verify laser operation and to assess detection strategies for both CO and O. Recent tests have included attempts to obtain spatially resolved measurements during ICP tests in the reacting boundary layer above a water-cooled copper surface. Data from these preliminary tests are discussed in this section.

Tests were performed on a 12.5 mm cooled copper disk mounted in a 25 mm diameter cooled brass sample holder. Copper was chosen as the material for the initial tests as it is known to catalyze oxygen and nitrogen recombination in plasma test facilities, even though it is known to be less than fully catalytic. A table showing typical test conditions can be seen in Table 3. Unfortunately, owing to difficulties with the power supply argon was added to the gas mixture for tests with CO as the target species. The cause of the power supply instabilities is currently being investigated.

LIF target species	pressure (torr)	$\dot{m}_{CO_2}$ (g/s)	$\dot{m}_{Ar}$ (g/s)
O	98	0.9296	0
CO	103	0.8997	0.3536

Table 3: **Typical test conditions**

The first tests were done for 100% CO<sub>2</sub> plasma, with atomic oxygen as the LIF target species. A scan of the  $J'' = 2$  fine level of the  $3p^3P_{2,1,0} \leftarrow 2p^3P_2$  transition is shown below in Figure 6. The signal from the ICP is represented by the red trace, which shows a pattern of enhanced noise on the right side of the trace over a limited wavelength region. This excess noise occurred at different wavelengths for all of the scans during this ICP run, and appeared to affect only the PMT closest to the test chamber. The source of this noise is also currently being investigated. Despite the noise, the spectral model provides a reasonable fit to the experimental data. The blue trace (and red fit) are from the simultaneous measurement in the flow reactor. The fit to the reactor data provides the laser line width, which allows extraction of the translational temperature from the ICP data. Similar data are acquired at the different locations of the boundary layer survey, and at each location the spectral fit provides a temperature value, while the spectrally integrated

signal provides an indication of the relative O atom number density. All of the measurements needed to convert the relative number densities to absolute values have been performed, including Raman calibrations of both detection systems, beam profile and fluorescence lifetime measurements. However, the chemical titration to establish the reference population of oxygen atoms in the flow reactor has not been done, so only the relative density information is discussed below.

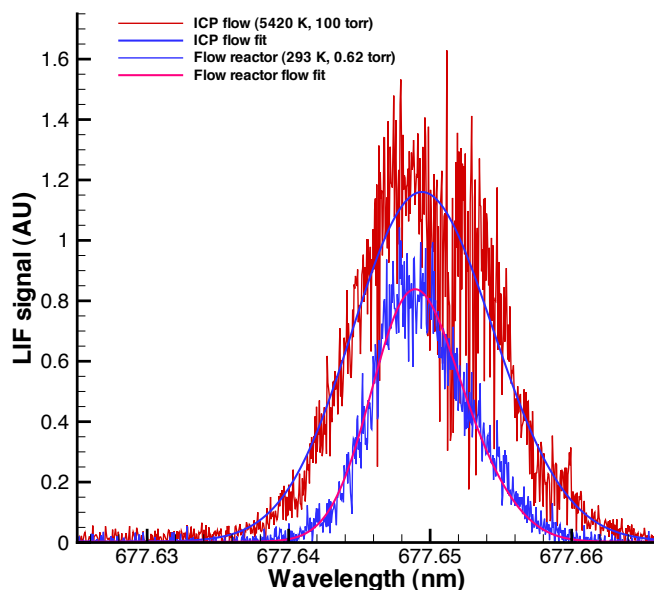


Figure 6: LIF signal from oxygen atom scan

Figure 7a shows the temperature profile derived from oxygen atom scans. The scans appear to have covered the extent of the boundary layer, which appears to be on the order of 1.5 mm for the 25 mm cooled probe placed in the plasma stream. Relative number density of oxygen atoms is seen to decrease through the boundary layer approaching the wall, as shown in Figure 7b. This decrease implies that some mechanism is depleting the O atom population at the wall. If such a depleting mechanism was not operating, the relative number density of O atoms would follow the total number density assuming that gas-phase recombination is relatively slow,<sup>13</sup> and the data trend would be upward toward the wall. As copper is known to catalyze the reaction  $O + O(s) \rightarrow O_2$ , the decreasing trend of relative number density for oxygen is not surprising, and the O atom depletion mechanism is presumed to be surface-catalyzed recombination.

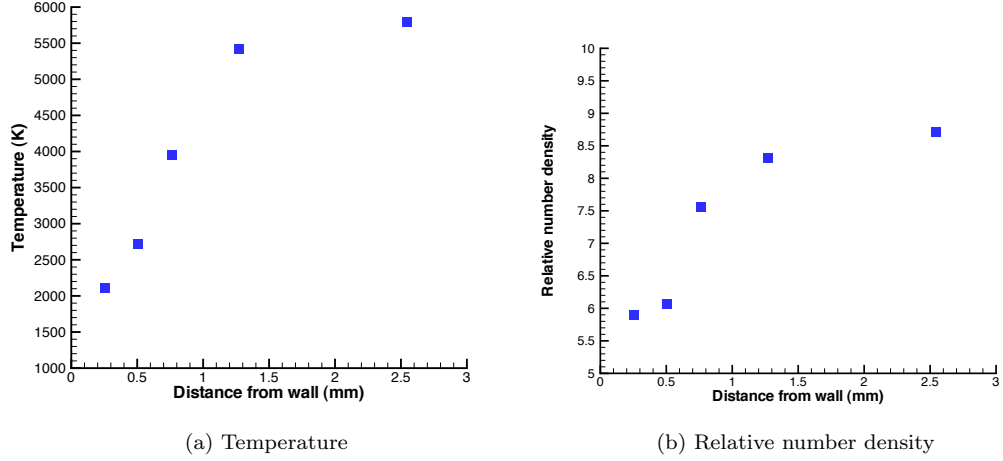


Figure 7: **Temperature and relative number density for oxygen atom scans**

Following the O atom measurements, several repairs had to be made to facility components, including a complete rebuild of the injector block. From that point, facility operation proved difficult or inconsistent with pure CO<sub>2</sub> and further modifications were made to the power supply tank circuit. Finally, owing to time constraints operation was attempted with the CO<sub>2</sub>:Ar mixture defined in Table 3. above, and this allowed steady operation for relatively short test times. Each test lasted for approximately two limited (0.1 nm) wavelength scans of the CO ( $B^1\Sigma^+ \leftarrow X$ ) (0,0) absorption band at the predetermined boundary layer locations. Following each shut-down the facility was restarted at approximately the same test conditions.

Figure 8 shows normalized ( $S/E_p^2$ ) scan data in the 690.80 to 690.90 nm range, which contains rotational transitions with quantum numbers near  $\approx 30$ . The distance from the surface for each measurement location is indicated under the separate images. Looking at the images sequentially starting with the location outside the boundary layer, one can see that the signal reflects that the rotational population of CO is shifting to lower quantum number rotational levels (toward higher wavelength) as the measurements approach the cooled copper surface. This is expected given the translational temperature gradient seen in the oxygen atom measurements. The scans are very noisy, as the filter admitted both LIF signals and visible emission from the plasma at the detection wavelength. To reduce the background signal level, a second boxcar gate was set to record the signal approximately 60 ns after the laser pulse, and so each point of the scan is corrected by subtracting this background signal. This improved the signal relative to the noise, but clearly a better filter is needed for these measurements.

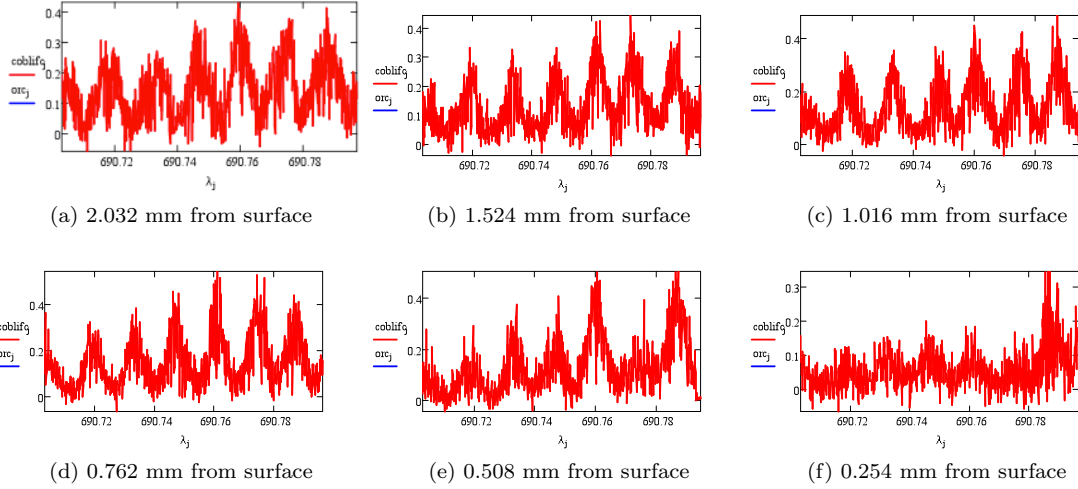


Figure 8: Scans of the CO ( $B \leftarrow X$ ) (0,0) absorption band at varying distances from the surface

Figure 9 shows the CO ( $B^1\Sigma^+ \leftarrow X^1\Sigma^+$ ) (0,0) bandhead at 691 nm. This measurement was obtained with the beam partially blocked by the probe, and so sampled the region adjacent to the copper surface, which is relatively cool. Note that the signal is normalized by the raw energy measurement, which does not account for the sample blockage, and so the signal level is artificially lowered.

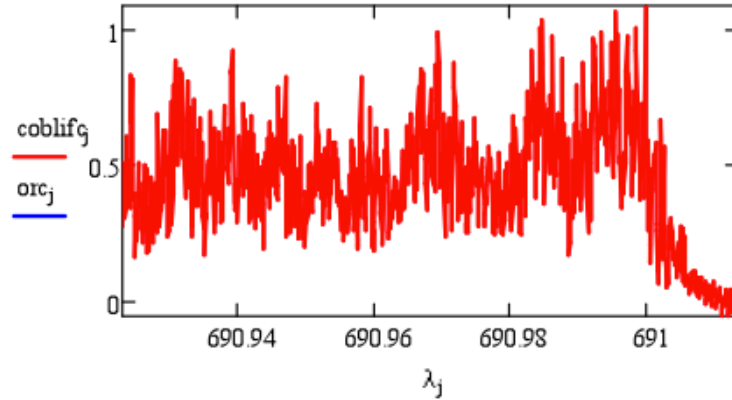


Figure 9: CO ( $B \leftarrow X$ ) (0,0) bandhead, 0.127 mm from surface

Despite the noise in the data, fits were made using a spectral model of the CO  $B \leftarrow X$  absorption including all rotational transitions up to a rotational quantum number of 100. The spectroscopic constants for this model were taken from Huber and Herzberg<sup>14</sup> for the  $X^1\Sigma^+$  state and Eidelsberg and Rostas<sup>15</sup> for the  $B^1\Sigma^+$  state. An example fit is shown for the furthest point from the surface in Figure 10. The temperature sensitivity of the fit is limited owing to the relatively short spectral range of the scan. However, even with the difference in mixture, the best fit temperature value appears to be in reasonable agreement with the temperature derived from the oxygen atom line shape analysis, as seen in Figure 11 where fit-derived temperature values are shown for all of the measurement locations. We expect that the uncertainties in these temperature values are on the order of at least 1000 K. A longer wavelength scan range would have helped, but this was not possible given the power supply issues.

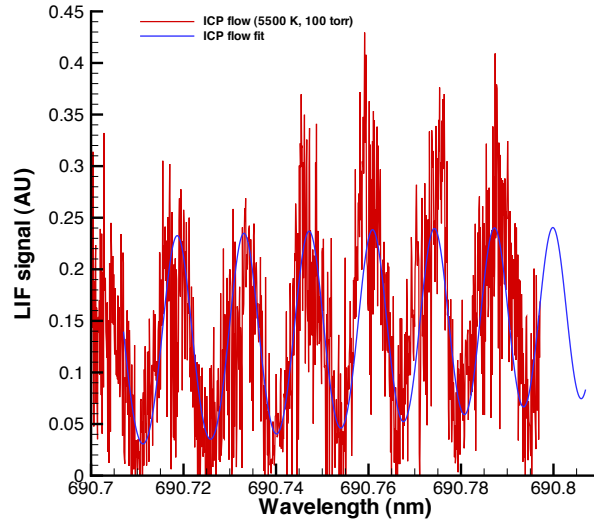


Figure 10: Spectral model fits to CO absorption for the nearest and furthest points from the surface

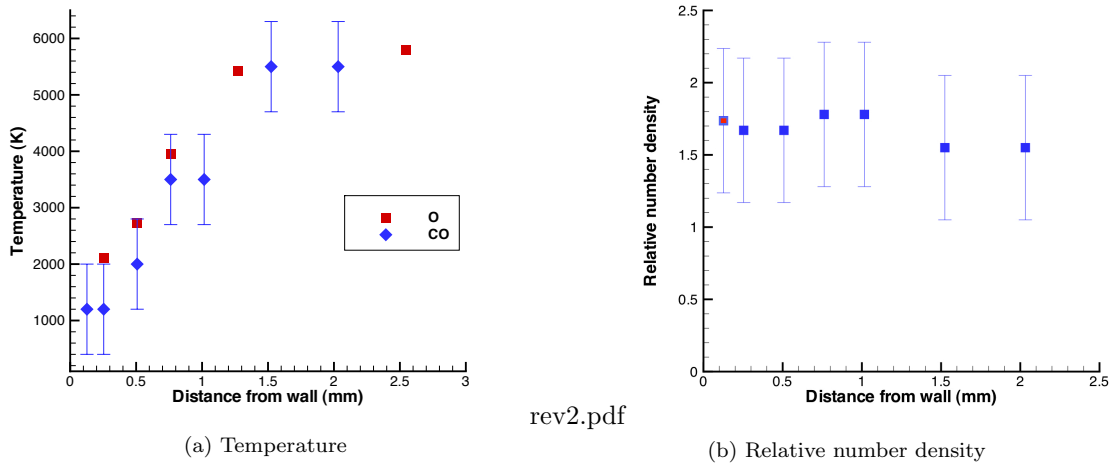


Figure 11: **Temperature and relative number density for CO scans**

A more interesting parameter to evaluate is the relative CO number density, and an estimate of this value for the different measurements was obtained by spectrally integrating the model over all rotational transitions, once the model value was adjusted to the measured voltage at each location. As the bias voltage was constant for all tests and no adjustments were made to the detection system, this integral value is expected to be a reasonable representation of the relative number density. The distribution of these values is shown in Figure 11. Although the data are preliminary and of very low quality as indicated by the large error bars, it is interesting to note that they show a trend of either constant or slightly increasing density (except at the last location on the surface) toward the surface. This trend would be consistent with frozen chemistry, and a low value of surface catalycity for promoting the reaction  $CO + O(s) \rightarrow CO_2$ . As mentioned above, at the location nearest to the surface the laser beam was partially blocked by the edge of the cooled probe. During the measurements, the fourth boxcar channel was used to measure the background signal

with the second gate rather than recording the laser pulse energy passing through the ICP facility. As such the data point was adjusted by an estimate of the unblocked energy based on the known beam profile. Our estimate of the normalized signal loss at this location was  $\approx 56\%$  based on the beam geometry.

## V. Summary

Preliminary measured values of temperature, oxygen atom relative density, and CO relative density obtained in CO<sub>2</sub> and Ar plasmas in the 30 kW ICP Torch Facility were presented and trends in the data were discussed. These data represent a first attempt to assess relative surface-catalyzed reaction probabilities for the different possible surface reactions relevant to Mars atmosphere missions by direct measurement of species gradients over catalytic and noncatalytic surfaces. Although the data are preliminary the trends suggest that O atom recombination does occur at the surface. In the case of CO, where the data are of exceptionally low quality, the current trend in the relative densities determined from spectral fits (over a limited spectral range) does not support strong CO participation in surface-catalyzed recombination reactions.

Future tests will address the issues of facility noise and extended operation on CO<sub>2</sub> mixtures, while improved filters for CO LIF will be investigated. As many of the ancillary measurements required to extract absolute number densities from LIF signals have been done, further effort will be made to convert the data to absolute values, and to check for consistency with other data at the boundary layer edge.

## VI. Acknowledgements

This work has been supported by NASA Grant NNX08AD01A and AFOSR Grant FA9550-08-1-0414.

## References

- <sup>1</sup>Sepka, S., Chen, Y.-K., Marschall, J., and Copeland, R.A., Experimental Investigation of Surface Reactions in Carbon Monoxide and Oxygen Mixtures, *Journal of Thermophysics and Heat Transfer*, Vol. 14, 2000, pp. 45-52
- <sup>2</sup>Marschall, J., Copeland, R.A., Hwang, H.H., and Wright, M.J., Surface Catalysis Experiments on Metal Surfaces in Oxygen and Carbon Monoxide Mixtures, AIAA Paper 2006-181, January 2006.
- <sup>3</sup>Wright, M.J., Olejniczak, J., Brown, J.L., Hornung, H., and Edquist, K.T., Modeling of Shock Tunnel Aeroheating Data on the Mars Science Laboratory Aeroshell, *Journal of Thermophysics and Heat Transfer* Vol. 20, No. 4, 2006, pp. 641-651
- <sup>4</sup>Bose, D., Wright, M. J., Palmer, G. E., (2006) Uncertainty Analysis for Laminar Aeroheating Predictions for Mars Entries *Journal of Thermophysics and Heat Transfer* vol. 20 no. 4 652-662
- <sup>5</sup>Wright, M.J., Edquist, K.T., Hollis, B.R., Brown, J.L., Olejniczak, J. (2007) A Review of Aerothermal Modeling for Current and Future Mars Entry Missions *Journal of Thermophysics and Heat Transfer*
- <sup>6</sup>Barbante, P.F., (2009) Heat Flux Duplication Between Ground Facility and Flight *Journal of Thermophysics and Heat Transfer* 684-692
- <sup>7</sup>Magin, T. (2004) A Model for Inductive Plasma Wind Tunnels
- <sup>8</sup>Wright, M. J., Grinstead, J. H., Bose, D. (2007) A Risk Based Approach for Aerothermal/TPS Analysis and Testing *Experiment, Modeling and Simulation of Gas-Surface Interactions for Reactive Flows in Hypersonic Flights*
- <sup>9</sup>Owens, W. P., Uhl, J., Dougherty, M., Lutz, A., Fletcher, D. G., (2010) Development of a 30 kW Inductively Coupled Plasma Torch Facility for Aerospace Material Testing
- <sup>10</sup>Meyers, J., Owens, W.P., Dougherty, M., Lutz, A., Fletcher, D.G., "Laser Spectroscopic Investigation of Surface-Catalyzed Reactions for Mars Exploration Vehicles" Paper presented AIAA Thermophysics and Heat Transfer Conference,, Chicago, Illinois, 2010
- <sup>11</sup>Fletcher, D.G. and Playez, M., (2006) Characterization of Supersonic and Subsonic Plasma Flows, AIAA Paper No. 2006-3294, June
- <sup>12</sup>Bischel, W.K., Bamford, D.J. and Jusinski, L.E. (1986) Absolute Calibration of a Fluorescence Collection System by Raman Scattering of H<sub>2</sub>, *Applied Optics*, Vol 25, pp. 1215-1221.
- <sup>13</sup>Fletcher, D. G., Thoemel, J., Chazot, O., and Marschall, J.,(2010) Realization of a Gas-Surface Interaction Test Case for Model Validation, AIAA Paper No. 2010-1249, Jan
- <sup>14</sup>Huber, K.P. and Herzberg, G. *Molecular Spectra and Molecular Structure IV: Constants of Diatomic Molecules*, Van Nostrand Reinhold, New York, 1979
- <sup>15</sup>Eidelsberg, M. and Rostas, F., Spectroscopic, Absorption, and Photodissociation Data for CO and Isotopic Species Between 91 and 115 nm, *Astronomy and Astrophysics*, Vol 235, No 1-2, pp 427-489, 1990

# INVESTIGATION OF CN PRODUCTION FROM CARBON MATERIALS IN NITROGEN PLASMAS

A. Lutz\*, W. Owens†, J. Meyers‡ and D.G. Fletcher§

*University of Vermont  
Burlington, VT  
and*

**J. Marschall\*\***

*SRI International  
Menlo Park, CA*

The numerical approaches used to calculate ablative heat shield thickness have come into question recently, with particular attention given to uncertainties in chemical reaction rates. One such example is the carbon nitridation reaction,  $C(s) + N \rightarrow CN$  where atomic nitrogen extracts solid carbon from a heat shield surface. Few measurements have been performed for this reaction at conditions relevant to re-entry, and large differences exist in reported values. Experiments aimed at measuring this particular reaction rate have been conducted recently in the 30 kW Inductively Coupled Plasma Torch Facility at the University of Vermont, which simulates re-entry conditions on scaled material samples. Two-photon laser-induced fluorescence is used to measure nitrogen atom density and translational temperature in the reacting boundary layer above the graphite surface. These measurements are used to calculate the nitrogen atom flux reaching the surface. Combining this result with measurements of sample mass loss allows an estimation of the nitridation rate for the test conditions. Initial tests were done with modest surface temperatures in the range of 1620 to 1800 K. Preliminary results from this investigation are reported.

## 1. INTRODUCTION

Planetary exploration and Earth re-entry vehicles experience extremely high convective and radiative heat loads during hypersonic flight, especially in stagnation regions. Accurate prediction of these heat flux levels remains a key objective in the development of next-generation space-exploration vehicles. At present, thermal protection systems (TPS) are designed with large safety factors owing to the limited understanding of gas-surface interactions at elevated temperatures. This conservative design approach adds mass to the TPS at the expense of vehicle payload and presents a barrier to the deployment of novel TPS designs that may provide better performance with lower mass penalty. Clearly, detailed studies of gas-surface interactions are needed to improve this situation.

Heat shields are typically classified as either ablative or non-ablative TPS depending on their composition. Figure 1 below shows the processes that occur for both ablative and non-ablative materials at high

---

\*Graduate Student, Mechanical Engineering Department, 211 Perkins Hall, 33 Colchester Ave; andrew.lutz@uvm.edu.

†Graduate Student, Mechanical Engineering Department, 211 Perkins Hall, 33 Colchester Ave; wpowens@uvm.edu.

‡Post-doctoral Researcher, Mechanical Engineering Department, 109 Votey Hall, 33 Colchester Ave, Member AIAA.

§Professor, Mechanical Engineering Department, 201 Votey Hall, 33 Colchester Ave; douglas.fletcher@uvm.edu. Associate Fellow AIAA.

\*\*Senior Research Scientist, Molecular Physics Laboratory, 333 Ravenswood Avenue; jochen.marschall@sri.com. Senior Member AIAA.

temperatures. Non-ablative materials are restricted to aerothermal trajectories where the vehicle does not encounter heat fluxes that drive the material beyond its melting point. Ablative materials are designed differently as they allow for a controlled burn of a low-temperature phase-change material impregnated within a stronger, matrix material to provide blockage of the convective heating; thus mitigating heating by phase change and mass efflux. For ablative TPS, carbon has proven to be the most performant matrix material.

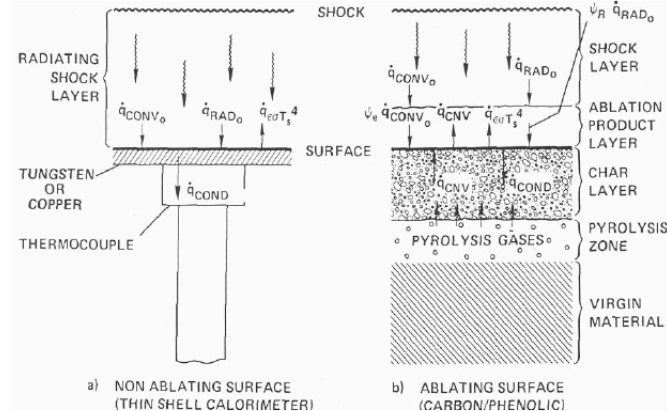


FIGURE 1. Diagram summarizing heat and mass transfer processes with ablating and non-ablating heat shields.

A key aspect of ablative TPS is understanding all carbon based reactions, including carbon nitridation, which may play an important role in high-speed earth re-entry missions, such as outer planet sample return. This reaction is known to result in formation of the cyanogen (CN) molecule, which is a very strong radiator at high temperatures. Despite the role of nitridation in the ablation of carbon based heat shields, a reliable gas-surface CN reaction efficiency has not been measured. Historically, surface recession rates have been calculated through B' tables, which assume a chemical equilibrium model. However, evidence of chemical non-equilibrium between the surface and ambient gas has been proven, making finite-rate chemistry models necessary [1].

Previous experiments have attempted to measure the carbon nitridation reaction efficiency. One of the first attempts to classify this efficiency was performed by Goldstein [2]. AGOT and TSX graphite samples were exposed to a stream of microwave-discharge generated nitrogen and liquid-nitrogen cooled traps were used to gather byproducts. CN production was measured relative to the approaching N-atom concentration. Reaction efficiency was found to vary between 0.00041 to 0.0017 over a temperature range of 1694K to 2365K in TSX graphite. With AGOT samples, the efficiency range varied between 0.00045 and 0.00069 within 2031K and 2237K respectively. There is some uncertainty regarding the accuracy of these findings, however the data do not seem unreasonable.

One of the more surprising results was obtained by Park and Bogdanoff [4]. In their experiment, tungsten wire coated in lampblack was subjected to a stream of highly dissociated nitrogen, produced within a shock tube. The N-atom concentrations were calculated assuming post-shock equilibrium conditions and the CN production was inferred from spectrally integrated emission at 386 nm. The authors determined a reaction efficiency of  $\gamma_N = 0.3$  from this experiment. This value is higher than expected and it does not have a temperature dependence, which is physically unlikely [1]. In contrast, carbon oxidation has a strong dependence on temperature, where  $\gamma_O$  is known to vary between 0.01 and 0.3 for room temperature and

3000 K, respectively. Also, carbon oxidation should be a more efficient than nitridation, but the Park and Bogdanoff result does not reflect this.

Recently, Suzuki et. al utilized a 110 kW Inductively Coupled Plasma (ICP) wind tunnel to study CN production in a stream of pure nitrogen [3]. The experiments were performed at a pressure of 10 kPa and a mass flow rate of  $2 \text{ g s}^{-1}$ . These experiments yielded reaction efficiencies ranging from 0.0025 and 0.0032 at surface temperatures of 1822K to 2184K respectively. These numbers appear to agree in magnitude with the Goldstein experiments. No direct measurements of N-atom were made for these tests. Instead a computational fluid dynamics code was used to estimate N-atom concentration.

For graphite, enhanced oxidation efficiency with respect to nitridation is easily proven. A sample placed in an air plasma will show signs of oxidation, including significant surface recession for high heating rate conditions within a few minutes. A similar sample will not show signs of deformation until much later at identical conditions in a pure nitrogen plasma. This is illustrated in Figure 2 where several samples were subjected to different plasma streams at varying exposure times. The sample exposed to nitrogen was held within the stream on the order of 10 minutes. It appears unchanged from the virgin sample whereas samples exposed to air plasmas for equivalent or shorter durations show significant surface erosion.



FIGURE 2. Graphite samples used in the UVM ICPT test facility. These samples show the different stages of decomposition from 1) nitrogen plasma (10 min) 2-3) air-argon plasma in successively longer exposure times up to 10 minutes [5].

To provide a better measure of nitridation, and thereby resolve some of the existing discrepancies a series of experiments are being conducted at SRI International using a high temperature diffusion reactor and at the University of Vermont (UVM) in the 30 kW (ICP) Torch Facility. Results from the diffusion reactor tests have been reported [1], and the results appear to be consistent with those of Goldstein and Suzuki. The present paper reports on the status of the measurements in the ICP Torch Facility.

In the present investigation, numerical simulations of the ICP stagnation point boundary layer conditions are used to estimate the boundary layer thickness and property gradients to help define the required spatial resolution for LIF measurements. These simulations are described in the next section, and this is followed by descriptions of the ICP facility and laser diagnostic approach used for these investigations. Finally, results are presented and discussed and a summary is given.

## 2. BOUNDARY LAYER CODE

Several numerical codes have been developed at the von Karman Institute (VKI) in Belgium for modeling stagnation point testing in ICP facilities. The Non-Equilibrium Boundary Layer (NEBOULA) flow code is a computational tool that calculates surface heat flux for different boundary edge conditions at the stagnation point in user-defined gas mixtures [6]. Output from NEBOULA includes temperature, density,

velocity, enthalpy and mass and molar fractions of species along the stagnation stream line. The sample body diameter determines the velocity gradient around the body. NEBOULA requires plasma mixture properties, including transport, chemical and thermodynamic properties at various conditions within the reacting boundary layer. The Multicomponent Transport, Thermodynamic and Chemistry Properties for Ionized Gases (MUTATION) library calculates gas mixture properties at prescribed temperatures and pressures [7], providing an accurate description of the behavior of gases at plasma conditions. For the present investigation of carbon nitridation, MUTATION and NEBOULA are used as an aid in the interpretation of experimental results.

Figure 3a shows the mass fraction of a 5-species  $N_2$  mixture as a function of temperature over the range of 1500 to 7000K for a static pressure of 115 Torr. These conditions closely correspond to the experimental test conditions in the 30 kW ICP Torch Facility, and show clearly that  $N_2$  dissociation will be significant at temperatures above 5000 K. These calculations are done for thermodynamic equilibrium, which is believed to pertain to the boundary layer edge conditions. Investigation of the boundary layer edge condition for the present experiments is ongoing. These data, along with enthalpy, mass density and viscosity serve as initial conditions for the NEBOULA stagnation-point calculation.

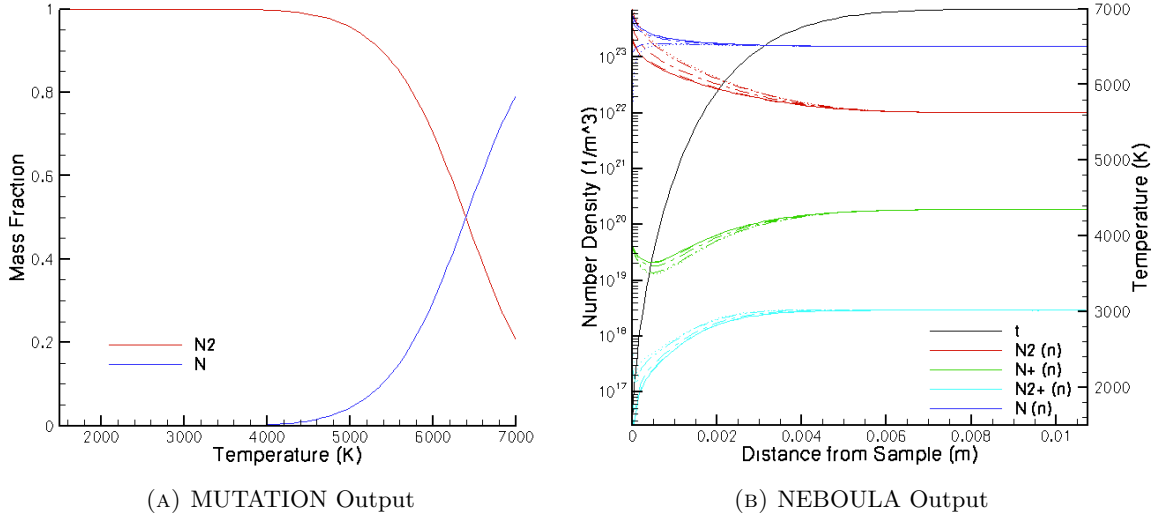


FIGURE 3. a. Mass fraction of the 5-species  $N_2$  mixture created in MUTATION as a function of temperature. The primary species present are  $N_2$  and atomic Nitrogen. All other species do not appear in large quantities at these conditions. b. Molar composition and mixture temperature of the 5-species  $N_2$  gas created in NEBOULA. Prominent species include  $N_2$  and  $N$ .

Figure 3b shows a sample output from the NEBOULA code. Species number densities and the bulk gas temperature are plotted along the stagnation point streamline. The boundary layer edge and wall temperatures were set to 7000K and 1500K respectively for this particular case. Again, the prominent species for these conditions are molecular and atomic nitrogen. Three traces are shown for each species, corresponding to non-catalytic (solid), fully catalytic (dotted) and partially catalytic (dot-dash). Surface catalysis in this case is used as a qualitative indicator of nitridation, as both represent mechanisms for removing atomic nitrogen from the boundary layer, which affects the nitrogen atom density gradient. An increasing N-atom density gradient towards the surface would indicate infinitely slow nitridation, while a decreasing N-atom density gradient indicates a higher nitridation rate.

## 3. FACILITY AND INSTRUMENTATION DESCRIPTION

The 30 kW ICP Torch Facility at UVM is designed to test samples in high enthalpy gas flows for simulation of planetary entry and earth atmosphere re-entry trajectory heating conditions. It is currently configured for operation with subsonic flow to simulate the post-shock conditions of high-enthalpy flight for a stagnation point geometry. As described in [8], the facility test conditions can be related to flight trajectory conditions (or to supersonic arc-jet facility test conditions) through the similarity parameters that control stagnation point heating: total flow enthalpy, stagnation pressure, and stagnation-point velocity gradient. A key advantage of ICP facilities is their electrode-less operation and their ability to operate on a wide range of gas mixtures. The design specifications for the UVM 30 kW ICP Torch Facility are summarized in Table 1.

TABLE 1. UVM ICPT System Specifications [5]

Parameter	Rating
Inductive heater power	30 kW (max) @ 4 MHz
Enthalpy range	10 - 40 MJ kg <sup>-1</sup> (for air)
Mach range	0.3 to 1
Stagnation heat transfer rate	10 - 290 W cm <sup>-2</sup>
Stagnation pressure	0.05 - 1.0 atm

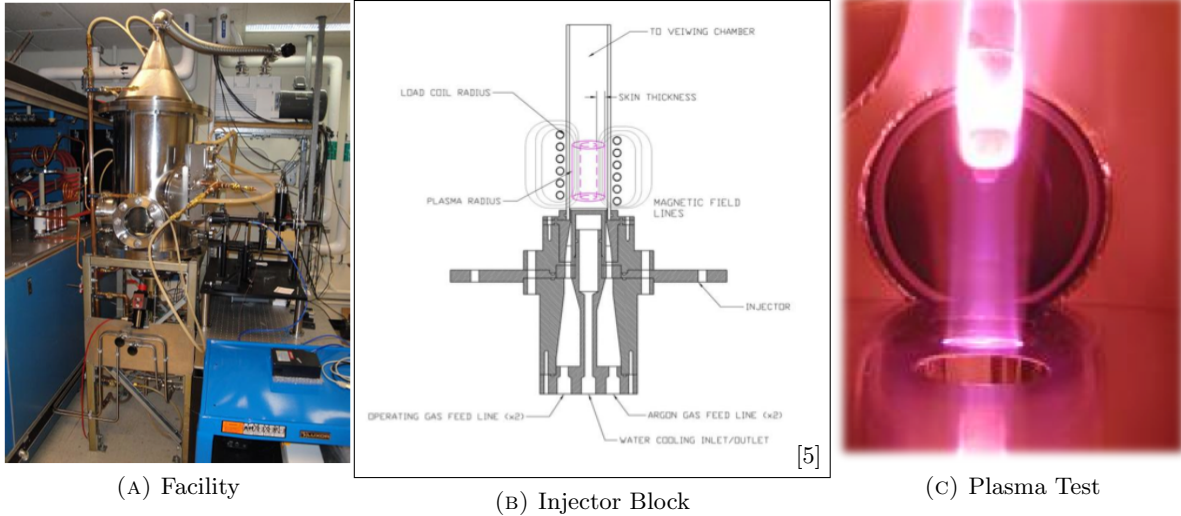


FIGURE 4. a. The University of Vermont ICPT test chamber and 30kW power source. b. The gas injector block assembly is located below the test chamber and is responsible for injecting steady, laminar gas flow through the quartz tube [5]. c. Experimental setup with graphite sample face held perpendicular to major flow axis. Sample shown tested in nitrogen plasma.

The primary components of the ICP facilities are the power source, gas injection assembly, test chamber, cooling circuit, vacuum pump and gas supply system. The power supply, test chamber and vacuum pump



tripling, provided tunable UV radiation over a wavelength range of 205 to 220 nm. Downstream of the crystals, the UV output beam is divided in two directions; 90% of the beam power is directed toward the test chamber and 10% is sent to the Microwave-Discharge Flow Reactor (MDFR). As discussed below, additional energy is removed from the ICP leg by two additional beam splitters to maintain the laser pulse energy density at the ICP measurement location at modest levels. This avoids stimulating additional multi-photon processes that would interfere with the two-photon Laser-Induced Fluorescence (LIF) signals. Fluorescence from both the ICP and MDFR is detected using gated PMTs with 10 nm bandpass filters centered at 870 nm. A tilting stage was used to angle the PMT view at the ICP such that signal obscuration by the sample is avoided. A Molectron energy meter downstream of the flow reactor is used to normalize the measured LIF signals for the laser pulse energy fluctuations. All signals are averaged and recorded using a gated integrator system. Typical laser system pulse energies at the different wavelengths are summarized in Table 2.

The target species for two-photon LIF measurements in the present investigation is atomic nitrogen, as its flux arriving at the surface is presumed to be the parameter controlling active surface nitridation. By making simultaneous measurements of an absorption transition in both the ICP Torch Facility and in the MDFR, absolute concentrations of nitrogen atoms can be determined based on the known concentration in the flow reactor, which are established by chemical titration, as described by Fletcher and Playez [8]. Briefly, the measurements involve performing Raman calibrations of the detection optics for both locations, as well as measuring the respective fluorescence yields, beam spatial and temporal profiles, and energies.

TABLE 2. Nd:YAG Laser Specifications

Parameter	Rating
YAG pulse energy	740 mJ @ 532 nm
Dye fundamental output	120 mJ @ 633 nm
Tripled output	3-4 mJ @ 211 nm (N-atom LIF)
Temporal pulse width	7 ns

#### 4. EXPERIMENTAL APPROACH

Two-photon LIF will be used to obtain quantitative measurements of nitrogen atom densities in the reacting boundary layer over graphite samples placed in the nitrogen plasma stream to allow a determination of the nitridation reaction efficiency. For the present investigation, we assume that nitridation arises directly from atomic nitrogen reaching the surface and combining with a surface carbon atom, so the reaction efficiency,  $\gamma_N$ , is calculated from the following equation [1].

$$\gamma_N = \frac{\Gamma_{CN}}{\Gamma_N} = \left( \frac{\Delta M_C}{A m_C \Delta t} \right) / \left( \frac{n_N}{4} \sqrt{\frac{8 k_B T}{\pi m_N}} \right)$$

The reaction rate efficiency is the ratio of the CN flux,  $\Gamma_{CN}$ , to the nitrogen atom flux,  $\Gamma_N$ , which are the rates of CN creation and N-atom flow to the surface, respectively. This ratio can be expressed as a function of the sample carbon mass loss  $\Delta M_C$ , the sample area  $A$ , the atomic masses of carbon and nitrogen  $m_C$  and  $m_N$ , the exposure time  $\Delta t$ , the nitrogen atom number density  $n_N$ , the Boltzmann constant  $k_B$  and temperature  $T$ . Of these parameters, the only values that need to be measured experimentally are the carbon mass loss, sample area, exposure time, temperature and nitrogen atom number density just above the sample surface.

The sample area is measured directly from the initial geometry, and for these first tests the change in area due to plasma exposure is assumed to be negligible. All samples used have a 20 mm nominal diameter and a 12.5 mm height. The carbon mass loss is calculated from pre- and post-test mass measurements. Care was taken to avoid inadvertent contamination of the graphite surface by handling with gloves only after a methanol rinse. Exposure times for the graphite samples in nitrogen plasmas were recorded from the time that the target test conditions were achieved. Owing to the sample geometry used for these tests,

the samples were always in the plasma, even during startup. However, the starting conditions in argon have very low heat flux levels, and we expect that exposure to the argon plasma did not affect the surface. Two-photon LIF is used to make spatially resolved measurements of translation temperature and nitrogen atom number density.

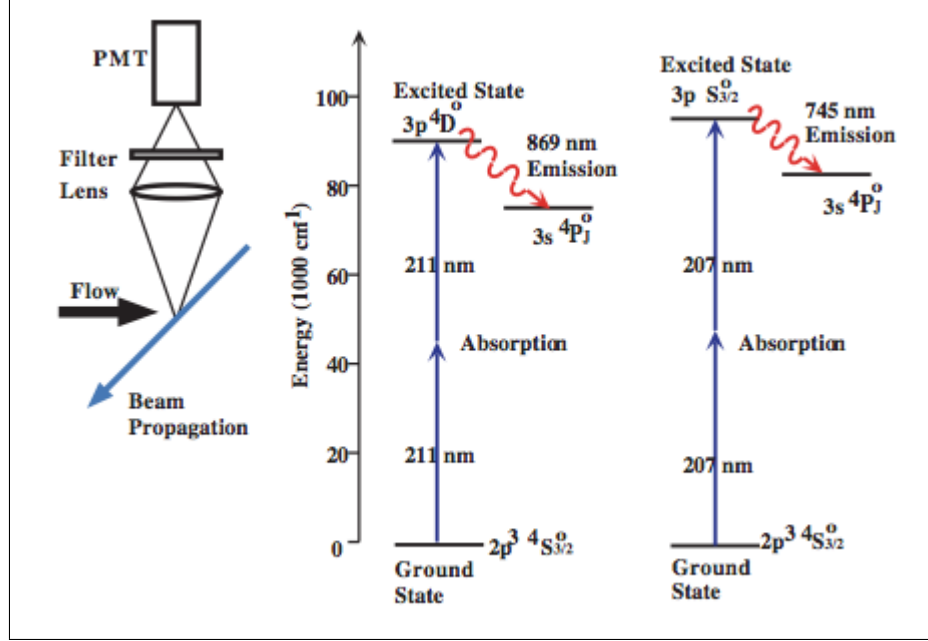


FIGURE 6. Two-photon nitrogen excitation strategies.

Two-photon LIF measurements of atomic nitrogen have been described in detail elsewhere [8]. There are two excitation strategies that can be used, and these are shown in Figure 6. Owing to use of DCM dye, higher pulse energies are available for the longer wavelength excitation (211 nm), and so this approach is used for the present investigation, despite the fact that the fluorescence is polarized. As mentioned above, the output of the dye laser is frequency tripled to the 211 nm wavelength region. Note that both nitrogen number density and translational temperature are needed to quantify the nitrogen atom flux rate, and so the measurements were made by scanning the dye laser wavelength over the atomic transition. As shown on the figure, the scan will promote atoms from the  $2p^3 \ 4S_{3/2}^o$  state to the  $3p^4 D^o$  state and the excited atoms where they can then relax to the  $3s^4 P_J^o$  by emitting a photon at 869 nm. Translation temperature is then determined from a spectral fit of the fluorescence for both the reactor and ICP data. As the flow reactor conditions are at room temperature, the fit is used to determine the laser line-width, which is then used in the fit of the ICP LIF line shape to extract a temperature from the plasma measurement. The current spectral model assumes negligible collisional broadening, and so is based on the convolution of the gaussian laser frequency distribution and the thermal distribution of absorbing atom velocities. Figure 7 shows a plot of the 2-photon LIF signal for atomic nitrogen in the UVM ICP torch facility free-stream, as well as a simultaneous signal recorded in the flow reactor from a recent test. The fits obtained from the spectral model of the line shape are also shown for each spectrum.

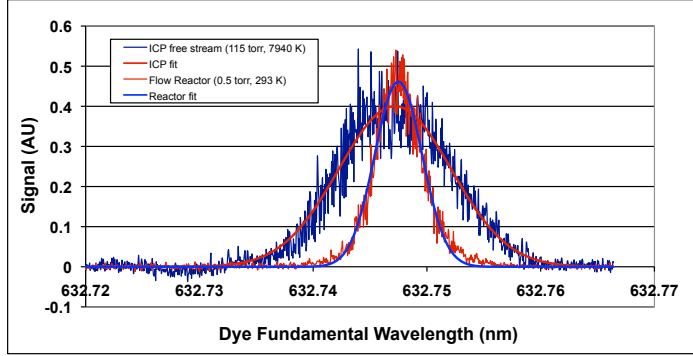


FIGURE 7. Two-photon LIF measurements within the UVM ICP chamber and flow reactor.

The spectrally integrated fluorescence signal is proportional to the local number density of atomic nitrogen. However, to convert the values measured in the ICP to absolute number densities requires measurement of additional parameters, as well as a chemical titration to establish the number density in the flow reactor. The explicit relationship for number density is

$$(n_N)_{icp} = \frac{\int (S/E^2)_{icp} d\omega D_{fr} \tau_{fr} w_{icp}^2}{\int (S/E^2)_{fr} d\omega D_{icp} \tau_{icp} w_{fr}^2} (n_N)_{fr} \quad ,$$

where  $S$  is the fluorescence signal,  $E$  is the pulse energy,  $D$  is the Raman calibration factor,  $\tau$  is the observed fluorescence lifetime,  $w$  is the beam waist at the measurement locations, and the subscripts refer to ICP and flow reactor, respectively. Measurements of all parameters needed for conversion of relative densities to absolute values have been obtained and examples are shown below and discussed briefly.

Several measurements of the observed fluorescence lifetime are taken during the ICP tests for both the ICP and flow reactor LIF, and the lifetime is determined from a single exponential fit to the measurements. An example ICP measurement is shown in Figure 8 below, where the influence of quenching at the higher pressure in the ICP is evident. The lifetime derived from the fit is 6.2 ns, which is considerably shorter than the  $\approx 32$  ns radiative lifetime.

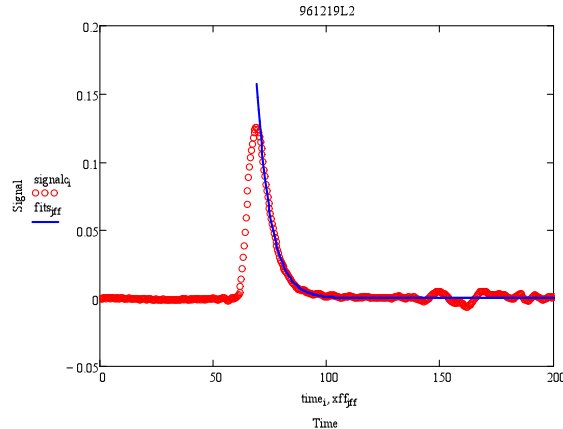


FIGURE 8. Observed fluorescence lifetime for ICP

A Spiricon beam profiler is used to record images of the laser energy distribution at each measurement location when the facility is not running, and the waist values are extracted from these images. One example beam image is shown below in Figure 9a for the focal region in the ICP. At this location, the beam is not perfectly circular, but the narrowest dimension is aligned along the direction perpendicular to the surface, which provides a spatial resolution of about 0.4 mm in this direction. As the beam is tightly focused, periodic evaluations of the energy density at the measurement locations are done by recording PMT and energy meter signals as the polarization rotator between the doubling and tripling crystals is adjusted. If the power-law fit to the data gives a slope close to two, then the correct two-photon scaling is assumed to apply for the experiment. Results from these tests led us to reduce the energy brought to the ICP flow by installing two additional beam splitters and shifting the focal position of the lens, as discussed below. Following this six-fold reduction in laser energy density in the focal region, the LIF signal scaled very nearly with the square of the pulse energy, as shown below in Figure 9b.

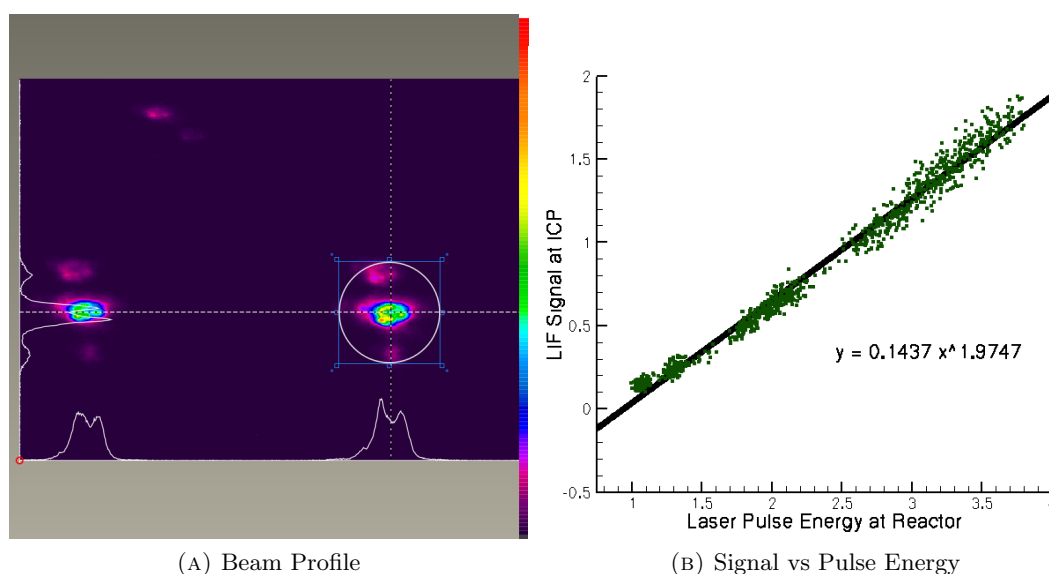


FIGURE 9. a. Beam profile measured at the ICP detection region. b. ICP LIF signal plotted against laser pulse energy (exponent from power law fit is 1.97, compared to theoretical value of 2.)

Raman calibrations have also been done for both the ICP and flow reactor detection instrumentation. Unfortunately, the mass flow controller that is used to monitor the titration gas is currently being repaired, and so we have to postpone the conversion of the relative number density values to absolute values. The titration of the nitrogen atoms by the fast reaction  $N + NO \rightarrow N_2 + O$  is described in [8].

The graphite sample test procedure involved aligning the sample in the center of the plasma with the facility not running and registering the laser beam stage micrometer and PMT stage micrometer to the cold sample leading surface location. The facility is then closed and evacuated, and the plasma is initiated with argon. After pressure is raised to the target level, nitrogen is added and argon is removed until full nitrogen plasma flow is established. Moving away from the sample in small steps, laser wavelength scans are performed at each measurement location, and pressure and mass flow are maintained at constant levels. If time allows, some measurements are repeated to judge how steady conditions are maintained.

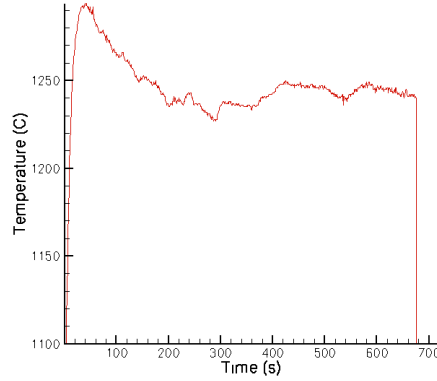


FIGURE 10. Surface temperature of graphite sample 4 in nitrogen plasma mixture.

As mentioned above, the sample surface temperature was also recorded during the tests, and Figure 10 shows an example of such a measurement for graphite in a nitrogen/argon plasma stream for the test of sample 4. The trend shown is typical for most experiments: surface temperature rises to a maximum level and then decreases. This is believed to be a result of heat transfer by conduction through the sample to the water-cooled probe holder, which is in contact with the sample stem. The surface temperature decreases when the the cooling water begins to flash boil, which provides a considerable heat-sink for the highly conductive graphite. Future tests will incorporate a zirconia based insulator to reduce the conductive loss.

## 5. RESULTS AND DISCUSSION

Seven identical 20 mm diameter graphite samples were tested during this campaign, and the mass loss and test duration data for these samples are given in Table 3 below, along with the respective mass loss rates. Note that for these preliminary measurements, changes were being made to both the tank circuit of the power supply, injector block, and sample holder. Thus, the wide variation in mass loss rates for similar surface temperature values is not surprising. However, for samples 6 and 7, where boundary layer data were acquired during the tests, the configuration of power supply, injector block and sample holder were unchanged. Sample pre- and post-test dimension measurements to evaluate surface recession are given in Table 4.

TABLE 3. Test Sample Mass Measurements

Sample #	Mass <sub>0</sub> (g)	Mass <sub>f</sub> (g)	ΔMass (g)	Total Run Time (mm:ss)	Mass Loss Rate (mg/s)	Average Wall Temperature (K)
1	7.833	7.116	0.717	15:10	.788	1380
2	7.838	6.125	1.713	33:10	.861	
3	7.839	6.351	1.488	40:40	.610	
4	7.86	7.226	0.634	58:20	.181	1243
5	7.825	6.572	1.253	30:00	.696	1304
6	7.857	6.994	0.863	34:55	.412	1427
7	7.831	6.57	1.261	63:20	.332	1318

TABLE 4. Test Sample Recession Measurements

Sample #	Length <sub>0</sub> (mm)	Length <sub>f</sub> (mm)	$\Delta$ Length (mm)	Diameter <sub>0</sub> (mm)	Diameter <sub>f</sub> (mm)	$\Delta$ Diameter (mm)	Total
							Run Time (mm:ss)
1	7.833	7.116	0.717	19	18.5	0.5	15:10
2	7.838	6.125	1.713	19	18	1	33:10
3	7.839	6.351	1.488	19	18	1	40:40
4	7.86	7.226	0.634	19	18.5	0.5	58:20
5	7.825	6.572	1.253	19	19	0	30:00
6	7.857	6.994	0.863	19	18.5	0.5	34:55
7	7.831	6.57	1.261	19	18	1	63:20



FIGURE 11. Sample 2 after a long duration, high temperature run alongside a virgin sample, showing how a sample changes in length and profile dimensions during nitridation.

As expected, the greatest amount of mass loss came from the shortening of the sample. However, there was also an effect on the profile as well. With high temperature conditions and a long exposure time, the diameter changed significantly, as shown in Table 4. Figure 11 shows sample 2 post-run alongside a virgin sample. This illustrates how the perimeter evolves from a cylindrical shape to a tapered profile, which suggests an enhanced heat transfer rate at the sample corner region.

Although boundary layer measurements of nitrogen atom number density and temperature were attempted for each of the sample tests, reliable results were obtained for just two samples (samples 6 and 7). The translational temperature distribution is shown as a function of distance from the surface in Figure 12a below and the corresponding relative nitrogen atom density is shown in 12b. The outer flow temperatures for this test are not reliable, owing to having too high an energy density in the focal volume (this was checked after and the intensity was reduced by a factor of  $\approx 6$  for subsequent experiments). Based on tests performed the next day in the plasma stream, we estimate that the temperature values beyond 1 mm are about 1500 K too high owing to some undetermined multi-photon process interfering with the

two-photon LIF. Nevertheless, the spatial resolution of the LIF measurements appears to be sufficient to capture the gradient region, indicating a boundary layer thickness between 1 and 1.5 mm. Moreover, the approach appears to have a spatial resolution sufficient to allow a determination of the nitrogen atom flux based on an extrapolation of the temperature and number density data to a position just above the surface. Although the nitrogen atom density decreases toward the surface, the signal persistence indicates that non-equilibrium density levels exist for the gas phase near the surface (see Figure 3a). The downward trend is driven by consumption of nitrogen atoms combining with surface carbon. If this reaction did not occur, the relative nitrogen density would likely follow the overall density, given the relatively slow three body recombination reaction. No uncertainty values are indicated on either plot, as these values are still being investigated.

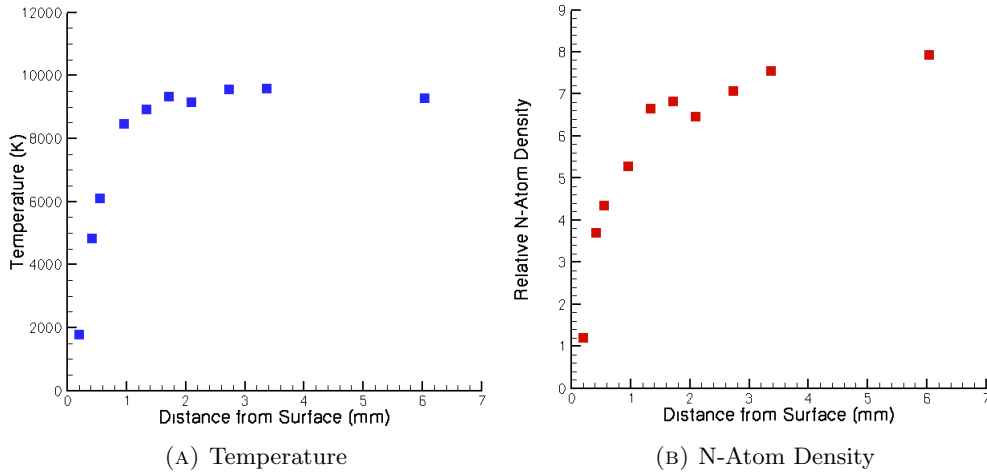


FIGURE 12. Boundary layer survey for sample 6, showing translation temperature and relative nitrogen atom density.

Boundary layer survey results from the test of sample 7 are shown in Figure 13, with the translation temperature in 13a and the relative nitrogen atom density in 13b. All of the translation temperature values shown are believed to be reliable, as the energy in the focal region was brought to a level that gave proper two-photon signal scaling. As with the previous data, we see that the 20 mm diameter sample produces a nearly 1 to 1.5 mm boundary layer thickness that is captured reasonably well by the spatial resolution of the LIF technique. For this case, however, we were not able to obtain measurements as close to the surface as for sample 6, and so the extrapolation for calculating the nitrogen atom flux will likely be less precise.

While every attempt was made to precisely register the beam position with respect to the surface, attaining successful measurements at the appropriate locations was not straightforward. The sample appears to expand slightly when exposed to the hot plasma while the surface recedes during the test. Future measurements will have to account for these effects. We plan to conduct some tests with a laser obscuration measurement to provide information for better alignment.

As mentioned above, the conversion to absolute number densities has not yet been completed, although all of the required ancillary measurements to do so have been completed. However, if we assume that the boundary layer edge conditions are in thermodynamic equilibrium, then we can estimate the nitrogen atom flux based on our measured conditions nearest the surface, and the ratio of relative number densities. This is currently being investigated.

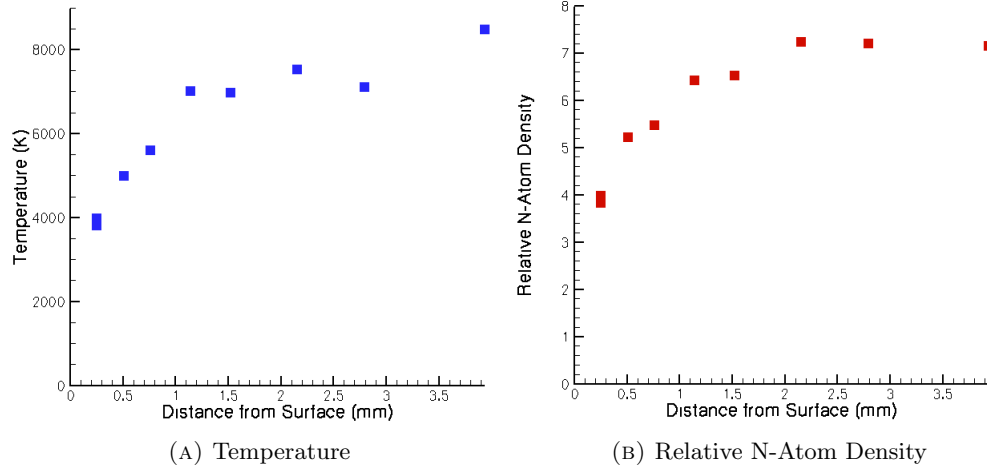


FIGURE 13. Boundary layer survey for sample 7, showing translational temperature and relative nitrogen atom density.)

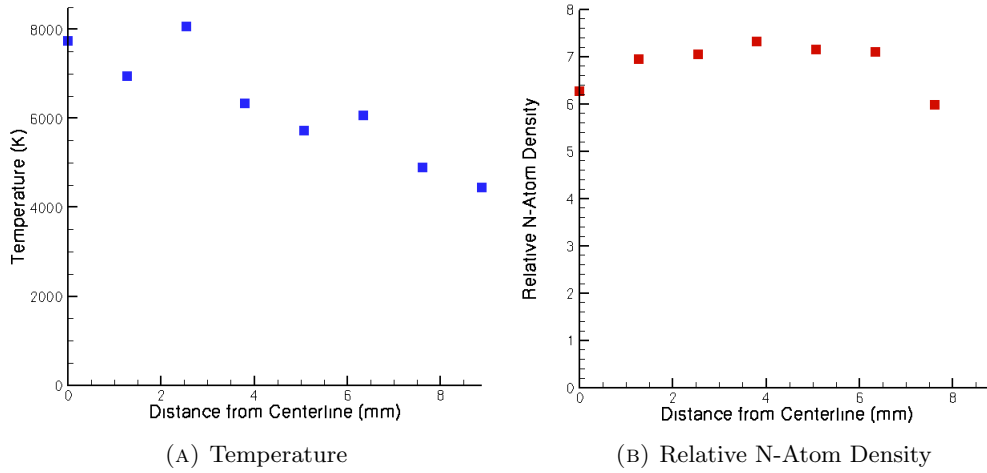


FIGURE 14. Variation in temperature and N atom density in radial direction at a height of 1.52 mm above sample 7 (at boundary layer edge).

Finally, recalling that the laser beam shape is elongated, and noting that the largest dimension is in the radial direction relative to the sample, it is reasonable to question whether or not radial averaging has a significant influence on the results. To assess this, we performed a radial scan at the boundary layer edge with sample 7 in the plasma stream. Radial profiles of translation temperature and relative nitrogen atom density are shown below in Figure 14. The results show modest variation in atom density and temperature.

In the region near the center of the sample there is relatively little variation in nitrogen atom density. Additional radial surveys will be performed closer to the surface in the future to better assess uniformity of the atom flux to the surface.

## 6. SUMMARY

Preliminary results from an investigation of graphite nitridation in an ICP Torch Facility have been presented. The diagnostic approach includes measurements of carbon mass loss along with two-photon LIF measurements of the nitrogen atom flux to the surface for 20 mm graphite samples installed in a nitrogen plasma stream. Boundary layer profiles of translational temperature and nitrogen number density were obtained for two of the seven graphite samples tested. In one case, the boundary layer survey included measurements very near the sample surface, but with questionable outer flow temperature levels owing to excess beam energy density in the focal region. For the second case, following adjustments to the energy density, reliable temperature values were obtained for the entire survey, but the survey did not include a measurements as near to the surface as desired. Nevertheless, these preliminary results clearly indicate that the approach can provide species density and temperature measurements that are sufficiently well resolved to allow a calculation of the atom flux reaching the surface. Based on the carbon loss rate and nitrogen atom arrival flux, the nitridation efficiency can be determined, once the chemical titration of the flow reactor atom population is performed and the measured relative density values are converted to absolute densities.

Further work to complete the nitridation efficiency determination and to quantify the uncertainties in the measurements is ongoing. Additional samples, with a 25 mm diameter to increase the boundary layer thickness, are available for further measurements, and the test range will be extended to include higher surface temperature levels, which will be aided by use of an insulator to reduce the conductive heat loss. Efforts will also be made to take the initial sample surface expansion and subsequent recession into account during the boundary layer survey.

The approach used to assess nitridation is an example of the type of *in situ* measurements that need to be performed in plasma test facilities to provide a better understanding of gas-surface interactions in general.

## 7. ACKNOWLEDGEMENTS

This work was supported by NASA Grant NNX08AC98A and AFOSR Grant FA9550-08-1-0414.

## REFERENCES

- [1] D.A. Pejakovic, J. Marschall, L. Duan and M.P. Martin (2008) Nitric Oxide Production from Surface Recombination of Oxygen and Nitrogen Atoms *Journal of Thermophysics and Heat Transfer*, vol. 22 no. 2 10.2514/1.33073
- [2] Goldstein, H.W., "The Reaction of Active Nitrogen with Graphite," *Journal of Physical Chemistry*, Vol. 68, 1964, pp. 39-42.
- [3] T. Suzuki, K. Fujita, K. Ando, and T. Sakai, "Experimental Study of Graphite Ablation in Nitrogen Flow," *J. Thermo. Heat Trans.*, **22** [3] 382-89 (2008).
- [4] C. Park and D. Bogdanoff (2006) Shock-Tube Measurement of Nitridation Coefficient of Solid Carbon *J. Thermophysics and Heat Transfer*, vol 20, no. 3, pp. 487-492
- [5] W.P Owens, J. Uhl, M. Dougherty, A. Lutz and D.G. Fletcher (2010) Development of a 30 kW Inductively Coupled Plasma Torch Facility for Aerospace Material Testing *University of Vermont*
- [6] P.F. Barbante (2001) Accurate and Efficient Modeling of High Temperature Non-equilibrium Air Flows *von Karman Institute for Fluid Dynamics*
- [7] T. Magin (2004) A Model for Inductive Plasma Wind Tunnels *von Karman Institute for Fluid Dynamics*
- [8] D.G. Fletcher and M. Playez (2006) Characterization of Supersonic and Subsonic Plasma Flows *von Karman Institute for Fluid Dynamics AIAA 2006-3294*
- [9] M. Playez 'Titan Atmosphere Plasma Characterization using Spectroscopic Measurement Techniques, Ph.D. Dissertation, Ecole Centrale Paris, *Laboratoire d'Energetique Moleculaire et Macroscopique, Combustion*, June 2006.

# SPECIES AND TEMPERATURE GRADIENT MEASUREMENTS IN THE REACTING BOUNDARY LAYER OVER ICP TEST SAMPLES

D. G. Fletcher, A. J. Lutz, J. M. Meyers, W. P. Owens, and J. Uhl

*University of Vermont, Burlington, Vermont 05405 USA*

## ABSTRACT

Improved estimations of stagnation point heat transfer require more physically realistic gas-surface interaction models. This paper reports on the ongoing development of spatially resolved laser diagnostic measurements of key reacting species in the thermal boundary layer over material samples placed in the flow of an inductively coupled plasma torch facility in stagnation point configuration. The specific case of carbon extraction from graphite by atomic nitrogen (nitridation) is used to illustrate the methodology, which provides translational temperature and species concentration along the stagnation streamline. These measurements are used to make a preliminary estimate of the nitridation rate for graphite surface temperature of 1590 K.

## 1. INTRODUCTION

There are many gas-surface interactions that are important in atmospheric entry aero-thermal heating rate calculations. These include surface catalyzed recombination for both homogeneous and heterogeneous molecule formation at lower heating rates, and oxidation and nitridation reactions for more severe heating [1]. Many of these rates have been determined in laboratory experiments under carefully controlled conditions using techniques that are well suited to the particular test environment. However, the test conditions for such laboratory measurements are often very different from the trajectory conditions that a material will encounter in an eventual atmospheric entry application. This situation motivates efforts to develop *in situ* diagnostic techniques for plasma facilities that more closely reproduce the trajectory aerothermal environment. One such effort is underway at the University of Vermont, where laser diagnostic techniques are being used to probe key species and thermodynamic conditions in the reacting boundary layer formed by a plasma flowing over a material sample placed in stagnation point configuration. These measurements are aimed at providing data that can be used to guide the development of better physical and chemical models for gas-surface interactions.

The specific example of extraction of carbon atoms from

hot graphite in a nitrogen plasma is chosen to illustrate this general laser-diagnostic based approach. We use nitridation to refer to this process, which has the following chemical description



This reaction is of interest because carbon is the most common base material, often as a fiber matrix, for thermal protection systems designed to handle the highest heat flux levels through ablation. In addition to its contribution to erosion of the carbon base material at high heating conditions, active nitridation of carbon may also be an important source of radiant heat flux to the stagnation region as the cyanogen radical is known to be a strong radiator owing to its permanent dipole.

While this reaction has been studied previously [2][3][4] in a number of different experimental facilities, the results have varied widely as discussed by Zhang et al [5]. Two of the existing published values for this reaction rate show it to be slower than the corresponding rate for carbon oxidation, while the third published value [4] is more rapid than oxidation. This disparity in published reactivity values, coupled with the fact that none of the experimental facilities used in the studies were designed explicitly to produce trajectory relevant aerothermal test conditions, provides additional motivation for the investigation.

Following brief descriptions of the Inductively Coupled Plasma (ICP) Torch facility, the laser and optical instrumentation, and the experimental approach, measurements from several different carbon nitridation experiments are presented. These results are discussed and a preliminary value of the nitridation rate is derived from the measurements.

## 2. FACILITY DESCRIPTION

The 30 kW ICP Torch Facility at the University of Vermont is designed to test materials that are being developed for high-temperature aerospace applications with

sample diameters ranging from 20 to 25 mm. An important feature of the test chamber is the extensive optical access available from large-diameter, orthogonally located viewports, which are seen in Fig. 1. These viewports, which are located in the plane of the test sample, are used to obtain spectrally resolved emission measurements and to provide laser and photo-detection access for laser-induced fluorescence (LIF) investigations. Additional optical viewports are installed in the bottom flange with a direct view of the test sample. Optical pyrometry and reflectivity measurements are conducted using these ports. The power supply for the ICP Torch is seen at the left of the torch chamber in Fig. 1, and this supplies radio-frequency (RF) electrical power to the load coil at frequencies that can be varied between 2 and 4 MHz, at a maximum voltage of 12 kV and maximum power of 30 kW. The load coil surrounds a 36 mm internal diameter quartz tube that separates the injector block from the lower flange of the test chamber. In its current configuration, a brass injector block assembly delivers the test gas mixture to the plasma generation region located in the quartz tube within the axial limits of the load coil. This injector block design is based on annular injection around a bluff central body to promote axisymmetric flow recirculation that stabilizes the plasma in the coupling zone.[6]

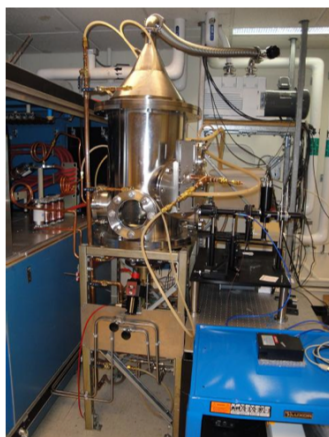


Figure 1: The University of Vermont ICP Torch Facility.

Two main gas supply lines bring argon, which is used to initiate the plasma, and the desired test gas mixture separately to the injector block. All gases are supplied by bottles and precise mixtures and mass flow rates are maintained by mass flow controllers for each cylinder. This allows operation of the ICP Torch Facility for a wide variety of gas mixtures for simulation of many different planetary atmospheres, including those of mars and titan. The test chamber is stainless steel and the conical exit is fitted with a heat exchanger to reduce the exhaust gas temperature before it reaches the vacuum pump. Separate cooling circuits serve the power supply, heat exchanger and sample/probe holders. [7]

Laser diagnostic instrumentation is installed at the UVM

ICP laboratory to measure gas-phase flow properties. The full beam path is shown in Figure 2. The 532 nm output from a Powerlite 8000 Nd:YAG laser pumps a ND6000 dye laser, and the dye laser output is frequency tripled through consecutive autotrackers. For the present investigation, the dye laser was operated with DCM, which, after frequency tripling, provides tunable UV radiation over a wavelength range of 205 to 220 nm. Downstream of the crystals, the UV output beam is divided in two directions; 90% of the beam energy is directed toward the test chamber and 10% is sent to the microwave-discharge Flow Reactor (FR). As discussed below, additional energy is removed from the ICP leg by two additional beam splitters to maintain the laser pulse energy density at the ICP measurement location at modest levels. Fluorescence from both the ICP and flow reactor laser probe volumes is detected using gated PMTs with 10 nm bandpass filters centered at 870 nm. A tilting stage was used to angle the PMT view at the ICP such that signal obscuration by the sample is minimized. A Molelectron energy meter downstream of the flow reactor is used to normalize the measured LIF signals for the laser pulse energy fluctuations, with an additional energy meter on the ICP beam path to verify the relative beam energies. All signals are averaged and recorded using a gated integrator system.

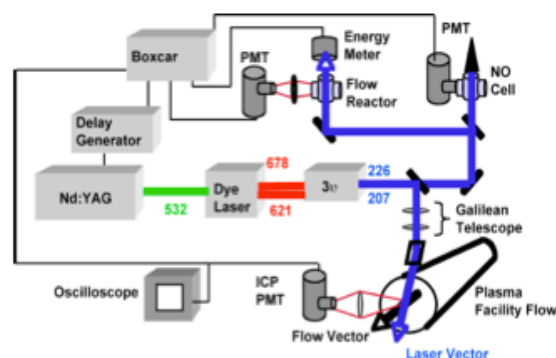


Figure 2: Laser and instrumentation configuration for making two-photon LIF measurements in the 30 kW ICP Torch Facility.

The target species for two-photon LIF measurements in the present investigation is atomic nitrogen, as its flux to the surface is presumed to result from its consumption by active carbon surface nitridation. At present we assume that the reaction rate is not limited by the rate of nitrogen atom diffusion, but this will have to be investigated at some point. By making simultaneous measurements of an absorption transition in both the ICP Torch Facility and in the flow reactor, absolute concentrations of nitrogen atoms can be determined based on the known concentration in the flow reactor, which is established by chemical titration, as described by Fletcher and Playez [8]. Briefly, such measurements involve performing Raman calibrations of the detection optics for both locations, as well as measuring the respective fluorescence yields, beam spatial profiles, and energies.

### 3. EXPERIMENTAL APPROACH

Two-photon LIF will be used to obtain quantitative measurements of nitrogen atom densities in the reacting boundary layer over graphite samples placed in the nitrogen plasma stream to allow a determination of the nitridation reaction efficiency. For the present investigation, we assume that nitridation arises directly from atomic nitrogen reaching the surface and combining with a surface carbon atom, so the reaction efficiency,  $\gamma_N$ , is calculated from the following equation [5].

$$\gamma_N = \frac{\Gamma_{CN}}{\Gamma_N} = \left( \frac{\Delta M_C}{A m_C \Delta t} \right) / \left( \frac{n_N}{4} \sqrt{\frac{8 k_B T}{\pi m_N}} \right) \quad (2)$$

The reaction rate efficiency is the ratio of the CN flux leaving the surface,  $\Gamma_{CN}$ , to the nitrogen atom flux arriving at the surface,  $\Gamma_N$ , which are the rates of CN creation and N-atom flow to the surface, respectively. Note that this is based on the presumed mechanism of a nitrogen atom extracting a carbon atom from the surface. The flux ratio can be expressed as a function of the sample carbon mass loss  $\Delta M_C$ , the sample area  $A$ , the atomic masses of carbon and nitrogen  $m_C$  and  $m_N$ , the exposure time  $\Delta t$ , the nitrogen atom number density  $n_N$ , the Boltzmann constant  $k_B$  and temperature  $T$ . Of these parameters, the only values that need to be measured experimentally are the carbon mass loss, sample area, exposure time, temperature and nitrogen atom number density just above the sample surface.

The sample area is measured directly from the initial geometry, and for these first tests the change in area due to plasma exposure is assumed to be negligible. All samples used have a 20 mm nominal diameter and a 12.5 mm height. The carbon mass loss is calculated from pre- and post-test mass measurements. Exposure times for the graphite samples in nitrogen plasmas were recorded from the time that the target test conditions were achieved. Owing to the sample geometry used for these tests, the samples were always in the plasma, even during startup. However, the starting conditions in argon have very low heat flux levels, and we expect that exposure to the argon plasma did not affect the surface. Two-photon LIF is used to make spatially resolved measurements of translation temperature and nitrogen atom number density.

Two-photon LIF of atomic nitrogen can be done using either of two excitation strategies, and these are shown in Figure 3. Owing to use of DCM dye, higher pulse energies are available for the longer wavelength excitation (211 nm), and so this approach is used for the present investigation, despite the fact that the fluorescence is polarized. As mentioned above, the output of the dye laser is frequency tripled to the 211 nm wavelength region. Note that both nitrogen number density and translational temperature are needed to quantify the nitrogen atom flux rate, and so the measurements were made by scanning the

dye laser wavelength over the atomic transition. Translation temperature is determined from a spectral fit of the fluorescence for both the reactor and ICP data. As the flow reactor conditions are at room temperature, the fit is used to determine the laser line-width, which is then used in the fit of the ICP LIF line shape to extract a temperature from the plasma measurement. The current spectral model assumes negligible collisional broadening, and so is based on the convolution of the gaussian laser frequency distribution and the thermal distribution of absorbing atom velocities. Figure 4 shows a plot of the 2-photon LIF signal for atomic nitrogen in the UVM ICP torch facility free-stream, as well as a simultaneous signal recorded in the flow reactor from a recent test. The fits obtained from the spectral model of the line shape are also shown for each spectrum. As the flow reactor condition is near room temperature, the transition width is considerably narrower for the transition in the reactor than in the ICP Torch plasma flow.

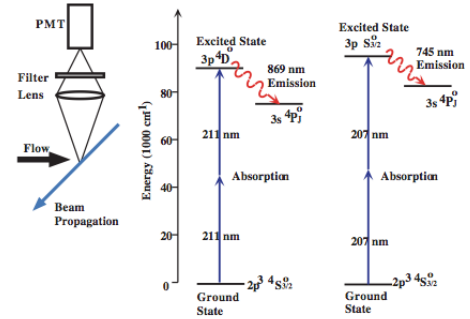


Figure 3: Two-photon nitrogen excitation strategies.

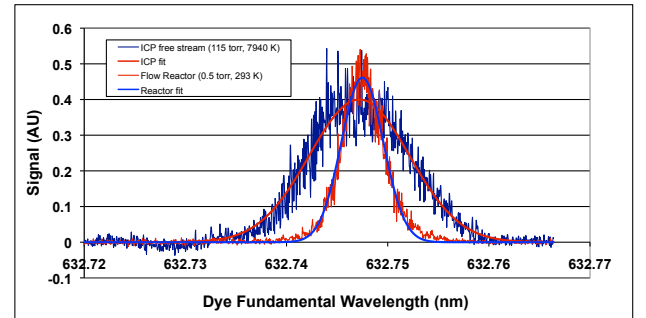


Figure 4: Two-photon LIF measurements within the UVM ICP chamber and flow reactor.

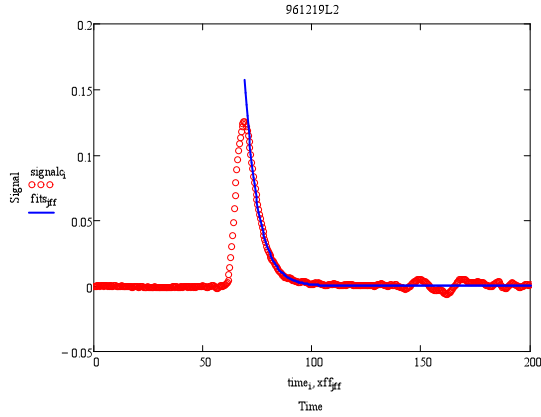
The spectrally integrated fluorescence signal is proportional to the local number density of atomic nitrogen. However, to convert the values measured in the ICP to absolute number densities requires measurement of additional parameters, as well as a chemical titration to establish the number density in the flow reactor. The explicit

relationship for number density is

$$(n_N)_{icp} = \frac{\int (S/E^2)_{icp} d\omega}{\int (S/E^2)_{fr} d\omega} \frac{D_{fr}}{D_{icp}} \frac{\tau_{fr}}{\tau_{icp}} \frac{w_{icp}^2}{w_{fr}^2} (n_N)_{fr}, \quad (3)$$

where  $S$  is the fluorescence signal,  $E$  is the pulse energy,  $D$  is the Raman calibration factor,  $\tau$  is the observed fluorescence lifetime,  $w$  is the beam waist at the measurement locations, and the subscripts refer to ICP and flow reactor, respectively. Measurements of all parameters needed for conversion of relative densities to absolute values have been obtained and examples are shown below and discussed briefly.

Several measurements of the observed fluorescence lifetime are taken during the ICP tests for both the ICP and flow reactor LIF, and the lifetime is determined from a single exponential fit to the measurements. An example ICP measurement is shown in Figure 5 below, where the influence of quenching at the higher pressure in the ICP is evident. The lifetime derived from the fit is 6.2 ns, which is considerably shorter than the  $\approx 43$  ns radiative lifetime for the  $3p^4D^0$  electronic state.



(a) ICP Lifetime

Figure 5: Observed fluorescence lifetime for the  $3p^4D^0$  state in the ICP Torch Facility.

A Spiricon beam profiler is used to record images of the laser energy distribution at each measurement location when the facility is not running, and the waist values are extracted from these images. At the observation point in the ICP Torch Facility the laser beam is not perfectly circular, but the narrowest dimension of the elliptical beam is aligned along the direction perpendicular to the surface, which provides a spatial resolution of about 0.4 mm in this direction. An example beam image from the measurements is given in [9].

Raman calibrations are also done for both the ICP and flow reactor detection instrumentation. The approach we follow for the Raman calibration of our detection optics is based on the procedure outlined in [10], with hydrogen as the scattering species. For each measurement location the experiment is conducted using the fundamental output of the dye laser operated with DCM dye, which is

brought to each of the two calibration locations by means of prisms. Owing to the large pulse energy of the dye fundamental relative to the tripled UV beam energy, a Scientech energy calorimeter was used to terminate the beam, and a reflection from the front surface was directed to a Molelectron head for pulse to pulse normalization of the Raman scattered signal. The boxcar values are converted to absolute energy values by comparing the voltage levels with the Scientech front panel readings. The dye laser is tuned continuously over the transmission range of the filters used in each detection system, and the value of the Raman calibration factor was taken at the transition location.

The last experiment needed to calibrate the ICP Torch Facility LIF measurements is the chemical titration that serves to establish the absolute number density of nitrogen atoms present in the flow reactor stream. Chemical titration of the nitrogen atoms by the fast reaction  $N + NO \rightarrow N_2 + O$  is described in [8], and involves adding the titration gas, which is 10%  $NO$  in  $He$ , just above the measurement location and monitoring the extinction of the N atom LIF signal while measuring the titration gas flow rate and cell pressure.

The graphite sample test procedure begins with aligning the sample in the center of the plasma with the facility not running and registering the laser beam stage micrometer and PMT stage micrometer to the cold sample leading surface location. The facility is then closed and evacuated, and the plasma is initiated with argon. After raising pressure to the target level, nitrogen is added and argon is removed until full nitrogen plasma flow is established. Moving away from the sample in small steps, laser wavelength scans are performed at each measurement location, and pressure and mass flow are maintained at constant levels. If time allows, some measurements are repeated to judge how steady conditions are maintained. Surface temperature is monitored using a two-color optical pyrometer.[9]

#### 4. RESULTS AND DISCUSSION

Seven identical 20 mm diameter graphite samples were tested in the ICP Torch Facility, and the mass loss and test times for these samples are given in Table 3 below, along with the respective mass loss rates. Note that for these preliminary measurements, changes were being made to the tank circuit of the power supply, injector block, and sample holder, so the range in mass loss rates for similar surface temperatures is not surprising. However, for samples 6 and 7, where boundary layer data were acquired during the tests, the configuration of power supply, injector block and sample holder were unchanged, and steps were taken to ensure that no air was entering the plasma stream. Sample pre- and post-test dimension measurements to evaluate surface recession are given in Table 4, where  $L$  refers to axial length and  $\phi$  refers to diameter.

Table 1: Test Sample Mass Measurements

#	Mass <sub>0</sub> (g)	Mass <sub>f</sub> (g)	ΔMass (g)	Run Time (m:s)	Loss Rate (mg/s)	Wall Temp. (C)
1	7.833	7.116	0.717	15:10	.788	1380
2	7.838	6.125	1.713	33:10	.861	
3	7.839	6.351	1.488	40:40	.610	
4	7.86	7.226	0.634	58:20	.181	1243
5	7.825	6.572	1.253	30:00	.696	1304
6	7.857	6.994	0.863	34:55	.412	1427
7	7.831	6.57	1.261	63:20	.332	1318

Table 2: Test Sample Recession Measurements

#	L <sub>0</sub> (mm)	L <sub>f</sub> (mm)	ΔL (mm)	φ <sub>0</sub> (mm)	φ <sub>f</sub> (mm)	Δφ (mm)
1	7.833	7.116	0.717	19	18.5	0.5
2	7.838	6.125	1.713	19	18	1
3	7.839	6.351	1.488	19	18	1
4	7.86	7.226	0.634	19	18.5	0.5
5	7.825	6.572	1.253	19	19	0
6	7.857	6.994	0.863	19	18.5	0.5
7	7.831	6.57	1.261	19	18	1

Most of the graphite mass loss came from from the axial dimension; however, additional mass was lost in the shoulder region, which significantly altered the profile. With high temperature conditions and long exposure time, even the diameter changed as shown in Table 2. Figure 6 shows sample 2 compared to a virgin sample, where the overall shape change is clearly seen.



Figure 6: Sample 2 post-test alongside a virgin sample, showing significant shape change.

A number of tests were done without LIF to have a rough estimate of the recession rate for the graphite. Additional tests were needed to ascertain whether the laser energy in the probe volume was at a level sufficient to ensure that no undesired multi-photon processes would interfere with the measurements. Results from these tests led us to install additional beam splitters ahead of the test section to reduce the beam energy by a factor 3, and to move the focal point of the lens on the beam delivery stage 10 mm beyond the observation point of the collection optics. These

measures produced the appropriate two-photon scaling of the detected LIF signals, giving the desired slope of 2 on a log plot of the LIF signal versus beam energy. This was achieved in time for the testing the 7th sample.

Boundary layer survey results from the test of sample 7 are shown below, with the translation temperature in Figure 7 and the relative nitrogen atom density in Figure 8. In both figures, we see that the 20 mm diameter sample produces a nearly 1.5 mm boundary layer thickness that is captured reasonably well by the spatial resolution of the LIF technique. For this sample we were unable to obtain measurements as close to the surface as for some of the other tests owing to misjudging the surface recession. While every attempt was made to precisely register the beam position with respect to the surface, attaining successful measurements at the appropriate locations was not straightforward. Additional measurements were done to assess radial gradients, and these were discussed by Lutz et al. [9]

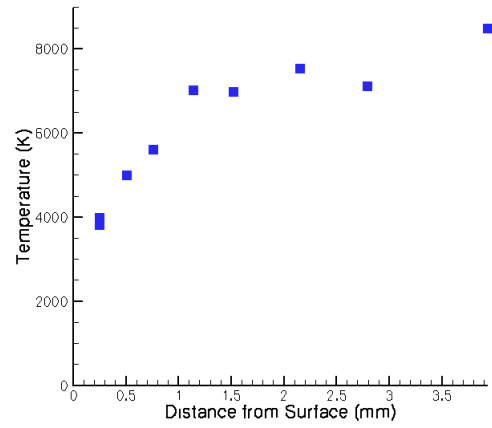


Figure 7: Boundary layer translational temperature distribution for sample 7.

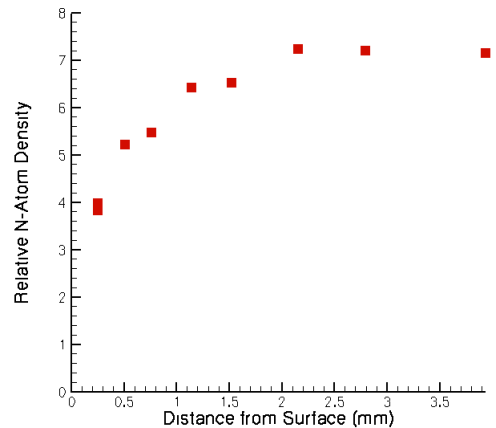


Figure 8: Relative nitrogen atom density in boundary layer for sample 7.

As mentioned above, the additional experimental measurements that are needed to convert the relative nitrogen atom density measurement to absolute values include Raman scattering calibrations of both the ICP and FR detection optics and a chemical titration of the nitrogen atoms in the flow reactor. Raman calibrations were done following the sample tests, and they yielded values of  $D_{FR} = 8.74(10)^{-9}$  V-cm-sr and  $D_{ICP} = 5.95(10)^{-10}$  V-cm-sr. The greater value at the flow reactor is attributed to the lower f/number of the detection optics as the PMT is very close to the beam.

A titration experiment was done after the dye had been changed to a mixture of DCM and LDS 698, which was used to provide access to both O atom and CO LIF for another experiment. Thus, the endpoint was detected by locating the asymptote for maximum O atom LIF as the titration gas flow rate is increased. Even so, the endpoint is quite sharp, and this titration experiment produced a value of atomic nitrogen number density of  $n_N = 1.57(10)^{14}$  cm $^{-3}$  for the same nominal flow reactor conditions as for the nitridation tests.

Using these values along with the measured fluorescence lifetimes for each location ( $\tau_{FR} = 39.9$  ns and  $\tau_{ICP} = 6.2$  ns), beam waists ( $w_{FR} = 0.516$  mm and  $w_{ICP} = 0.4$  mm), and integrated LIF signals in Eq.3 yields a value of  $n_N = 1.9(10)^{16}$  cm $^{-3}$  at the boundary layer edge, which is considerably different than the predicted equilibrium value of  $n_N = 1.245(10)^{17}$  cm $^{-3}$ . The most likely reason for the discrepancy appears to be the lifetime measurements, which are consistently longer than expected for the pressure levels in either the ICP or flow reactor. If we calculate the fluorescence lifetimes using the collisional quenching scaling measured by Copeland et al [11], we obtain values of 0.7 ns for the ICP at 96 torr and the 31.9 ns for the flow reactor at 0.54 torr. Using these values in Eq.3 in place of the measured lifetimes produces a nitrogen atom concentration value of  $n_N = 1.35(10)^{17}$  cm $^{-3}$  at the boundary layer edge, which is within 8% of the equilibrium value. At present, the cause of the longer than expected lifetime measurements is not yet understood, but it is being investigated.

The boundary layer edge value of nitrogen atom concentration is sufficient to calibrate all relative values acquired during the boundary layer survey provided that no changes were made to the optical detection system, and provided that the near wall values of the laser pulse energy are corrected for clipping by the sample surface. For the point nearest the surface, this produces a value of  $n_N \approx 2.7(10)^{16}$  cm $^{-3}$ , and this value along with the near wall surface temperature are used in Eq.2, along with the carbon mass loss data for sample 7 to provide a preliminary estimate of the active carbon nitridation efficiency,  $\Gamma_{CN} = 0.0038$ , for these test conditions. Efforts are ongoing to quantify the uncertainties in the absolute species concentration values and the reaction efficiency through additional experiments.

## 5. SUMMARY

Preliminary boundary layer survey measurements that can be used to assess gas-surface interaction phenomena have been presented and discussed for the particular case of active nitridation of carbon for graphite samples in a nitrogen plasma. Spatially resolved measurements of temperature and nitrogen atom density have been presented along the stagnation streamline, and the near wall measurement conditions have been used to provide a preliminary estimate of the nitridation efficiency for the test conditions that pertained during the test of sample 7.

We believe that these boundary layer survey measurements can be extended to investigate other important gas-surface interaction processes that are of interest for aero-thermal heating of both hypersonic flight and atmospheric entry vehicles.

## ACKNOWLEDGMENTS

This work has been supported by NASA Grant NNX08AC98A and AFOSR Grant FA9550-08-1-0414.

## REFERENCES

- [1] Wright, M.J., Olejniczak, J., Brown, J.L., Hornung, H., and Edquist, K.T., (2006) *J. of Thermophysics and Heat Transfer*, 4, 631
- [2] Goldstein, H.W., (1964) *J. Phys. Chem.*, 68, 39.
- [3] T. Suzuki, K. Fujita, K. Ando, and T. Sakai, (2008) *J. Thermo. Heat Trans.*, 22, 382.
- [4] C. Park and D. Bogdanoff (2006) *J. Thermo. Heat Trans.*, 20, 487.
- [5] Zhang, Pejakovic, D., Marschall, J., and Fletcher, D.G. (2009) AIAA Paper No. 2009-4251
- [6] M. Playez, (2006) Ph.D. Dissertation, Ecole Centrale Paris, *Laboratoire d'Energetique Moleculaire et Macroscopique, Combustion*.
- [7] W.P Owens, J. Uhl, M. Dougherty, A. Lutz and D.G. Fletcher (2010) AIAA Paper No. 2010-4322
- [8] Fletcher, D. G., Playez, M. (2006) AIAA Paper 2006-3294
- [9] Lutz, A.J., Owens, W.P., Meyers, et al (2011) AIAA Paper No. 2011-901.
- [10] Bischel, W.K., Bamford, D.J., and Jusinski, L.E. (1986) *Applied Optics*, 25, 1215.
- [11] Copeland, R.A., Jeffries, J.B., Hickman, A.P. and Crosley, D.R. (1987) *J. Chem. Phys.*, 86, 4876.